

The Pennsylvania State University

The Graduate School

**CO<sub>2</sub>, O<sub>2</sub>, AND THE HISTORY OF THE GREENHOUSE EFFECT:  
SELECT PROBLEMS IN THE EVOLUTION OF THE  
EARTH'S ATMOSPHERE AND CLIMATE**

A Dissertation in  
Geosciences and Astrobiology

by

Rebecca C. Payne

© 2020 Rebecca C. Payne

Submitted in Partial Fulfillment  
of the Requirements  
for the Degree of

Doctor of Philosophy

December 2020

The dissertation of Rebecca C. Payne was reviewed and approved by the following:

James F. Kasting  
Evan Pugh Professor, Department of Geosciences  
Dissertation Advisor  
Chair of Committee

Christopher House  
Professor, Department of Geosciences

Julie Cosmidis  
Assistant Professor, Department of Geosciences

Raymond Najjar  
Professor, Department of Meteorology and Atmospheric Sciences

Mark Patzkowsky  
Professor, Department of Geosciences  
Associate Head for Graduate Programs and Research (Geosciences)

## Abstract

To understand the history of life on Earth, it is essential to understand the evolution of the global climate that has maintained a relatively stable and habitable environment for life over the last 4.6 billion years. Earth's climate itself is the result of a delicate balance between the composition of the atmosphere and the processes on the surface—in the oceans, and on the continents—that interact with it.

Prior to the rise of atmospheric O<sub>2</sub> at ~2.45 Ga, Earth's climate relied on CO<sub>2</sub> as a major atmospheric constituent in order to keep Earth at a habitable temperature in spite of lower solar luminosity. While climate models have estimated that at least several percent of CO<sub>2</sub> in the atmosphere would have been needed to maintain a habitable climate, geochemical data from paleosols have largely predicted CO<sub>2</sub> one or two orders of magnitude lower, though there is considerable disagreement between paleosol studies. We argue instead that oxidized iron micrometeorites from ~2.7 Ga offer a new point of comparison that is not subject to the same potential biases as paleosols. Abundant CO<sub>2</sub> could have oxidized iron micrometeorites during atmospheric entry, meaning that preserved micrometeorites may offer a means of estimating atmospheric CO<sub>2</sub> in an atmosphere largely devoid of other potential oxidants. We estimate that an atmosphere of at least ~23% CO<sub>2</sub> would be sufficient to oxidize the micrometeorites and keep surface temperatures warm. Using a climate model, we demonstrate that the new CO<sub>2</sub> constraint from micrometeorites also supports the idea that the partial pressure of N<sub>2</sub> (and overall surface pressure) was lower on the early Earth, in order for high CO<sub>2</sub> to not cause surface temperatures to conflict with evidence of glaciation in the late Archean.

The emergence of atmospheric O<sub>2</sub> after ~2.45 Ga, and its role as a major constituent during the last ~541 Ma in particular, resulted in a fundamental shift in the greenhouse effect and atmospheric CO<sub>2</sub>. Using a coupled one-dimensional photochemical-climate model, we find that atmospheric O<sub>2</sub> equal to or higher than 21% (its present-day abundance) slightly enhances warming by other greenhouse gases like CO<sub>2</sub> and H<sub>2</sub>O, by broadening their absorption lines to increase effectiveness. But O<sub>2</sub> exerts a minor effect on surface temperature at most; our findings support the classical interpretation that changes in solar luminosity, CO<sub>2</sub>, and global geography are the primary controls on global climate in the Phanerozoic. We apply this analysis specifically to the early Cretaceous, at ~100 Ma, and argue that higher atmospheric O<sub>2</sub> would support both the hot temperatures of the Cretaceous as well as the needs of the massive terrestrial life (namely, dinosaurs) that mark that time in geologic history.

We also consider carbon cycling on long timescales, using a box model of the atmosphere-ocean-seafloor to study changes in CO<sub>2</sub> and in C sources and sinks over the last 100 Ma. We demonstrate that both seafloor weathering and continental weathering are important to climate change since the Cretaceous. Seafloor weathering is closely tied to seafloor temperatures, and so was likely to have been a more important C sink during the Cretaceous when global temperatures were higher than today. We agree with recent analyses that have suggested that continental weathering—especially an increase in continental weatherability over the last ~100 Ma due to tectonic activity and uplift, as well as sea level change—has driven much of the CO<sub>2</sub> cycling.

# Table of Contents

<b>List of Tables</b> .....	<b>vi</b>
<b>List of Figures</b> .....	<b>vii</b>
<b>Preface</b> .....	<b>viii</b>
<b>Acknowledgements</b> .....	<b>ix</b>
<b>Chapter 1. Introduction</b> .....	<b>1</b>
<b>Chapter 2. Iron micrometeorite oxidation as a proxy for atmospheric CO<sub>2</sub> during the Neoproterozoic</b> .....	<b>7</b>
1. BACKGROUND .....	7
2. MICROMETEORITE OXIDATION .....	9
2.1. <i>Entry physics</i> .....	9
2.2. <i>Micrometeorite oxidation chemistry</i> .....	12
3. PHOTOCHEMICAL CALCULATIONS .....	17
3.1. <i>Methods</i> .....	17
3.2. <i>Results</i> .....	19
4. DISCUSSION .....	20
4.1. <i>Constraints on pCO<sub>2</sub> from Neoproterozoic climate</i> .....	20
4.2. <i>Constraints on pCO<sub>2</sub> from paleosols</i> .....	25
4.3. <i>Other analyses of the Tomkins et al. micrometeorites</i> .....	27
5. CONCLUSIONS .....	28
APPENDIX 1: FULL DERIVATIONS AND MODEL SPECIFICS .....	30
A1.1. <i>Full derivation of CO<sub>2</sub> mass balance, Eq. (4)</i> .....	30
A1.2. <i>Derivation of Eq. 10</i> .....	32
<b>Chapter 3. The response of the greenhouse effect, and surface temperature, to changes in atmospheric O<sub>2</sub> during the Phanerozoic</b> .....	<b>51</b>
1. BACKGROUND .....	51
2. CONSERVATION OF NITROGEN .....	53
3. RADIATIVE FORCING CALCULATIONS .....	57
4. CONVERGED MODEL CALCULATIONS .....	62
5. DISCUSSION .....	67
5.1. <i>Additional issues with the Poulsen et al. calculations</i> .....	67
5.2. <i>Comparison with other 3-D models</i> .....	71
<b>Chapter 4. Long-term changes in atmospheric CO<sub>2</sub> and the carbon cycle throughout the Phanerozoic</b> .....	<b>74</b>
1. BACKGROUND .....	74
2. METHODS .....	81
2.1. <i>Model development</i> .....	81
2.2. <i>Activation energy calculations</i> .....	85
3. RESULTS .....	88
4. DISCUSSION .....	94
4.1. <i>Marine controls on C cycling</i> .....	94
4.2. <i>The role of continental processes in the Phanerozoic C cycle</i> .....	96
5. CONCLUSIONS .....	99
<b>Chapter 5. Concluding Remarks</b> .....	<b>101</b>
<b>Bibliography</b> .....	<b>103</b>

## List of Tables

<b>2.1</b>	Oxidation pressure range upper and lower bounds.....	<b>11</b>
<b>A1.1</b>	Reaction rates.....	<b>37</b>
<b>3.1</b>	Effect of O <sub>2</sub> on CH <sub>4</sub> and N <sub>2</sub> O column mixing ratio.....	<b>56</b>
<b>3.2</b>	O <sub>2</sub> effects for one-step and converged calculations.....	<b>60</b>
<b>3.3</b>	O <sub>2</sub> effect on planetary albedo.....	<b>62</b>
<b>3.4</b>	Effect of accurate ozone profile for converged calculations.....	<b>65</b>

## List of Figures

<b>2.1</b>	Vertical profiles of major Archean atmosphere constituents.....	<b>20</b>
<b>2.2</b>	1-D climate model estimates for Archean surface temperature.....	<b>24</b>
<b>2.3</b>	Comparison of climate model/paleosol Archean pCO <sub>2</sub> estimates.....	<b>26</b>
<b>A1.1</b>	Photochemical model atmosphere setup.....	<b>35</b>
<b>A1.2</b>	Comparison of vertical profiles of Archean atmosphere composition.....	<b>36</b>
<b>3.1</b>	Flux for one-step Cretaceous calculations.....	<b>59</b>
<b>3.2</b>	Flux for converged Cretaceous calculations.....	<b>63</b>
<b>3.3</b>	Vertical profile of ozone for Cretaceous calculations.....	<b>64</b>
<b>3.4</b>	Vertical profile of temperature for Cretaceous calculations.....	<b>65</b>
<b>3.5</b>	Comparison of O <sub>2</sub> estimates from various models.....	<b>70</b>
<b>4.1</b>	Proxy error analysis; model-proxy disagreement.....	<b>79</b>
<b>4.2</b>	K-T&C 2-box and our 3-box model schematics.....	<b>83</b>
<b>4.3</b>	Model comparison for saturation state, temperature, and marine C fluxes.....	<b>89</b>
<b>4.4</b>	K-T&C model “best fit” case.....	<b>92</b>
<b>4.5</b>	Our model “best fit” case.....	<b>93</b>

## Preface

Chapter 2 is published in the *Proceedings of the National Academy of Sciences (PNAS)* as of January 2020 (<https://doi.org/10.1073/pnas.1910698117>), with coauthors Don Brownlee and James Kasting. I ran the modeling cases described in the chapter and wrote the analysis, and thank both for their input in refining the calculations and contributions to some of the text.

Chapter 3 is published in the *Journal of Geophysical Research: Atmospheres (JGR: Atmospheres)* in August 2016 (<https://doi.org/10.1002/2016JD025459>), with coauthors Amber Young (née Britt), Howard Chen, David Catling, and James Kasting. I conducted the modeling and wrote the analysis; I thank all coauthors for their input on the text.

Chapter 4 is unpublished as of writing this dissertation, and is a collaboration between myself and my advisor Jim Kasting. I modified the source code, conducted the modeling, and wrote the analysis, and thank Jim for his guidance and contributions to some of the text.

## Acknowledgements

Thank you to my friends and family, who have kept me sane, been a constant source of fun and support, and listened patiently to my lengthy excited and/or frustrated discussions about rocks and air over the last several years.

I would also like to thank all of the Kasting research group, past and present—especially Sonny Harman, Peng Liu, Benjamin Hayworth, Aoshuang Ji, Jingjun Xi, Evan Sneed—for their help, camaraderie, and insight.

Finally, I'd like to thank my committee—Chris House, Julie Cosmidis, and Ray Najjar—as well as the coauthors who have contributed to the various chapters of this dissertation and constitute the royal “we” herein: Don Brownlee, David Catling, Amber Young (née Britt), and Howard Chen, and especially my advisor Jim Kasting. This work wouldn't have been possible without you. I am beyond grateful for everything I've learned these past few years, and can't wait to keep learning.

“There is nothing more deceptive than an obvious fact.”

—*The Adventures of Sherlock Holmes: The Boscombe Valley Mystery*,  
Sir Arthur Conan Doyle

“The entire universe has been neatly divided into things to (a) mate with, (b) eat, (c) run away from, and (d) rocks.”

—*Equal Rites*,  
Terry Pratchett

“It is sometimes said that scientists are unromantic, that their passion to figure out robs the world of beauty and mystery. But is it not stirring to understand how the world actually works—that white light is made of colors, that color is the way we perceive the wavelengths of light, that transparent air reflects light, that in so doing it discriminates among the waves, and that the sky is blue for the same reason that the sunset is red? It does no harm to the romance of the sunset to know a little bit about it.”

—*Pale Blue Dot: A Vision of the Human Future in Space*,  
Carl Sagan

# Chapter 1.

## Introduction

The evolution of the Earth's climate over the course of its 4.6-billion-year history represents a dynamic balancing act between solar radiation, the changing chemical composition of the atmosphere, and the adaptive strength of the Earth's greenhouse effect. It is widely accepted that the Sun was less bright earlier in its life, with a total luminosity of only about 70% that of today at the start of Earth's history (Kump et al., 2000). But geologic evidence suggests that the Earth remained relatively warm for the vast majority of its history: there is evidence for sustained liquid water on Earth's surface at ~4.3 Ga from detrital zircons (Mojzsis et al., 2001; Wilde et al., 2001), and indicators of life as early as ~3.7 Ga in the Isua supracrustal belt (Nutman et al., 2016). The evidence for a warm climate in spite of weaker solar luminosity—a challenge referred to as the Faint Young Sun paradox (Sagan & Mullen, 1972; Kasting, 2010)—establishes the need for a strong early greenhouse effect during the Archean (~4 – 2.5 Ga) to maintain surface temperatures conducive to life.

Studying the evolution of the greenhouse effect is further complicated by the role of O<sub>2</sub> in Earth's atmospheric history. O<sub>2</sub> was negligible in the early Earth's atmosphere, resulting in a generally reducing atmosphere, before its concentration began to rise in the late Archean around ~2.5 Ga (Holland, 1994/2006), in a change referred to as the Great Oxygenation Event (GOE). Over time, this changed the atmosphere's redox state from weakly reducing to weakly oxidizing. In the Phanerozoic (~541 Ma to today), O<sub>2</sub> became a major atmospheric constituent and now constitutes approximately 21% of the atmosphere

by volume. This major shift in atmospheric composition and redox state means that the makeup of greenhouse gases present in the atmosphere would have needed to adapt accordingly, and that effectively studying the Earth's greenhouse effect through time requires studying it in tandem with the rise of atmospheric O<sub>2</sub>.

Several gases have been assessed for their potential as the dominant greenhouse gas in the pre-oxygenated atmosphere prior to the rise of O<sub>2</sub>. Sagan and Mullen (1972) favored NH<sub>3</sub>, but NH<sub>3</sub> is photochemically unstable even in a reduced environment and is quickly broken down when exposed to UV radiation (Kuhn & Atreya, 1979). It is therefore unlikely that it would have been able to build up to the concentrations needed for it to have been a major contributor to early warming. H<sub>2</sub> can act as a greenhouse gas through collisions with N<sub>2</sub> (Wordsworth & Pierrehumbert, 2013), and production of H<sub>2</sub> from early serpentinization and volcanism may have contributed enough to boost the atmospheric greenhouse effect. However, H<sub>2</sub> could only have acted as a greenhouse gas for a geologically brief period, as it would have likely been converted by methanogens to another greenhouse gas, CH<sub>4</sub>. CH<sub>4</sub> provides some of modern greenhouse warming, but it may have been even more prevalent in the pre-oxygenated atmosphere prior to ~2.5 Ga, when it was possible to build up to greater concentrations without being quickly oxidized. CH<sub>4</sub> has a lifetime of only about 10 years in today's atmosphere, but can have a lifetime up to 1000 times longer in an anoxic atmosphere (Haqq-Misra et al., 2008). This, and the fact that CH<sub>4</sub> likely had a stable source via early methanogenic life (Kharecha et al., 2005), means that it may have been relatively abundant during the Archean. However, CH<sub>4</sub> could still only have been a minor atmospheric constituent compared to CO<sub>2</sub>; when the ratio CH<sub>4</sub> to CO<sub>2</sub> exceeds ~0.1, CH<sub>4</sub> begins to polymerize and form haze as it is photolyzed, resulting in a net cooling effect as

it absorbs and reemits incoming solar radiation. Therefore, while CH<sub>4</sub> may have contributed to the early greenhouse effect, it is unlikely to have been the primary source of warming.

CO<sub>2</sub> plays a central role in modern climate change (both natural and anthropogenic), but it likely also dominated the early Earth's greenhouse effect. CO<sub>2</sub> outgassed from volcanoes would have accumulated to much higher levels than today in a volcanically active, pre-oxygen atmosphere (Kasting, 1993), and a CO<sub>2</sub> concentration just 100 times higher than today's would have been sufficient to keep the early Earth habitable with regard to surface temperature. While other reduced greenhouse gases would have been oxidized following the GOE (removing their contribution to the greenhouse effect), CO<sub>2</sub> would not be as affected by this shift in atmospheric composition. In fact, the Huronian Snowball Earth event at ~2.4 Ga—likely triggered by the oxidation and large-scale removal of atmospheric CH<sub>4</sub> and subsequent weakening of the greenhouse effect (Bekker et al., 2005)—was probably ended by a buildup of CO<sub>2</sub> from volcanic outgassing (Kirschvink et al., 2000; Kopp et al., 2005). In the geologic record, the glacial deposits of the ~2.48 billion-year-old Huronian supergroup are overlain by siderites and dolomites that indicate an oxygenated surface ocean and massive biological CO<sub>2</sub> consumption, respectively, after the retreat of the global ice cover. Ultimately, it is probable that CO<sub>2</sub> has been the dominant greenhouse gas throughout much of Earth history, and that it—along with changing O<sub>2</sub>—dictated much of the major shifts in the atmospheric evolution and climate history on Earth.

The central three chapters of this dissertation focus on select problems in climate history related to the role of CO<sub>2</sub> and O<sub>2</sub> through time. The first examines a new potential means of estimating ancient pCO<sub>2</sub>, using one-dimensional modeling to recreate the pre-

oxygen Archean atmosphere around  $\sim 2.7$  Ga. The second chapter utilizes a similar modeling approach, using a coupled 1-D photochemical model and 1-D climate model, to study the influence of  $O_2$  on the greenhouse effect of the much more recent Cretaceous about  $\sim 100$  Ma. The final chapter applies a different modeling technique, considering how the interplay of  $CO_2$ ,  $O_2$ , and the C cycle have shaped climate over the course of the Phanerozoic.

As previously mentioned, what we know about Earth's past climate is the result of careful juxtaposition of climate modeling and geochemical analysis. That said, information on Earth's climate becomes increasingly limited with age, and the data that exist are often progressively more difficult to decipher. Paleosols—ancient soils containing carbonate minerals—have long been the most widely used and cited Archean proxies for  $pCO_2$  (Sheldon, 2008; Driese et al., 2011). But the estimates from paleosols are hard to constrain, and there is considerable disagreement between individual paleosol studies (Kanzaki & Murakami, 2015) as well as between paleosols and climate models (Kasting, 2015; Catling & Kasting, 2017). Tomkins et al. (2016) analyzed oxidized iron micrometeorites from the late Archean, theorizing that they indicated a high ( $\sim 21\%$ ) abundance of upper atmospheric  $O_2$  at 2.7 Ga, even though total atmospheric  $O_2$  is thought to have been negligible until at least  $\sim 2.5$  Ga. Our analysis (in Chapter 2) indicates that these micrometeorites are more likely a proxy for Archean  $CO_2$  and, possibly, surface pressure. If so, this may provide a new point of comparison for geochemical proxies and climate models. We investigate  $pCO_2$  during the Neoproterozoic using compositional data from the 2.7 Ga micrometeorites collected by Tomkins et al., along with novel mathematical interpretations. Assessing the

potential value of new atmospheric proxies is vital to understanding how Earth's atmosphere and climate have evolved over time.

In thinking about the greenhouse effect across time, it is also important to evaluate competing effects that gases may exert on total atmospheric warming. While proxies indicate abundances, models can help us resolve the interplay between gases and how this affects energy balance. We therefore turn to the Phanerozoic in Chapter 3, long after the rise of O<sub>2</sub> as a major atmospheric constituent. First, we do an in-depth study of the effect of O<sub>2</sub> on surface temperatures, with a focus on the Cenomanian (~100 Ma). We compare our results to those of Berner (2006) and Poulsen et al. (2015), who had conflicting views on the relative importance of CO<sub>2</sub> versus O<sub>2</sub> on Phanerozoic climate. We compare the influence of O<sub>2</sub> to that of CO<sub>2</sub> on surface temperature, as well as the evolution of the biosphere at that time. We argue that Berner's assertion that CO<sub>2</sub> and weathering were the primary controls on Phanerozoic climate is robust, with large-scale changes in atmospheric O<sub>2</sub> accentuating the strength of the greenhouse effect.

Finally, we combine our work utilizing both geochemical proxies and climate models to try to understand long-term climate evolution during the Phanerozoic. We assess existing models of the global C cycle and atmospheric CO<sub>2</sub>. In particular, we consider Berner's GEOCARB model, the COPSE model by Bergman et al., and the more recent C cycle model by Krissansen-Totten & Catling. We then construct our own box model to study CO<sub>2</sub> and carbon burial in the Phanerozoic, extrapolating relationships between data and systems over time to better understand long-term changes in climate and the atmospheric greenhouse effect. We also use this model to revisit calculations by Berner, Krissansen-Totten & Catling, and others, of the activation energy for continental

weathering and use it to evaluate the role of the continents and seafloor in controlling global carbon cycling.

Together, these three chapters represent three different approaches to modeling climate change throughout Earth's history, and emphasize the importance of using both climate models and geochemical proxies to study this fascinating problem.

## Chapter 2.

### Iron micrometeorite oxidation as a proxy for atmospheric CO<sub>2</sub> during the Neoproterozoic

Chapter 2 is published in the *Proceedings of the National Academy of Sciences (PNAS)* as of January 2020 (<https://doi.org/10.1073/pnas.1910698117>), with coauthors Don Brownlee and James Kasting. I ran the modeling cases described in the chapter and wrote the analysis. I thank both coauthors for their input developing the calculations, and their contributions to some of the text.

#### 1. Background

Earth's atmospheric O<sub>2</sub> concentration is widely believed to have been low or negligible prior to ~2.5 Ga, based on a variety of geologic evidence (Holland, 2006), including multiple sulfur isotopes preserved in sediments (Farquar et al., 2000; Pavlov et al., 2001; Harman et al., 2018). These constraints on O<sub>2</sub> are relevant to the lower atmosphere—as sediments only interact with the air directly above the ground—but do not necessarily apply to the upper atmosphere. Tomkins et al. (2016) proposed that ancient spherical micrometeorites could be used to determine past oxygen concentrations in the upper atmosphere. They extracted fifty-nine iron-type micrometeorites from Pilbara limestone, dated at ~2.72 Ga, and used the iron oxides contained within them to estimate the amount of O<sub>2</sub> the micrometeorites would have encountered as they were melted during entry. These type I cosmic spheres were small Fe-Ni metal meteoroids that totally melted to form spheres during hypervelocity entry into the atmosphere. Their oxygen content was obtained solely in the upper atmosphere during a brief period of frictional melting. Tomkins et al. (2016) concluded that upper atmospheric O<sub>2</sub> concentrations must have been close to the modern value, 21 percent by volume, to create the largely oxidized composition of the micrometeorites. To explain the discrepancy with inferred low O<sub>2</sub> concentrations at the surface, they suggested that vertical atmospheric mixing in the Neoproterozoic could have

been inhibited by the presence of a stratospheric organic haze, which would have caused a temperature inversion by absorbing incoming sunlight and, thus, isolated upper atmospheric O<sub>2</sub> from O<sub>2</sub> in the lower atmosphere.

In more detail, Tomkins et al. argued that the micrometeorites would have passed through the upper atmosphere, accelerated by Earth's gravitational field, and reached maximum temperature and velocity between 85 and 90 km above the surface (Love & Brownlee, 1991). They posited that melting and quench-cooling of these sand grain-size meteorites would have occurred within approximately two seconds between 75 and 90 km, so this is where oxidation should have occurred. Tomkins et al. argued that the micrometeorites must have been oxidized when passing through the atmosphere, and not by later alteration, based on several lines of evidence. First, the existence of a layer of encasing wüstite (FeO) in some of the micrometeorites supports an extraterrestrial origin of the spherules, as this iron oxide is not formed in sedimentary environments. Second, the presence of FeO and magnetite (Fe<sub>3</sub>O<sub>4</sub>), and the absence of hematite, in any of the collected meteorites indicates oxidation is unlikely to have occurred in a sedimentary environment where water may have been present. Third, the preservation of delicate surface textures indicates that later chemical alteration or diagenesis probably did not occur, as these textures would not have survived. Tomkins et al. then developed a mathematical model to determine the amount of O<sub>2</sub> that would need to have been encountered during atmospheric entry to produce the iron oxides found in the micrometeorites. This included an equilibrium chemical model coupled to a numerical model of meteorite ablation. Tomkins et al. argued that CO<sub>2</sub> would have been an ineffective oxidant on its own because of its supposedly

sluggish rate of reaction, and therefore free O<sub>2</sub> would have been needed to oxidize the meteorites.

To test both this theory of micrometeorite oxidation, we used our own 1-D photochemical model to create a suite of Archean atmosphere profiles with varying concentrations of atmospheric CO<sub>2</sub>. Rather than focus exclusively on upper atmospheric O<sub>2</sub>, as Tomkins et al. did, we included O in our calculations as well, in order to assess the availability of all forms of oxygen. Furthermore, we reevaluated the efficacy of CO<sub>2</sub> as an oxidant, and considered atmosphere-particle interactions to determine likely conditions for micrometeorite oxidation in the upper Archean atmosphere. We then simulated the effect of possible CO<sub>2</sub> concentrations on surface temperature and pressure, for different values of  $pN_2$ , using a 1-D radiative-convective climate model.

## **2. Micrometeorite oxidation**

### **2.1. Entry physics**

Particles with a diameter of less than 1 mm are too small to generate a bow shock during atmospheric entry (Love & Brownlee, 1991), meaning that micrometeorites smaller than this do not create the shock waves or gas caps that typically form around larger particles under these conditions. The interaction between the smaller micrometeorites and the atmosphere is therefore thought to be simple, as no shock-induced chemical alteration occurs to the surrounding air during entry. Instead, the micrometeorite is simply slowed by, and may react with, the gas it encounters. Deceleration is a function of momentum exchange, and frictional heating during deceleration is what causes the micrometeorite to briefly melt and quench-crystallize during atmospheric entry. The speed of the micrometeorite decreases by a factor of 1/e for each particle mass column of gas that the micrometeorite impacts, assuming all of the gas momentum is transferred to the

micrometeorite. A micrometeorite's speed would decrease to 0.37 and 0.135 of the initial speed after colliding with gas equal to 1 and 2 particle masses respectively. Faster micrometeorites would encounter more air while molten because of their greater momentum.

The temperature of an entering micrometeorite depends on its velocity and on the ambient gas density, such that

$$\text{radiated power} = \frac{1}{4} * \left(\frac{1}{2}\rho_{air}\right) * v^3 \quad (1)$$

Here,  $\rho_{air}$  is the ambient air density and  $v$  is the micrometeorite's entry velocity. The melting temperature of Fe and its oxides is approximately 1500°C, so the micrometeorite's speed must be above 6 km/s at 80 km and above 9 km/s at 85 km (in the modern Earth's atmosphere) to reach the melting point. To take up oxygen and form the mix of magnetite, wüstite, and metal observed in the Tomkins et al. spherules, the micrometeorites need to be molten.

Depending on size and particle speed, most micrometeorites should contact one to two equivalent masses of air in the time that they are traveling fast enough to be heated to their melting points. A complication is that the micrometeorites are potentially evaporating some fraction of their mass during entry, and this is strongly dependent on entry angle and initial micrometeorite size. Evaporative mass loss during entry would likely decrease the number of Fe atoms that would need to be reacting with oxidants for the micrometeorite to be fully oxidized. But, newly acquired oxygen may be lost as well, and so the uncertainties associated with mass loss make it difficult to constrain in our calculations without knowing more about entry angle and initial size. For this study, we assume that the micrometeorite

retains most or all the oxygen it encounters, along with its own initial mass, so oxidizing the micrometeorites is therefore a function of how much oxygen the meteorite encounters in the upper atmosphere while molten.

Tomkins et al. assumed that the altitude region within which the micrometeorites were molten would be the same in the Archean as it is in the modern atmosphere (between ~75 and 90 km, as Love & Brownlee (1991) specified). But the deceleration—and frictional heating—of a micrometeorite depends on the number of particles it encounters during entry. Thus, the window in which oxidation occurs is not located at a fixed altitude range, but rather at a fixed pressure range. Pressure in our model Archean atmosphere falls off more rapidly than in the modern atmosphere (see Appendix 1, Fig. A1b) because of the cooler, ozone-poor stratosphere, along with the higher mean molecular weight caused by increased CO<sub>2</sub>. Thus, the ‘oxidation altitude range’ of 75 to 90 km for the modern atmosphere should really be redefined as an ‘oxidation pressure range’ from  $\sim 2.3 \times 10^{-5}$  bar to  $\sim 1.6 \times 10^{-7}$  bar. The corresponding altitude of oxidation therefore varies with the CO<sub>2</sub> concentration and is generally lower than assumed by Tomkins et al. (Table 2.1).

---

**Table 2.1:** Approximate altitude of lower and upper bounds of oxidation pressure range for atmospheres with various CO<sub>2</sub> mixing ratios. Altitude in kilometers.

CO <sub>2</sub> (%)	Modern	1%	10%	20%	25%	30%	35%	50%
<b>Lower</b>	75	59	55	54	52	51	50	46
<b>Upper</b>	90	72	70	67	65	64	62	58

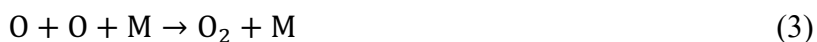
---

## 2.2. Micrometeorite oxidation chemistry

In a Neoproterozoic atmosphere with a primarily N<sub>2</sub>-CO<sub>2</sub> composition, upper atmospheric chemistry would be dominated by the reaction:



Direct recombination of CO with O is spin-forbidden, and therefore slow, so O primarily recombines with itself to form O<sub>2</sub>:



In terms of micrometeorite oxidation, it should not matter much whether oxygen was present as O or O<sub>2</sub>, as the high temperature of the molten iron micrometeorites should allow all of the gaseous species interacting with them to equilibrate with each other on short time scales.

Tomkins et al. only considered O<sub>2</sub> as a potential oxidant, assuming that the concentration of other forms of oxygen would be negligible. Their Fig. 4 shows calculations by Zahnle et al. (2006) that appear to support this assumption. But our own photochemical model of the 2.7 Ga atmosphere indicates that both O<sub>2</sub> and O would be present in the upper atmosphere (see Section 3 of this chapter). The Zahnle et al. model (Zahnle et al., 2006; Zahnle, 1986), which is a derivative of our model, would almost certainly yield the same result. However, those authors were focused on the lower atmosphere and simply did not include O in their figure.

It is also possible—even likely—that CO<sub>2</sub> itself was an oxidant for the micrometeorites. Tomkins et al. argued that Fe oxidation by CO<sub>2</sub> would be slow, based on studies of Fe metallurgy at temperatures below 1470 K (Abuluwefa et al., 1997; Bredesen

& Kofstad, 1991). But iron micrometeorites (and iron oxide) need to reach at least ~1770 K during entry in order to melt (Love & Brownlee, 1991). Shock tube experiments above the Fe melting temperature indicate that oxidation rates of Fe to FeO by O<sub>2</sub> (Akhmadov et al., 1988) and CO<sub>2</sub> (Giesen et al., 2002) are roughly equal and are up to 3 orders of magnitude faster than reduction of FeO by CO (Smirnov, 2008). Other possible oxidation reactions include O<sub>2</sub> oxidation of Fe to FeO<sub>2</sub> (Smirnov, 2012), and CO<sub>2</sub> oxidation of FeO to FeCO<sub>3</sub> (Rollason & Plane, 2000) at similar reaction rates. But it is worth noting that O can also reduce FeO to form O<sub>2</sub> in the upper mesosphere (Self & Plane, 2003), albeit at much lower temperatures than the micrometeorites would experience during entry. Until experimental chemical reaction rate data are obtained for the appropriate temperature and pressure range, we cannot definitively state which oxidation and reduction reactions are likely to dominate. Nonetheless, the CO<sub>2</sub> oxidation pathway indicates the value such experiments would have for micrometeorite analysis—and, for now, existing data points to its potential significance for the Tomkins micrometeorites. In short, it suggests that at least one O atom from each CO<sub>2</sub> molecule may contribute to micrometeorite oxidation during entry. It also suggests that reduction of the newly formed Fe oxides by CO is unlikely to occur during the short time that the micrometeorite is molten, and that accumulating an adequate amount of oxidant in the oxidation pressure range is more important than the ratio of oxidants to reductants.

If so, then one should consider the oxidation potential from O, O<sub>2</sub>, and CO<sub>2</sub> within the oxidation pressure window. And this, in turn, makes the calculation quite simple, as nearly all O and O<sub>2</sub> in the upper atmosphere is derived from CO<sub>2</sub>. O atoms are neither created nor destroyed in the atmosphere above the altitude at which they are removed by

rainout of H<sub>2</sub>O. Thus, from mass balance, it is easy to demonstrate (see Appendix 1) that if O<sub>2</sub> concentrations are low near the surface, and if H<sub>2</sub>O concentrations are low at the tropopause, then

$$f(\text{O}) + 2f\text{O}_2 + f\text{CO}_2 = \text{const.} = f\text{CO}_2^0 \quad (4)$$

Here,  $f_i$  is the volume mixing ratio of species  $i$  and  $f\text{CO}_2^0$  is the mixing ratio of CO<sub>2</sub> at the surface. More precisely,  $f\text{CO}_2^0$  is the mixing ratio of CO<sub>2</sub> at the base of the stratosphere; however, the difference between this value and the surface CO<sub>2</sub> mixing ratio is negligible. Thus, in our analysis, the key parameter is the CO<sub>2</sub>:N<sub>2</sub> ratio at the surface. CO<sub>2</sub> oxidizes the micrometeorites, whereas both CO<sub>2</sub> and N<sub>2</sub> decelerate the meteorites. The CO<sub>2</sub>:N<sub>2</sub> ratio determines whether or not they are oxidized, independent of particle size.

To make this analysis more concrete, consider the modern atmosphere, within which we know that incoming metal micrometeorites are partly to fully oxidized to form a mix of Fe<sub>(1-x)</sub>O (wüstite), Fe<sub>3</sub>O<sub>4</sub> and sometimes iron metal during entry (Love & Brownlee, 1991). For total oxidation, this requires the addition of 1 to 1.3 O atoms per iron atom. In the modern atmosphere, this oxidation is accomplished almost exclusively by O<sub>2</sub>. Assume for now that the particle remains molten, and hence reactive, only during its encounter with the first equivalent air mass. Because the atomic mass of Fe (~56 amu) is just under twice the average atmospheric mass (29.6 for N<sub>2</sub>-O<sub>2</sub>-<sup>40</sup>Ar), the micrometeorite should encounter about twice as many air molecules as it contains Fe atoms while it is still molten. Of these, 21% are O<sub>2</sub> molecules. Therefore, the ratio of O<sub>2</sub> molecules encountered to Fe atoms within the micrometeorite is equal to  $2 \times 0.21 \cong 0.4$ . The ratio of O:Fe is twice that, or 0.8. This ratio is close enough to the O:Fe ratio required to form the observed oxides (as the

micrometeorites contain some varying fraction of Ni instead of Fe), provided that oxidation is total and nearly 100% efficient. We can express this relationship compactly by writing

$$\left(\frac{56}{29.6}\right) \cdot 2fO_2 \cong 0.8 \quad (5)$$

Now, let us apply this same logic to the Neoproterozoic atmosphere, assuming that it consists primarily of N<sub>2</sub> and CO<sub>2</sub> within the oxidation pressure window (Figs. 2.1 and A1.2 show that this is approximately true). The mean molecular weight of the atmosphere is then

$$M_{at} \cong 44fCO_2 + 28(1 - fCO_2) \quad (6)$$

Here,  $fCO_2$  is effectively  $fCO_2^0$ , the CO<sub>2</sub> mixing ratio at the ground. We will use these terms interchangeably from here on. Using the identical requirement of 0.8 O atoms per Fe atom for complete oxidation then yields

$$\left(\frac{56}{M_{at}}\right) fCO_2 = \left(\frac{56 fCO_2}{44 fCO_2 + 28 (1 - fCO_2)}\right) \geq 0.8$$

or

$$\left(\frac{2 fCO_2}{1 + \left(\frac{4}{7}\right)fCO_2}\right) \geq 0.8 \quad (7)$$

Solving for  $fCO_2$  gives a minimum value of 0.52 needed to oxidize a micrometeorite encountering one equivalent mass of air during entry.

Suppose now that the meteorite remains molten during its encounter with two equivalent air masses. The required CO<sub>2</sub> mixing ratio is lower, but not exactly by a factor of 2. The analog to eq. 7 is

$$\left(\frac{56}{M_{at}}\right) \cdot 2fCO_2 = \left(\frac{56 fCO_2}{44 fCO_2 + 28 (1 - fCO_2)}\right) \geq 0.8$$

or, more simply,

$$\left( \frac{4f\text{CO}_2}{1 + \left(\frac{4}{7}\right)f\text{CO}_2} \right) \geq 0.8 \quad (8)$$

Solving for  $f\text{CO}_2$  in this case yields a value of 0.23. It is slightly less than half the value predicted from eq. 7 because the mean molecular weight of the atmosphere is lower, causing the micrometeorite to encounter more air molecules as it decelerates.

Similar calculations can be performed for the case when  $\text{CO}_2$  is not considered to be an oxidant for Fe. We do this here because it remains unclear which assumption is actually correct. In this case,  $\text{CO}_2$  and  $\text{N}_2$  would still be the dominant constituents in the oxidation pressure range, so  $M_{\text{at}}$  remains unchanged, but the fraction of oxidant is  $f\text{O}_{\text{oxy}} \equiv (f\text{O} + 2f\text{O}_2)$ , rather than  $f\text{CO}_2$ . Thus, if the particle remains molten during encounter with one equivalent air mass, we can write

$$\left( \frac{56}{M_{\text{at}}} \right) f\text{O}_{\text{oxy}} = f\text{O}_{\text{oxy}} \left( \frac{56}{44 f\text{CO}_2 + 28 (1 - f\text{CO}_2)} \right) \geq 0.8$$

or

$$\left( \frac{2 * f\text{O}_{\text{oxy}}}{1 + \left(\frac{4}{7}\right)f\text{CO}_2} \right) \geq 0.8 \quad (9)$$

The value of  $f\text{O}_{\text{oxy}}$  needed to oxidize the micrometeorites still depends on the mixing ratio of  $\text{CO}_2$ , but the relationship is more complicated, as O and  $\text{O}_2$  are both produced, directly or indirectly, from  $\text{CO}_2$  photolysis. Thus, a photochemical model is needed to determine this relationship. We have performed such modeling (see Section 3 of this chapter) and, not surprisingly, the required atmospheric  $\text{CO}_2$  mixing ratios for micrometeorite oxidation using only O and  $\text{O}_2$  are much higher. For a 2-air-mass oxidation event, the required value of  $f\text{O}_{\text{oxy}}$  in eq. 9 is cut exactly in half, as the mean molecular mass does not change. But, as

we shall see, attaining even this lower value of  $f_{\text{O}_{\text{oxy}}}$  is difficult to achieve in a realistic Archean atmosphere.

### **3. Photochemical calculations**

#### **3.1. Methods**

Photochemical model calculations are required if  $\text{CO}_2$  is not included as a possible oxidant for Fe micrometeorites. For our calculations, we used a version of our 1-D photochemical model developed for high- $\text{CO}_2$ , low- $\text{O}_2$  atmospheres (Harman et al., 2015). Our model contains 49 chemical species involved in 220 reactions (see Appendix 1 Table A.1, Supp. Info of Stanton et al., 2018 for the full list). It extends upwards from the Earth's surface to 100 km in 1-km thick layers. Vertical mixing is parameterized as a combination of eddy and molecular diffusion, using a profile appropriate for the modern atmosphere (Massie & Hunten, 1981). Absorption and scattering of solar radiation were calculated using a 2-stream algorithm (Toon et al., 1989), assuming a fixed solar zenith angle of 50 degrees. The time-dependent, coupled chemistry/diffusion equations were integrated to steady state using the (fully implicit) reverse Euler method. We also calculated changes to the solar UV flux using a parameterization developed by Ribas et al. (2005). Properly scaling the UV flux is essential for this analysis, as the rate of free oxygen production via  $\text{CO}_2$  photolysis depends on this parameter. At 2.7 Ga, the Sun would have been only ~81% as bright as today in the visible (Gough, 1981; Kasting, 2010), but ~50% brighter than today at far-UV wavelengths ( $< 1750 \text{ \AA}$ ), as main sequence stars like our Sun tend to emit greater amounts of UV radiation earlier in their lifetimes because of their higher rotation rates and increased magnetic activity (Ribas et al., 2005).

Calculations were performed for a 1-bar,  $\text{CO}_2\text{-N}_2$  atmosphere with 1-50%  $\text{CO}_2$ , along with low concentrations of methane (see below). We should note that we are solving

minor-constituent diffusion equations for major species, which introduces some error in the ratio of CO<sub>2</sub>:CO:O at high altitudes in the model atmosphere. However, this should have little effect on our results because, as discussed earlier, it is only the sum of CO<sub>2</sub>, O<sub>2</sub>, and O that matters, as iron reduction by CO is slow. Furthermore, the largest errors in these ratios occur close to the top of the model atmosphere, well above the altitude range at which most meteorite oxidation occurs.

We assumed a simplified temperature structure that decreases from 285 K at the surface (actually, at 0.5 km) to 175 K at 9.5 km and then remains constant above that height (Fig. A1.1a). This is consistent with predictions from 1-D climate models (e.g., Kasting, 1984), which suggest that the temperature profile of an ozone-free atmosphere should follow a moist adiabat from the surface up to the tropopause and then become roughly isothermal above that altitude. We have not attempted to keep the surface temperature consistent with the assumed CO<sub>2</sub> concentration and solar flux in these calculations, reasoning that upper atmospheric composition should be relatively insensitive to this parameter. We examine the implications of atmospheric composition and photochemistry on surface temperature in our climate calculations (see Section 4 of this chapter).

An upward CH<sub>4</sub> flux of  $3.0 \times 10^9$  molecules cm<sup>-2</sup>s<sup>-1</sup> was assumed for our photochemical calculations. This is about 3% of the present CH<sub>4</sub> flux, and well below the estimated CH<sub>4</sub> flux during the Archean (Kharecha et al., 2005). Unlike Tomkins et al. (2016), we do not rely on a stratospheric temperature inversion to help build up upper atmospheric O<sub>2</sub>, and so we avoid the regime in which  $f_{\text{CH}_4}/f_{\text{CO}_2} > 0.1$  and in which organic haze may form (Haqq-Misra et al., 2008). The actual amount of CH<sub>4</sub> present should have

little effect on micrometeorite oxidation; however, it does have implications for climate at that time, so we return to this issue in Section 4 of this chapter.

### 3.2. Results

Vertical profiles of major atmospheric constituents for our 25% CO<sub>2</sub> case are shown in Fig. 2.1. Key reducing and oxidizing species in the upper atmosphere at different CO<sub>2</sub> concentrations are shown in Fig. A1.2 in Appendix 1. Both O and O<sub>2</sub> are present within the micrometeorite oxidation pressure range, with O dominating in the upper part of this region and O<sub>2</sub> in the lower part. In all these simulations, the sum of  $fO + 2fO_2$  ( $fO_{oxy}$ ) is much less than  $fCO_2$ . That is because virtually all the O and O<sub>2</sub> is coming from CO<sub>2</sub>, and because CO<sub>2</sub> itself is relatively resistant to photolysis (CO<sub>2</sub> photolyzes only below ~200 nm, where the solar UV flux is relatively low). Accumulating large amounts of O and O<sub>2</sub> in the stratosphere and above would require unrealistically low eddy mixing. Tomkins et al. (5) argued that such low mixing might result from a stratospheric temperature inversion caused by the presence of organic haze. But the eddy diffusion profile used here already accounts for this phenomenon, as it was derived for the modern stratosphere which has a temperature inversion caused by ozone, so our calculations may already overestimate upper atmospheric oxygen.

Even with CO<sub>2</sub> concentrations as high as 50%, the fraction of the atmosphere within the oxidation pressure range that is composed of O and O<sub>2</sub> combined is less than 2% (Fig. A1.2). Oxidizing the micrometeorites with oxygen alone (eq. 9) requires reaching a value of  $fO_{oxy}$  roughly 10 times higher than this. Doing so would thus require both an extremely high CO<sub>2</sub> concentration and extremely low eddy mixing. It is therefore difficult, or even impossible, to oxidize the Tomkins et al. micrometeorites using just O and O<sub>2</sub>, unless O<sub>2</sub>

was abundant throughout the atmosphere. But this possibility is ruled out by geologic data, including sulfur isotope studies, as mentioned earlier. It is much more likely that the micrometeorites were oxidized by  $\text{CO}_2$ , in which case the limits on  $f\text{CO}_2$  derived in Sect. 2.2 remain applicable.

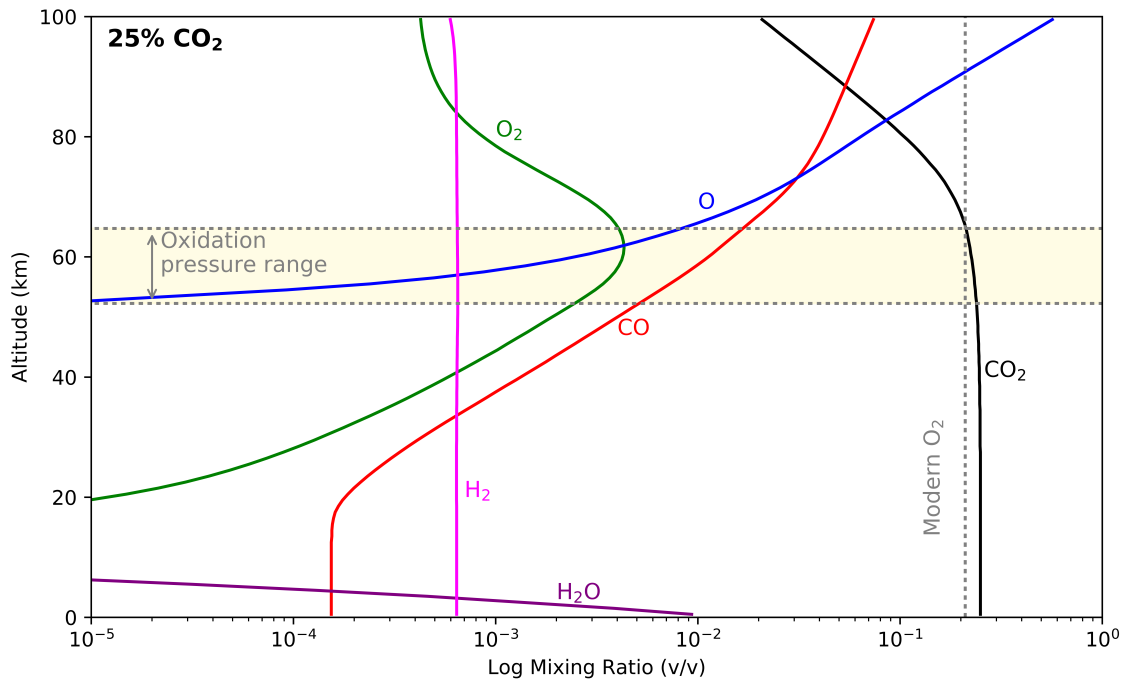


**Figure 2.1.** Vertical profiles of major constituents mixing ratios for  $f\text{CO}_2 = 25\%$ , close to our minimum estimated value. The pressure range for micrometeorite oxidation is indicated by the shaded yellow region. The modern  $\text{O}_2$  mixing ratio is shown by the vertical dotted line. Atmosphere also contains 0.8 bar  $\text{N}_2$ .

## 4. Discussion

### 4.1. Constraints on $p\text{CO}_2$ from Neoproterozoic climate

The high atmospheric  $\text{CO}_2$  concentrations required to oxidize the micrometeorites can be compared with  $\text{CO}_2$  levels required to explain the climate of the Neoproterozoic Earth. Ojakangas et al. (2014) have reported diamictites—unsorted terrigenous conglomerate or

breccia with a fine matrix, which are commonly interpreted as glacial in origin—dated at 2.7 Ga in the Dharwar Supergroup in India. This is approximately the same age as the micrometeorites ( $2.721 \pm 0.004$  Ga) analyzed by Tomkins et al. (2016). Even more convincing evidence for glaciation is found in 2.9 Ga rocks from the Pongola Supergroup in southern Africa (Young et al., 1998), which include diamictites with geochemical weathering patterns indicative of continental glaciers. Together, these observations suggest that the climate of the Neoproterozoic was not too different from today. In a long-term sense, Earth's climate is considered to be glacial today because ice caps exist at both poles.

Approximate constraints on global mean surface temperature,  $T_s$ , during glacial periods have been estimated by Kasting (1987), and we follow the same approach here. The modern value of  $T_s$  is  $\sim 288$  K. Polar ice caps were absent during the early Cenozoic and preceding Mesozoic eras. The Antarctic ice cap started to grow about 35 million years ago, at which time  $T_s$  was about 5 degrees warmer than today, or 293 K, based on oxygen isotopes in deep sea carbonate cores. This suggests that 293 K is a reasonable upper limit for continental-scale glaciation. The argument is not iron-clad, because changes in land-sea distributions—in particular, the opening of the Drake passage at about this same time—could also have helped trigger Antarctic glaciation. But we will use this as a reasonable guess at the upper limit on  $T_s$  at 2.7 Ga. At the same time, we can take  $0^\circ\text{C}$ , or 273 K, as a reasonable lower limit on  $T_s$ , as climate models predict that Earth's climate would go into a Snowball state if global mean temperatures were to drop much below this value. Climate theory (Walker et al., 1981) then predicts that silicate weathering would slow, and atmospheric  $\text{CO}_2$  would build up if this were the case.

We used a 1-D climate model (described in more detail in Chapter 3) to study the effects of high atmospheric CO<sub>2</sub> levels on Neoproterozoic climate. To do so, we needed to first establish a relationship between  $f\text{CO}_2$  (the CO<sub>2</sub> mixing ratio) and surface pressure. This relationship is nonlinear because the total atmospheric pressure changes as  $f\text{CO}_2$  increases, given a fixed amount of N<sub>2</sub>. The required relationship (derived in Section 1.2 of Appendix 1) is

$$p\text{CO}'_2 = p\text{N}'_2 \cdot \left(\frac{44}{28}\right) \cdot \left(\frac{f\text{CO}_2}{1-f\text{CO}_2}\right) \quad (10)$$

Here,  $p\text{CO}'_2$  and  $p\text{N}'_2$  are the ‘partial pressures’ of CO<sub>2</sub> and N<sub>2</sub>. The term ‘partial pressure’ is used loosely here, as these are not true partial pressures. Rather, they represent the surface pressure that would be exerted by that amount of gas were it to exist by itself in Earth’s atmosphere. Lighter gases cause heavier ones to diffuse away from Earth’s surface, whereas heavier gases cause lighter ones to diffuse towards it; hence, the actual partial pressure of a gas can be different from its pressure in isolation, seemingly contrary to Dalton’s Law. The advantage of defining these terms in this way is that surface pressure,  $P_s$ , is then given by

$$P_s = p\text{CO}'_2 + p\text{N}'_2 \quad (11)$$

With these relationships in hand, we used the 1-D climate model to calculate mean surface temperature as a function of  $f\text{CO}_2$ . The results are shown in Fig. 2.2. The assumed solar luminosity was ~0.81 times present at 2.7 Ga, following Gough (1981). The top panel shows  $T_s$  versus  $f\text{CO}_2$  for different amounts of N<sub>2</sub> and CH<sub>4</sub>. CH<sub>4</sub> is a greenhouse gas which is scarce enough to have little effect on surface pressure, but abundant enough (1000 ppmv

in these calculations) to raise  $T_s$  by 8–10 degrees. This  $\text{CH}_4$  concentration is an approximate upper limit derived from Archean ecosystem modeling (Kharecha et al., 2005). The micrometeorite oxidation constraints are on  $f\text{CO}_2$ , not  $p\text{CO}_2$ , and are displayed as vertical dotted lines in Fig. 2.2.

The results from the climate model show that if  $pN_2'$  were the same as today ( $\sim 0.8$  bar), the climate at 2.7 Ga would have been warm—300 K or more—even if  $f\text{CO}_2$  was equal to the minimum value,  $\sim 0.23$ , estimated from 2-air-mass oxidation. For  $f\text{CO}_2 = 0.52$ , the minimum value for 1-air-mass oxidation, then  $T_s \geq 320$  K. Either of these global mean surface temperatures would almost certainly have precluded polar glaciation.

The results are more promising for a potentially glacial climate if  $pN_2'$  was half its present value, or 0.4 bar. For  $f\text{CO}_2 = 0.23$ , the predicted  $T_s$  for the no-methane case is  $\sim 290$  K, which is within the glacial ‘window’. The high-methane case is several degrees warmer and is outside our nominal window. However, given the uncertainties in estimating this window, along with the uncertainties in age dating of the micrometeorites and the glaciations, this result also seems plausible.

All of this suggests that if the micrometeorite oxidation story—with  $\text{CO}_2$  facilitating Fe micrometeorite oxidation by up to 2 air masses during entry—is correct,  $pN_2$  must have been appreciably lower than today back at 2.7 Ga. The history of  $pN_2$  in Earth’s atmosphere is still an area of active debate, and some theoreticians have argued the opposite. Goldblatt et al. (2009) argued that if the abundance of  $N_2$  had been doubled during the Archean, it could have boosted greenhouse warming by  $\sim 4.4$  K through collisional effects with  $\text{CO}_2$  (a concept we explore for Phanerozoic climate in Chapter 3, though by

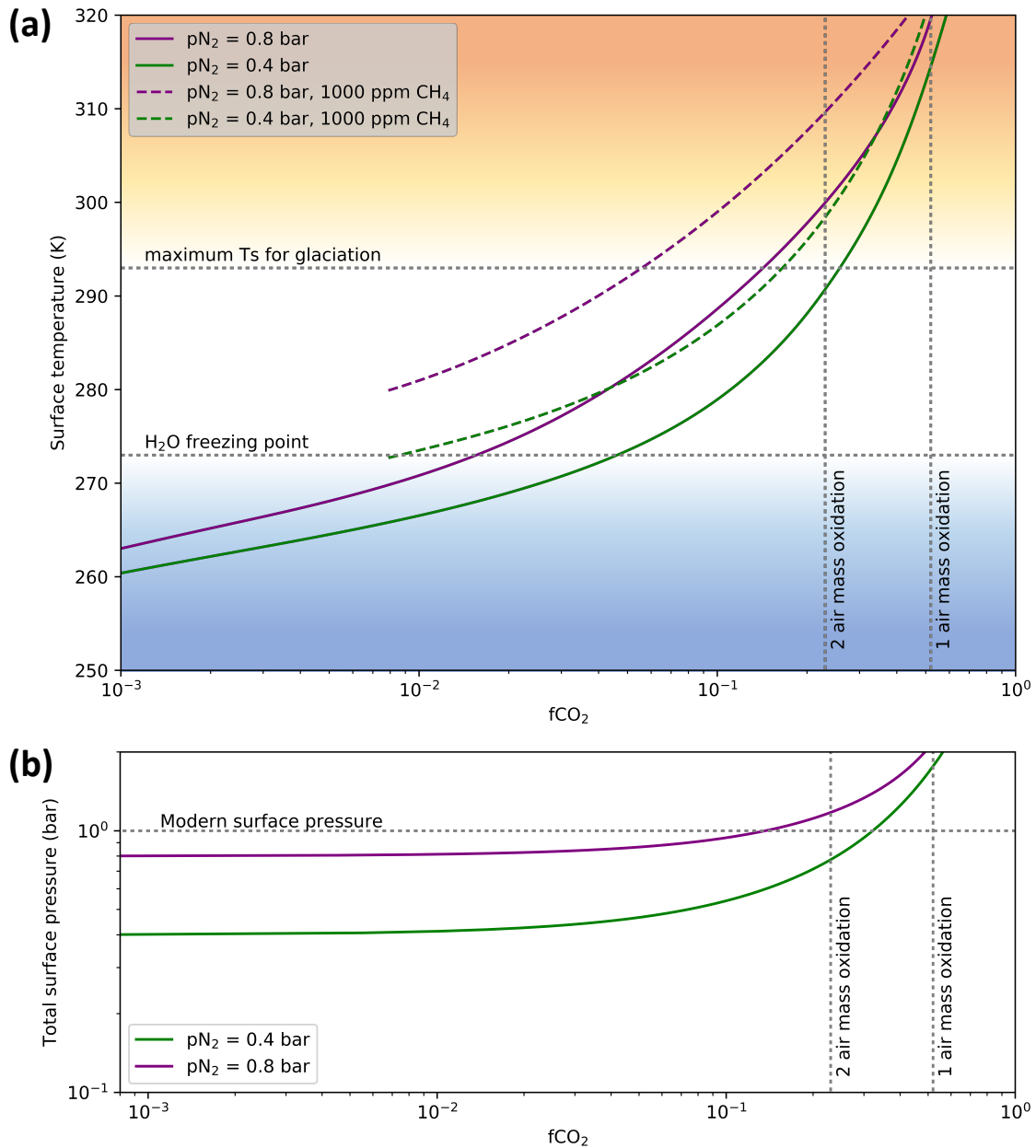


**Figure 2.2.** Results from our 1-D climate model: (a) Surface temperature as a function of  $f\text{CO}_2$ , for atmospheres with 0.8 bar (purple) and 0.4 bar (green) of  $\text{N}_2$ . Solid curves are for zero  $\text{CH}_4$ ; dashed curves are for 1000 ppm  $\text{CH}_4$ . Blue shaded region denotes sub-freezing global mean surface temperatures; orange shaded region indicates a global mean surface temperature too high to facilitate glaciation (see text). The 1 and 2 air mass oxidation lines represent the  $f\text{CO}_2$  needed for oxidation to occur if the micrometeorite reacts with these amounts of air during entry. (b) Surface pressure versus  $f\text{CO}_2$  for a  $\text{N}_2$ - $\text{CO}_2$  atmosphere with 0.8 bar  $\text{N}_2$  (purple) and 0.4 bar  $\text{N}_2$  (green)  $\text{N}_2$ , as calculated from eq. 11 in the text.

CO<sub>2</sub> interacting with O<sub>2</sub> rather than N<sub>2</sub>). They suggested that N<sub>2</sub> would have been higher in Earth's early history and was slowly sequestered in the mantle due to biological drawdown, based on N<sub>2</sub>-Ar ratios. However, more recent authors have provided empirical support for lower atmospheric N<sub>2</sub> in the past. For example, analysis of vesicles in 2.7 Ga basaltic lavas erupted at sea-level imply  $P_s < 0.5$  bar (Marty et al., 2013), and measured N<sub>2</sub>/<sup>36</sup>Ar ratios in fluid inclusions trapped in 3 to 3.5 Ga hydrothermal quartz suggest  $P_s < 1.1$  bar, and possibly as low as 0.5 bar (Som et al., 2016; Avice et al., 2018). These studies argue that N<sub>2</sub> that was initially part of the mantle would have been exsolved and outgassed over time. All three of these estimates are consistent with the low  $pN_2$  and  $P_s$  values derived here.

#### **4.2. Constraints on $pCO_2$ from paleosols**

Archean CO<sub>2</sub> levels have also been estimated from paleosols. Driese et al. (2011) published an estimate of 10–50 PAL CO<sub>2</sub> at ~2.7 Ga, based on an analytical technique developed by Sheldon (2008). 1 PAL CO<sub>2</sub> corresponds to 370 ppmv, or  $3.7 \times 10^{-4}$  bar, in their model, so their estimate is approximately 0.004–0.02 bar. By comparison, our minimum estimates of  $pCO_2$  are ~0.16 bar for the 0.4-bar  $pN_2$  case and ~0.25 bar for the 0.8-bar  $pN_2$  case (these are true CO<sub>2</sub> partial pressures—hence, no prime on  $pCO_2$ —obtained by multiplying  $fCO_2 = 0.23$  by the corresponding surface pressure in Fig. S1b). Our  $pCO_2$  estimates are clearly much higher than Sheldon's estimates. But Sheldon's method of analysis can be criticized on several different grounds (Kasting, 2014). Most importantly, it implicitly assumes that every CO<sub>2</sub> molecule that enters the soil will react with a silicate mineral, which is probably not the case. Hence, his method should provide only a lower limit on atmospheric  $pCO_2$ . A more recent analysis of the same paleosols by

Kanzaki & Murakami (2015) yields  $p\text{CO}_2$  values ranging from 0.03 bar to almost 0.4 bar (Fig. 2.3). The upper end of these new estimates overlaps nicely with the  $\text{CO}_2$  partial pressures derived here. So,  $\sim 0.2$  bar might be considered a “best guess” of atmospheric  $p\text{CO}_2$  at the time when the Tomkins et al. micrometeorites fell to Earth. At the very least, the new  $p\text{CO}_2$  estimates from micrometeorite oxidation provide support for the higher Kanzaki & Murakami  $p\text{CO}_2$  estimates from paleosols as compared to the older estimates from Driese et al. and Sheldon.

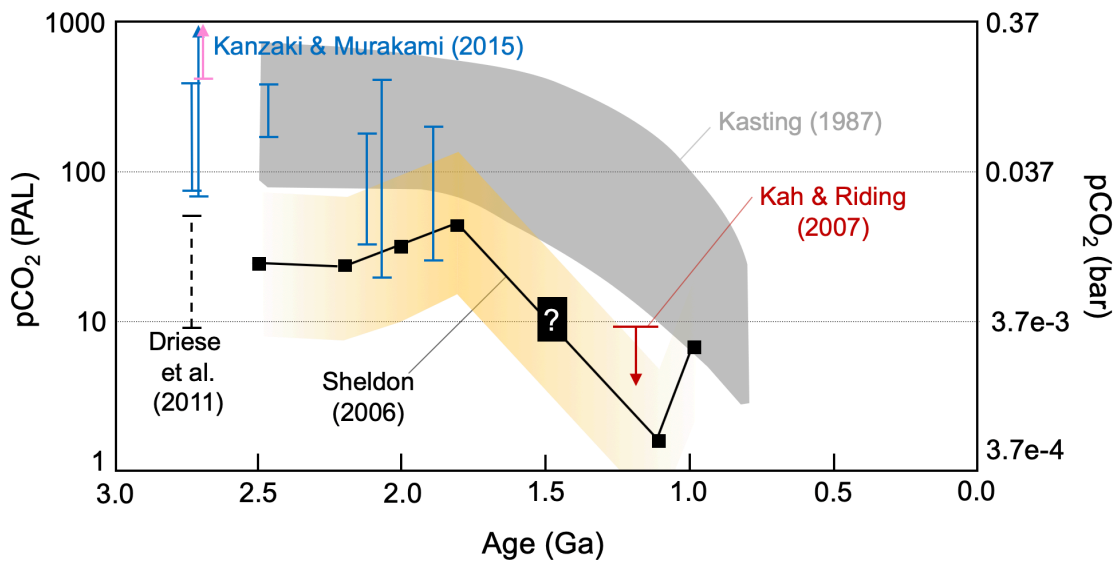


**Figure 2.3.**  $p\text{CO}_2$  estimates from paleosols compared to those from climate model calculations (grey shaded region) (Kharecha et al., 2005). Estimates from Sheldon (2008) are shown by the dark squares and solid black line (with error in yellow). The dashed vertical bar is the paleosol estimate at 2.7 Ga from Driese et al. (2011). The downward red arrow is the upper  $p\text{CO}_2$  limit from cyanobacterial sheath calcification at 1.2 Ga (Kah & Riding, 2007). The vertical bars in blue are the paleosol estimates from Kanzaki & Murakami (2015). The upward pink arrow indicates the  $p\text{CO}_2$  from our calculations at 2.7 Ga if  $p\text{N}_2$  was 0.8 bar. Modified from Catling & Kasting (2017, Fig. 11.7).

### **4.3. Other analyses of the Tomkins et al. micrometeorites**

It is worth comparing our analysis of the Tomkins et al. micrometeorites with two other recent analyses. We discuss their conclusions, and compare them with our own, here.

Rimmer et al. (2019) reanalyzed the Tomkins et al. micrometeorites, and concluded that they require low atmospheric surface pressure (on the order of  $\sim 0.3$  bar total) at 2.7 Ga to have been oxidized. According to their analysis, this allows H<sub>2</sub>O to penetrate into the upper atmosphere, where it then produces O<sub>2</sub> from photodissociation by UV. Zahnle & Buick (2016) had suggested this previously as a possible oxidation route, though they noted that it would require a much less effective tropopause cold trap than exists today. This solution would require that H<sub>2</sub>O was a major upper atmospheric constituent in the Rimmer et al. model; however, this does not seem to be the case, based on their Fig. 2, which depicts water vapor concentrations more or less the same as in the modern atmosphere and in our model. Instead, the O<sub>2</sub> in their model must be coming from the photolysis of CO<sub>2</sub>, as that is the only species that contains enough O atoms to produce it. CO<sub>2</sub> photolysis is slower in our model than in the Rimmer et al. model, for reasons that remain to be determined. Overall, their suggested source of O<sub>2</sub> from H<sub>2</sub>O, as well as their hypothetical atmosphere compositions for both of the cases they tested, are unlikely, if not unphysical. That said, while we think there may be problems with the Rimmer et al. model, or at least with their interpretations, we do agree that lower atmospheric pressure can help explain the Tomkins et al. data, as it would allow for a higher ratio of CO<sub>2</sub>:N<sub>2</sub>. This is a key factor in the analysis we present here.

Lehmer et al. (2020) also revisited the Tomkins et al. micrometeorites, using a model that incorporated entry physics. Their approach focused on modeling the motion, evaporation, and kinetic oxidation of a micrometeorite entering the atmosphere, simulating 15,000 entry scenarios by using a random sampling of parameter distributions for mass, velocity, and entry angle of incoming micrometeorites. In their model, the micrometeorites start as pure iron and are oxidized to wüstite or magnetite, as the Tomkins et al. micrometeorite seem to have been. All their simulations were for a 1-bar atmosphere with CO<sub>2</sub> concentrations between 2% and 85%. Lehmer et al. concluded, as we did, that CO<sub>2</sub> was a more likely oxidant than O<sub>2</sub> during the Archean if  $f\text{O}_2$  was 1% or lower, as was probably the case. While their range of possible  $f\text{CO}_2$  was considerably broader than our own—from 0.06 to at least 0.7, compared to our minimum estimate of 0.23 to 0.52—they agree that CO<sub>2</sub> would likely have needed to be a major constituent, in agreement with recent paleosol estimates (Kanzaki & Murakami, 2015). Lehmer et al. also suggested a lower overall surface pressure during the late Archean, to keep global mean surface temperatures consistent with glacial evidence from that time. Thus, their conclusions are basically similar to ours.

## **5. Conclusions**

To truly solve this problem, experimental data on iron oxidation by CO<sub>2</sub>, O, and O<sub>2</sub> in conditions like those a micrometeorite would experience during entry is needed. Nonetheless, existing data support the idea that the oxidation of Archean iron micrometeorites, melted during atmospheric entry, depends primarily on the amount of CO<sub>2</sub> available in the atmosphere. Assuming two-air-mass oxidation, and that CO<sub>2</sub> itself is the primary oxidant, we find that at least ~23% CO<sub>2</sub> would be needed to oxidize the

Tomkins et al. micrometeorites at 2.7 Ga. This CO<sub>2</sub> concentration can be reconciled with values derived from paleosols, provided that one accepts the higher estimates of Kanzaki and Murakami (2015). It is most easily reconciled with climate models if  $pN_2$  was lower than it is today, as this would facilitate a global mean surface temperature low enough for glaciation to occur. A surface pressure of about 0.6 bar, with less than 25% CO<sub>2</sub>, would have allowed the Tomkins et al. micrometeorites to be oxidized without conflicting with the evidence for glaciation at 2.7 Ga. There is thus no need to invoke unusually high atmospheric O<sub>2</sub> concentrations to explain the micrometeorite oxidation. Instead, these oxidized micrometeorites imply a Neoproterozoic atmosphere that was rich in CO<sub>2</sub> and somewhat poorer in N<sub>2</sub> than today's atmosphere.

## Appendix 1: Full Derivations and Model Specifics

### A1.1. Full derivation of CO<sub>2</sub> mass balance, Eq. (4)

Eq. (4) in Chapter 2 shows that, when CO<sub>2</sub> is included as an oxidant, the weighted sum of the mixing ratios of the different oxidants (O, O<sub>2</sub>, and CO<sub>2</sub>) is approximately equal to the mixing ratio of CO<sub>2</sub> at the surface,  $f\text{CO}_2^0$ . The derivation is as follows. Start from the continuity equation:

$$\frac{\partial n_i}{\partial t} = P_i - l_i n_i - \frac{\partial \Phi_i}{\partial z} \quad (\text{A1.1})$$

and the flux equation, neglecting molecular diffusion (as it is not relevant to this problem until one gets very near the homopause):

$$\Phi_i = -Kn \frac{\partial f_i}{\partial z} \quad (\text{A1.2})$$

Here,  $t$  = time,  $z$  = altitude,  $n_i$  = number density of species  $i$  (molecules/cm<sup>3</sup>),  $P_i$  = chemical production rate (molecules/cm<sup>3</sup>·s),  $l_i$  = chemical loss frequency (s<sup>-1</sup>),  $\Phi_i$  = flux of species  $i$ ,  $f_i \equiv n_i/n$  = mixing ratio of species  $i$ ,  $K$  = eddy diffusion coefficient (cm<sup>2</sup>/s), and  $n$  = total number density. All variables are given in CGS units, largely due to the fact that the kinetic theory of gases (e.g. Chapman et al., 1990; Chapman & Cowling, 1939) was originally developed using these units. A derivation of eq. (A1.2), including the molecular diffusion component, can be found in Ch. 15 of Banks & Kockarts (1973). Eq. (A1.2) applies to solving for a minor constituent diffusing through a more abundant background gas, which may introduce errors when applied to gases that become major constituents at some altitudes. That said, this issue has a limited effect on our analysis largely because the

altitudes at which our minor constituents become major constituents is limited to the top of the atmosphere, above the altitudes of interest for micrometeorite oxidation.

If steady state is assumed, then  $\frac{\partial n_i}{\partial t} = 0$ . If one divides by  $n$  to convert number densities into mixing ratios, eq. (A1.1) becomes

$$\frac{P_i}{n} - l_i f_i - \frac{1}{n} \frac{\partial \Phi_i}{\partial z} = 0 \quad (\text{A1.3})$$

Now let  $f_i = f_{\text{O}_{\text{tot}}} \equiv f_{\text{O}} + 2f_{\text{O}_2} + f_{\text{CO}} + 2f_{\text{CO}_2}$  (where we have neglected other minor O species, such as  $\text{H}_2\text{O}$ ). This variable represents the total oxygen mixing ratio. Continuing to refer to this mixing ratio as  $f_i$ , for simplicity, we can write

$$\frac{P_i}{n} - l_i f_i = 0 \quad (\text{A1.4})$$

Eq. (A1.4) must be true because O atoms are neither created nor lost above the altitude at which they are removed via rainout of  $\text{H}_2\text{O}$ . Inserting eq. (A1.4) into (A1.3) then yields

$$\frac{\partial \Phi_i}{\partial z} = 0 \rightarrow \Phi_i = \text{const.} \quad (\text{A1.5})$$

But  $\Phi_i$  must be zero at the top of the atmosphere, so we know from eq. (A1.2) that

$$\frac{\partial f_i}{\partial z} = 0 \rightarrow f_i = \text{const.} \quad (\text{A1.6})$$

and, therefore

$$f_{\text{O}_{\text{tot}}} = f_{\text{O}} + 2f_{\text{O}_2} + f_{\text{CO}} + 2f_{\text{CO}_2} = \text{const.} \approx 2f_{\text{CO}_2}^0 \quad (\text{A1.7})$$

where  $f\text{CO}_2^0$  is the  $\text{CO}_2$  mixing ratio at the Earth's surface. Eq. (A1.7) is valid if  $f\text{O}$ ,  $f\text{O}_2$ , and  $f\text{CO}$  are all  $\ll f\text{CO}_2$  at the surface; we see this is the case in our photochemical calculations (see Fig. A1.2, below).

Now, do the same calculation for carbon. If we define the total carbon mixing ratio as  $f\text{C}_{\text{tot}} \equiv f\text{CO} + f\text{CO}_2$ , then by the same logic as before we must have

$$f\text{C}_{\text{tot}} = f\text{CO} + f\text{CO}_2 \cong f\text{CO}_2^0 \quad (\text{A1.8})$$

Now subtract eq. (A1.8) from eq. (A1.7) to get

$$f(\text{O}) + 2f\text{O}_2 + f\text{CO}_2 = \text{const.} = f\text{CO}_2^0 \quad (\text{A1.9})$$

which is Eq. (4) in the main text of Chapter 2.

### A1.2: Derivation of Eq. 10

We use 'pseudo' partial pressure variables,  $p\text{CO}_2'$  and  $p\text{N}_2'$  in eq. (10) in Chapter 2. These variables are defined as the surface pressure that would be exerted by a certain amount of gas *if it was present by itself in the atmosphere*. This definition sometimes leads to confusion because it is seemingly contradictory to Dalton's Law, which says that the partial pressure of any ideal gas in a mixture of such gases is independent of the partial pressures of the other gases. Both  $\text{CO}_2$  and  $\text{N}_2$  are effectively ideal at terrestrial atmosphere pressures and temperatures, and yet Dalton's Law does not hold. The reason is that Dalton's Law is derived for gas mixtures that are contained within a fixed-volume container. The atmosphere is not fixed volume. Instead, the gases are confined by the planet's gravitational field. Lighter gases tend to diffuse away from the surface, while heavier gases diffuse towards it. The gases do work on each other as they interact through

diffusion. Adding a lighter gas, e.g. N<sub>2</sub>, to a heavier gas, e.g., CO<sub>2</sub>, reduces the partial pressure of CO<sub>2</sub> at the surface because the lighter N<sub>2</sub> drags some of the heavier CO<sub>2</sub> away from the planet's surface, thereby lowering its partial pressure.

In our analysis, though, we need to know the actual CO<sub>2</sub> partial pressure at the surface because that is what is measured, or at least attempted to be measured, from paleosols. And we need to be able to relate the CO<sub>2</sub> volume mixing ratio,  $f\text{CO}_2$ , to the pseudo partial pressure variable,  $p\text{CO}_2'$ , as we do in eq. (10). The derivation of eq. (10) follows.

The surface pressure of an isolated gas is linearly related to its column abundance. Thus, for a pure CO<sub>2</sub> atmosphere

$$p\text{CO}_2' = M_{\text{CO}_2} \cdot g \quad (\text{A1.10})$$

where,  $M_{\text{CO}_2}$  = the column mass of CO<sub>2</sub>, and  $g$  = gravity. The column number densities for CO<sub>2</sub> and N<sub>2</sub> can then be found from

$$\begin{aligned} N_{\text{col}}^{\text{CO}_2} &= \frac{M_{\text{col}}^{\text{CO}_2}}{44 \cdot m_{\text{H}}} = \frac{p\text{CO}_2'}{44 \cdot m_{\text{H}} \cdot g} \\ N_{\text{col}}^{\text{N}_2} &= \frac{M_{\text{col}}^{\text{N}_2}}{28 \cdot m_{\text{H}}} = \frac{p\text{N}_2'}{28 \cdot m_{\text{H}} \cdot g} \end{aligned} \quad (\text{A1.11})$$

where  $m_{\text{H}}$  = mass of a hydrogen atom. These column number densities are conserved when the two gases are mixed. The CO<sub>2</sub> volume mixing ratio,  $f\text{CO}_2$ , is thus

$$f\text{CO}_2 = \frac{N_{\text{col}}^{\text{CO}_2}}{N_{\text{col}}^{\text{CO}_2} + N_{\text{col}}^{\text{N}_2}} \quad (\text{A1.12})$$

Cancelling out the factors of  $(m_H \cdot g)$  in eq. (A1.11) yields

$$\begin{aligned} fCO_2 &= \frac{pCO'_2/44}{pCO'_2/44 + pN'_2/28} \\ &= \frac{1}{1 + \left(\frac{pN'_2}{pCO'_2}\right) \cdot \left(\frac{44}{28}\right)} \end{aligned} \tag{A1.13}$$

This equation, rearranged to solve for  $pCO'_2$ , is

$$pCO'_2 = pN'_2 \cdot \left(\frac{44}{28}\right) \cdot \left(\frac{fCO_2}{1 - fCO_2}\right) \tag{10}$$

which is our eq. (10) in the main text.

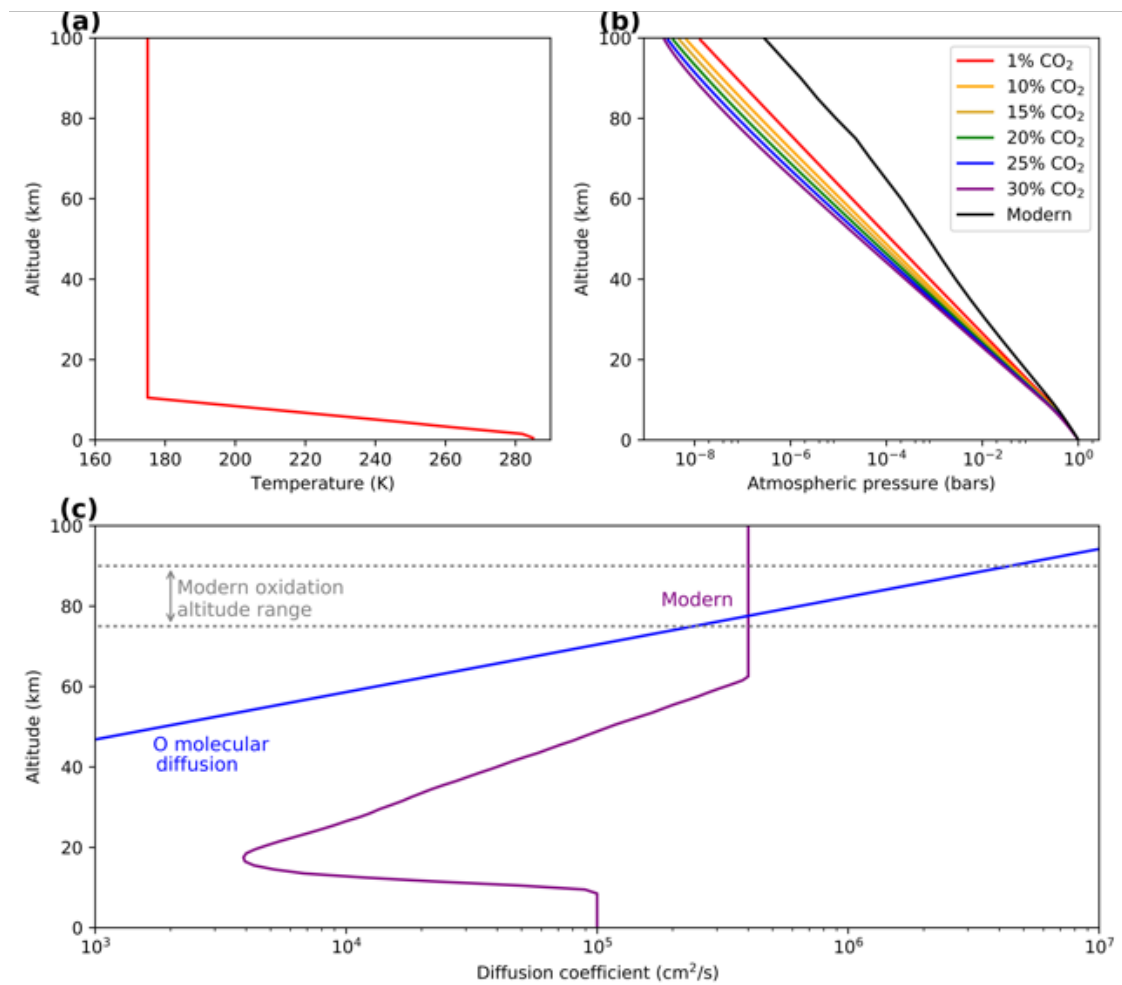


**Figure A1.1.** (a) Assumed vertical temperature profile for all simulations. (b) Vertical pressure profiles for various photochemical simulations, calculated using modern eddy diffusion coefficients. The pressure profile for the modern atmosphere is shown for comparison. (c) Vertical eddy diffusion profile used for all photochemical simulations (“modern”, purple). The solid blue curve is the molecular diffusion profile for atomic oxygen, which is calculated from Banks & Kockarts (1973) eqs. 15.28/29.

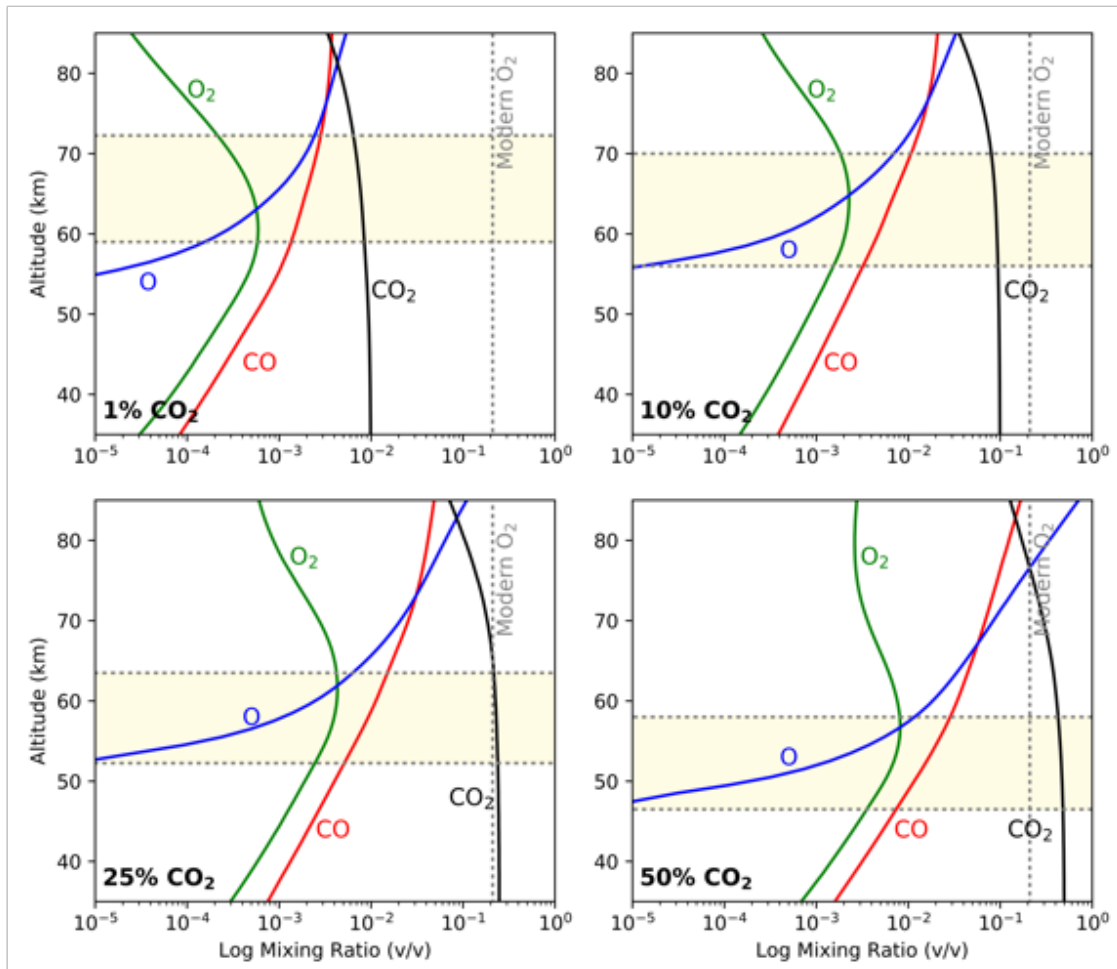


**Figure A1.2.** Upper atmospheric profiles of CO (red), O (blue), O<sub>2</sub> (green), and CO<sub>2</sub> (black) for various assumed surface concentrations of CO<sub>2</sub>. The shaded yellow region marks the micrometeorite oxidation pressure range for each  $f\text{CO}_2$ .

**Table A1.1:** Full list of reactions in the photochemical model used in Chapter 2 and Chapter 3.

Reaction	Rate constant (per second)	Reference	Notes
1) $\text{H}_2\text{O} + \text{O}(1\text{D}) \rightarrow 2\text{OH}$	$2.62\text{E}-10 * \text{EXP}(65./\text{T}(\text{I}))$	Dunlea et al. (2004)	°symbol means can be found in NIST database
2) $\text{H}_2 + \text{O}(1\text{D}) \rightarrow \text{OH} + \text{H}$	$1.10\text{E}-10$	DeMore et al. (1997)	
3) $\text{H}_2 + \text{O} \rightarrow \text{OH} + \text{H}$	$3.44\text{E}-13 * ((\text{T}(\text{I})/298.)^{**2.67}) * \text{EXP}(-3160./\text{T}(\text{I}))$	Baulch et al. (1992)	
4) $\text{H}_2 + \text{OH} \rightarrow \text{H}_2\text{O} + \text{H}$	$7.7\text{E}-12 * \text{EXP}(-2100./\text{T}(\text{I}))$	Atkinson et al. (2004)°	
5) $\text{H} + \text{O}_3 \rightarrow \text{OH} + \text{O}_2$	$1.4\text{E}-10 * \text{EXP}(-470./\text{T}(\text{I}))$	DeMore et al. (1992)	
6) $\text{H} + \text{O}_2 + \text{M} \rightarrow \text{HO}_2 + \text{M}$	TBDY(4.11E-32,7.51E-11,1.10,0.,TT, DN)	DeMore et al. (1997); Turanyi et al. (2012)	Explain notation: TBDY(K0, KI, N, M, T, DEN)
7) $\text{H} + \text{HO}_2 \rightarrow \text{H}_2 + \text{O}_2$	$5.6\text{E}-12$	Atkinson et al. (2004)°	
8) $\text{H} + \text{HO}_2 \rightarrow \text{H}_2\text{O} + \text{O}$	$2.4\text{E}-12$	Atkinson et al. (2004)°	
9) $\text{H} + \text{HO}_2 \rightarrow \text{OH} + \text{OH}$	$7.2\text{E}-11$	Atkinson et al. (2004)°	
10) $\text{OH} + \text{O} \rightarrow \text{H} + \text{O}_2$	$2.4\text{E}-11 * \text{EXP}(110./\text{T}(\text{I}))$	Atkinson et al. (2004)°	
11) $\text{OH} + \text{HO}_2 \rightarrow \text{H}_2\text{O} + \text{O}_2$	$5.00\text{E}-11$	Srinivasan et al. (2006)	
12) $\text{OH} + \text{O}_3 \rightarrow \text{HO}_2 + \text{O}_2$	$1.7\text{E}-12 * \text{EXP}(-940./\text{T}(\text{I}))$	Atkinson et al. (2004)°	
13) $\text{HO}_2 + \text{O} \rightarrow \text{OH} + \text{O}_2$	$2.7\text{E}-11 * \text{EXP}(225./\text{T}(\text{I}))$	Atkinson et al. (2004)°	
14) $\text{HO}_2 + \text{O}_3 \rightarrow \text{OH} + 2\text{O}_2$	$1.97\text{E}-16 * ((\text{T}(\text{I})/298.)^{**4.57}) * \text{EXP}(695./\text{T}(\text{I}))$	Atkinson et al. (2004)°	

**Table A1.1 (continued)**

<b>Reaction</b>	<b>Rate constant (per second)</b>	<b>Reference</b>	<b>Notes</b>
15) HO <sub>2</sub> + HO <sub>2</sub> → H <sub>2</sub> O <sub>2</sub> + O <sub>2</sub>	2.3E-13*EXP(600./T(I))+1.7E-33*EXP(1000./T(I))*DEN(I)	DeMore et al. (1992)	
16) H <sub>2</sub> O <sub>2</sub> + OH → HO <sub>2</sub> + H <sub>2</sub> O	2.9E-12*EXP(-160./T(I))	DeMore et al. (1992)	
17) O + O + M → O <sub>2</sub> + M	5.21E-35*EXP(900./T(I))*DEN(I)	Tsang and Hampson (1986) <sup>o</sup>	
18) O + O <sub>2</sub> + M → O <sub>3</sub> + M	TBDY(5.70E-34,1.E-10,2.6,0.,TT,DN)	DeMore et al. (1992); Atkinson et al. (2004) <sup>o</sup>	
19) O + O <sub>3</sub> → 2O <sub>2</sub>	8.0E-12*EXP(-2060./T(I))	DeMore et al. (1992)	
20) OH + OH → H <sub>2</sub> O + O	6.2E-14*((T(I)/298)**2.60)*EXP(945./T(I))	Atkinson et al. (2004) <sup>o</sup>	
21) O(1D) + N <sub>2</sub> → O(3P) + N <sub>2</sub>	1.8E-11*EXP(110./T(I))	DeMore et al. (1992)	
22) O(1D) + O <sub>2</sub> → O(3P) + O <sub>2</sub>	3.2E-11*EXP(70./T(I))	DeMore et al. (1992)	
23) O <sub>2</sub> + hν → O(3P) + O(1D)	5.81E-08	Thompson et al. (1963)	Photolysis rates used were taken from the top of the atmosphere (99.5 km altitude)
24) O <sub>2</sub> + hν → O(3P) + O(3P)	4.49E-08	Allen and Frederick (1982)	
25) H <sub>2</sub> O + hν → H + OH	5.48E-06	Thompson et al. (1963)	
26) O <sub>3</sub> + hν → O <sub>2</sub> + O(1D)	3.59E-03	WMO (1985)	
27) O <sub>3</sub> + hν → O <sub>2</sub> + O(3P)	6.97E-04	WMO (1985)	

**Table A1.1** (continued)

Reaction	Rate constant (per second)	Reference	Notes
28) $\text{H}_2\text{O}_2 + h\nu \rightarrow 2\text{OH}$	5.01E-05	DeMore et al. (1985)	
29) $\text{CO}_2 + h\nu \rightarrow \text{CO} + \text{O}(3\text{P})$	1.33E-09	Shemansky (1972)	
30) $\text{CO} + \text{OH} \rightarrow \text{CO}_2 + \text{H}$	$1.5\text{E}-13*(1.+0.6*\text{PATM})$	DeMore et al. (1992)	PATM = DEN(I)*1.38E-16*T(I)/1.013E6
31) $\text{CO} + \text{O} + \text{M} \rightarrow \text{CO}_2 + \text{M}$	$1.7\text{E}-33*\text{EXP}(-1510./\text{T(I)})*\text{DEN(I)}$	Tsang and Hampson (1986) <sup>o</sup>	
32) $\text{H} + \text{CO} + \text{M} \rightarrow \text{HCO} + \text{M}$	$5.29\text{E}-34*\text{EXP}(-370./\text{T(I)})*\text{DEN(I)}$	Baulch et al. (1994) <sup>o</sup>	
33) $\text{H} + \text{HCO} \rightarrow \text{H}_2 + \text{CO}$	1.50E-10	Baulch et al. (1992)	
34) $\text{HCO} + \text{HCO} \rightarrow \text{H}_2\text{CO} + \text{CO}$	0.	(Assumed)	
35) $\text{OH} + \text{HCO} \rightarrow \text{H}_2\text{O} + \text{CO}$	1.69E-10	Baulch et al. (1992)	
36) $\text{O} + \text{HCO} \rightarrow \text{H} + \text{CO}_2$	5.00E-11	Baulch et al. (1992)	
37) $\text{O} + \text{HCO} \rightarrow \text{OH} + \text{CO}$	5.00E-11	Baulch et al. (1992)	
38) $\text{H}_2\text{CO} + h\nu \rightarrow \text{H}_2 + \text{CO}$	4.16E-05	JPL (1983)	
39) $\text{H}_2\text{CO} + h\nu \rightarrow \text{HCO} + \text{H}$	4.11E-05	JPL (1983)	
40) $\text{HCO} + h\nu \rightarrow \text{H} + \text{CO}$	1.0E-2	Pinto et al. (1980)	
41) $\text{H}_2\text{CO} + \text{H} \rightarrow \text{H}_2 + \text{HCO}$	$2.14\text{E}-12*((\text{T(I)}/298)**1.62)*\text{EXP}(-1090./\text{T(I)})$	Baulch et al. (1994)	
42) $\text{CO}_2 + h\nu \rightarrow \text{CO} + \text{O}(1\text{D})$	1.36E-08	Thompson et al. (1963)	
43) $\text{H} + \text{H} + \text{M} \rightarrow \text{H}_2 + \text{M}$	$6.04\text{E}-33*((\text{T(I)}/298)**1.00)*\text{DEN(I)}$	Baulch et al. (1992) <sup>o</sup>	
44) $\text{HCO} + \text{O}_2 \rightarrow \text{HO}_2 + \text{CO}$	5.20E-12	Atkinson et al. (2001) <sup>o</sup>	

Table A1.1 (continued)

Reaction	Rate constant (per second)	Reference	Notes
45) $\text{H}_2\text{CO} + \text{OH} \rightarrow \text{H}_2\text{O} + \text{HCO}$	$8.20\text{E-}12 * \text{EXP}(40./\text{T(I)})$	Atkinson et al. (2001) <sup>o</sup>	
46) $\text{H} + \text{OH} + \text{M} \rightarrow \text{H}_2\text{O} + \text{M}$	$4.38\text{E-}30 * ((\text{T(I)}/298)**-2.00) * \text{DEN(I)}$	Baulch et al. (1992) <sup>o</sup>	
47) $\text{OH} + \text{OH} + \text{M} \rightarrow \text{H}_2\text{O}_2 + \text{M}$	TBDY(6.9E-31,2.50E-11,0.8,0.,TT,DN)	Atkinson et al. (2004) <sup>o</sup>	
48) $\text{H}_2\text{CO} + \text{O} \rightarrow \text{HCO} + \text{OH}$	$3.4\text{E-}11 * \text{EXP}(-1600./\text{T(I)})$	DeMore et al. (1992)	
49) $\text{H}_2\text{O}_2 + \text{O} \rightarrow \text{OH} + \text{HO}_2$	$1.4\text{E-}12 * \text{EXP}(-2000./\text{T(I)})$	DeMore et al. (1992)	
50) $\text{HO}_2 + \text{h}\nu \rightarrow \text{OH} + \text{O}$	3.04E-04	DeMore et al. (1985)	
51) $\text{CH}_4 + \text{h}\nu \rightarrow 1\text{CH}_2 + \text{H}_2$	4.41E-06	Mount et al. (1977)	
52) $\text{CH}_3\text{OOH} + \text{h}\nu \rightarrow \text{H}_3\text{CO} + \text{OH}$	4.07E-05	JPL (1983)	
53) $\text{N}_2\text{O} + \text{h}\nu \rightarrow \text{N}_2 + \text{O}$	5.34E-07	Johnson and Selwyn (1975)	
54) $\text{HNO}_2 + \text{h}\nu \rightarrow \text{NO} + \text{OH}$	1.7E-3	Cox (1974)	
55) $\text{HNO}_3 + \text{h}\nu \rightarrow \text{NO}_2 + \text{OH}$	8.59E-05	JPL (1983)	
56) $\text{NO} + \text{h}\nu \rightarrow \text{N} + \text{O}$	1.84E-06	Cieslik and Nicolet (1973)	
57) $\text{NO}_2 + \text{h}\nu \rightarrow \text{NO} + \text{O}$	5.78E-03	JPL (1983)	
58) $\text{CH}_4 + \text{OH} \rightarrow \text{CH}_3 + \text{H}_2\text{O}$	$4.16\text{E-}13 * ((\text{T(I)}/298.)**2.18) * \text{EXP}(-1230./\text{T(I)})$	Srinivasan et al. (2005)	
59) $\text{CH}_4 + \text{O(1D)} \rightarrow \text{CH}_3 + \text{OH}$	1.13E-10	DeMore et al. (1994)	
60) $\text{CH}_4 + \text{O(1D)} \rightarrow \text{H}_2\text{CO} + \text{H}_2$	7.51E-12	DeMore et al. (1994)	
61) $1\text{CH}_2 + \text{CH}_4 \rightarrow 2\text{CH}_3$	5.9E-11	Böhland et al. (1985b)	
62) $1\text{CH}_2 + \text{O}_2 \rightarrow \text{H}_2\text{CO} + \text{O}$	6.64E-14	Dombrowsky et al. (1992)	

**Table A1.1** (continued)

<b>Reaction</b>	<b>Rate constant (per second)</b>	<b>Reference</b>	<b>Notes</b>
<b>63)</b> $1\text{CH}_2 + \text{N}_2 \rightarrow 3\text{CH}_2 + \text{N}_2$	8.8E-12	Ashfold et al. (1981)	
<b>64)</b> $3\text{CH}_2 + \text{H}_2 \rightarrow \text{CH}_3 + \text{H}$	5.E-15	Tsang and Hampson (1986)	
<b>65)</b> $3\text{CH}_2 + \text{CH}_4 \rightarrow 2\text{CH}_3$	$7.1\text{E-}12 * \text{EXP}(-5051./\text{T(I)})$	Böhland et al. (1985a)	
<b>66)</b> $3\text{CH}_2 + \text{O}_2 \rightarrow \text{H}_2\text{CO} + \text{O}$	6.64E-14	Dombrowsky et al. (1992)	
<b>67)</b> $\text{CH}_3 + \text{O}_2 + \text{M} \rightarrow \text{CH}_3\text{O}_2 + \text{M}$	TBDY(4.49E-31,1.79E-12,3.00,1.70,TT,DN)	DeMore et al. (1997) <sup>o</sup>	
<b>68)</b> $\text{CH}_3 + \text{OH} \rightarrow \text{H}_2\text{CO} + \text{H}_2$	$2.59\text{E-}13 * ((\text{T(I)}/298)**-0.53) * \text{EXP}(-5440./\text{T(I)})$	Dean and Westmoreland (1987) <sup>o</sup>	
<b>69)</b> $\text{CH}_3 + \text{O} \rightarrow \text{H}_2\text{CO} + \text{H}$	1.1E-10	DeMore et al. (1992)	
<b>70)</b> $\text{CH}_3 + \text{O}_3 \rightarrow \text{H}_2\text{CO} + \text{HO}_2$	$5.4\text{E-}12 * \text{EXP}(-220./\text{T(I)})$	DeMore et al. (1992)	
<b>71)</b> $\text{CH}_3\text{O}_2 + \text{HO}_2 \rightarrow \text{CH}_3\text{OOH} + \text{O}_2$	$3.8\text{E-}13 * \text{EXP}(780./\text{T(I)})$	Atkinson et al. (2001) <sup>o</sup>	
<b>72)</b> $\text{CH}_3\text{O}_2 + \text{CH}_3\text{O}_2 \rightarrow 2\text{H}_3\text{CO} + \text{O}_2$	$7.40\text{E-}13 * \text{EXP}(-520./\text{T(I)})$	Atkinson et al. (2001) <sup>o</sup>	
<b>73)</b> $\text{CH}_3\text{O}_2 + \text{NO} \rightarrow \text{H}_3\text{CO} + \text{NO}_2$	$2.8\text{E-}12 * \text{EXP}(285./\text{T(I)})$	Atkinson et al. (2001) <sup>o</sup>	
<b>74)</b> $\text{H}_3\text{CO} + \text{O}_2 \rightarrow \text{H}_2\text{CO} + \text{HO}_2$	$3.9\text{E-}14 * \text{EXP}(-900./\text{T(I)})$	DeMore et al. (1997)	
<b>75)</b> $\text{H}_3\text{CO} + \text{O} \rightarrow \text{H}_2\text{CO} + \text{OH}$	1.E-14	NBS (1980)	
<b>76)</b> $\text{H}_3\text{CO} + \text{OH} \rightarrow \text{H}_2\text{CO} + \text{H}_2\text{O}$	3.2E-13	NBS (1980)	
<b>77)</b> $\text{N}_2\text{O} + \text{O(1D)} \rightarrow \text{NO} + \text{NO}$	6.7E-11	DeMore et al. (1997)	
<b>78)</b> $\text{N}_2\text{O} + \text{O(1D)} \rightarrow \text{N}_2 + \text{O}_2$	4.9E-11	DeMore et al. (1997)	
<b>79)</b> $\text{N} + \text{O}_2 \rightarrow \text{NO} + \text{O}$	$1.5\text{E-}11 * \text{EXP}(-3600./\text{T(I)})$	DeMore et al. (1992)	
<b>80)</b> $\text{N} + \text{O}_3 \rightarrow \text{NO} + \text{O}_2$	2.01E-16	DeMore et al. (1997)	(maximum value)

**Table A1.1 (continued)**

Reaction	Rate constant (per second)	Reference	Notes
81) $N + OH \rightarrow NO + H$	4.70E-11	Baulch et al. (1994)	
82) $N + NO \rightarrow N_2 + O$	2.09E-11*EXP(100./T(I))	DeMore et al. (1997)	
83) $NO + O_3 \rightarrow NO_2 + O_2$	1.4E-12*EXP(-1310./T(I))	Atkinson et al. (2004) <sup>o</sup>	
84) $NO + O + M \rightarrow NO_2 + M$	TBDY(9.E-32,3.E-11,1.5,0.,TT, DN)	DeMore et al. (1997) <sup>o</sup>	
85) $NO + HO_2 \rightarrow NO_2 + OH$	3.60E-12*EXP(270./T(I))	Atkinson et al. (2004) <sup>o</sup>	
86) $NO + OH + M \rightarrow HNO_2 + M$	TBDY(7.52E-31,3.3E-11,2.4,0.3,TT, DN)	Atkinson et al. (2004) <sup>oo</sup>	
87) $NO_2 + O \rightarrow NO + O_2$	5.50E-12*EXP(190./T(I))	Atkinson et al. (2004) <sup>o</sup>	
88) $NO_2 + OH + M \rightarrow HNO_3 + M$	TBDY(3.28E-30,2.7E-11,3.75,0.,TT, DN)	Troe (2012) <sup>o</sup>	
89) $NO_2 + H \rightarrow NO + OH$	1.47E-10	Su et al. (2002)	
90) $HNO_3 + OH \rightarrow H_2O + NO_3$	AK0+AK3M/(1.+AK3M/AK2)	DeMore et al. (1992)	Where: AK0 = 7.2E-15*EXP(785./T(I)), AK2 = 4.1E-16*EXP(1440./T(I)), AK3M = 1.9E-33*EXP(725./T(I))*DEN(I)
91) $HO_2 + NO_2 + M \rightarrow HO_2NO_2 + M$	TBDY(1.8E-31,4.7E-12,3.2,0,TT, DN)	Atkinson et al. (2004) <sup>o</sup>	
92) $HO_2NO_2 + OH \rightarrow NO_2 + H_2O + O_2$	1.90E-12*EXP(270./T(I))	Atkinson et al. (2004) <sup>o</sup>	
93) $HO_2NO_2 + O \rightarrow NO_2 + OH + O_2$	7.8E-11*EXP(-3400./T(I))	DeMore et al. (1997)	

**Table A1.1 (continued)**

<b>Reaction</b>	<b>Rate constant (per second)</b>	<b>Reference</b>	<b>Notes</b>
<b>94)</b> HO <sub>2</sub> NO <sub>2</sub> + M → HO <sub>2</sub> + NO <sub>2</sub> + M	(k <sub>91</sub> )/(2.33E-27*EXP(10870./T(I)))		Calculated from reverse reaction #91
<b>95)</b> HO <sub>2</sub> NO <sub>2</sub> + hν → HO <sub>2</sub> + NO <sub>2</sub>	2.44E-04	JPL (1983)	
<b>96)</b> CH <sub>3</sub> OOH + OH → CH <sub>3</sub> O <sub>2</sub> + H <sub>2</sub> O	1.9E-12*EXP(190./T(I))	Atkinson et al. (2001) <sup>o</sup>	
<b>97)</b> CH <sub>3</sub> O <sub>2</sub> + OH → H <sub>3</sub> CO + HO <sub>2</sub>	5E-11		Assumed = to Reaction #11
<b>98)</b> O <sub>3</sub> + NO <sub>2</sub> → O <sub>2</sub> + NO <sub>3</sub>	1.40E-13*EXP(-2470./T(I))	Atkinson et al. (2004) <sup>o</sup>	
<b>99)</b> NO <sub>2</sub> + NO <sub>3</sub> → NO + NO <sub>2</sub> + O <sub>2</sub>	4.5E-14*EXP(-1260./T(I))	DeMore et al. (1997)	
<b>100)</b> O + NO <sub>3</sub> → O <sub>2</sub> + NO <sub>2</sub>	1.00E-11	DeMore et al. (1997)	
<b>101)</b> CH <sub>3</sub> CL + hν → CH <sub>3</sub> + CL	1.27E-07	DeMore et al. (1985)	
<b>102)</b> NO + NO <sub>3</sub> → NO <sub>2</sub> + NO <sub>2</sub>	1.80E-11*EXP(110./T(I))	Atkinson et al. (2004) <sup>o</sup>	
<b>103)</b> OH + NO <sub>3</sub> → HO <sub>2</sub> + NO <sub>2</sub>	2.E-11	Atkinson et al. (2004) <sup>o</sup>	
<b>104)</b> CH <sub>3</sub> CL + OH → CL + H <sub>2</sub> O	2.4E-12*EXP(-1250./T(I))	Villenave et al. (1997), Herndon et al. (2001), Hsu and DeMore (1994)	
<b>105)</b> CL + O <sub>3</sub> → CLO + O <sub>2</sub>	2.80E-11*EXP(-250./T(I))	Atkinson et al. (2007) <sup>o</sup>	
<b>106)</b> CL + H <sub>2</sub> → HCL + H	3.90E-11*EXP(-2310./T(I))	Atkinson et al. (2007) <sup>o</sup>	
<b>107)</b> CL + CH <sub>4</sub> → HCL + CH <sub>3</sub>	8.24E-13*((T(I)/298)**2.49)*EXP(-610./T(I))	Bryukov et al. (2002)	

**Table A1.1** (continued)

<b>Reaction</b>	<b>Rate constant (per second)</b>	<b>Reference</b>	<b>Notes</b>
<b>108)</b> CL + CH <sub>3</sub> CL → CL + HCL	3.2E-11*EXP(-1250./T(I))	Manning and Kurylo (1997), Beichert et al. (1995), (Wallington et al. (1990)	
<b>109)</b> CL + H <sub>2</sub> CO → HCL + HCO	8.20E-11*EXP(-35./T(I))	Atkinson et al. (2001) <sup>o</sup>	
<b>110)</b> CL + H <sub>2</sub> O <sub>2</sub> → HCL + HO <sub>2</sub>	1.10E-11*EXP(-980./T(I))	Atkinson et al. (2007) <sup>o</sup>	
<b>111)</b> CL + HO <sub>2</sub> → HCL + O <sub>2</sub>	1.80E-11*EXP(170./T(I))	Atkinson et al. (2007) <sup>o</sup>	
<b>112)</b> CL + HO <sub>2</sub> → CLO + OH	6.30E-11*EXP(-570./T(I))	Atkinson et al. (2007) <sup>o</sup>	
<b>113)</b> CL + CLONO <sub>2</sub> → CL + CL + NO <sub>2</sub> (+O)	6.51E-12*EXP(135./T(I))	DeMore et al. (1997)	
<b>114)</b> CL + NO + M → NOCL + M	TBDY(9.E-32,1.E-10,1.6,0.,TT,DN)	DeMore et al. (1997) <sup>o</sup>	
<b>115)</b> CL + NO <sub>2</sub> + M → CLONO + M	TBDY(1.3E-30,1.E-10,2.,1.,TT,DN)	DeMore et al. (1997) <sup>o</sup>	
<b>116)</b> CL + NOCL → NO + CL <sub>2</sub>	5.8E-11*EXP(100./T(I))	DeMore et al. (1997)	
<b>117)</b> CL + O <sub>2</sub> + M → CLO <sub>2</sub> + M	TBDY(1.44E-33,1.E-10,3.9,0.,TT,DN)	DeMore et al. (1997); Atkinson et al. (2007) <sup>o</sup>	
<b>118)</b> CL + CLO <sub>2</sub> → CL <sub>2</sub> + O <sub>2</sub>	2.3E-10	DeMore et al. (1997)	
<b>119)</b> CL + CLO <sub>2</sub> → CLO + CLO	1.2E-11	DeMore et al. (1997)	
<b>120)</b> CLO + O → CL + O <sub>2</sub>	2.5E-11*EXP(110./T(I))	Atkinson et al. (2007) <sup>o</sup>	
<b>121)</b> CLO + NO → CL + NO <sub>2</sub>	6.2E-12*EXP(295./T(I))	Atkinson et al. (2007) <sup>o</sup>	
<b>122)</b> CLO + NO <sub>2</sub> + M → CLONO <sub>2</sub> + M	TBDY(1.64E-31,7.00E-11,3.4,0.,TT,DN)	Atkinson et al. (2007) <sup>o</sup>	
<b>123)</b> CLO + HO <sub>2</sub> → HOCL + O <sub>2</sub>	4.8E-13*EXP(700./T(I))	DeMore et al. (1997)	

**Table A1.1** (continued)

Reaction		Rate constant (per second)	Reference	Notes
124)	$\text{CLO} + \text{OH} \rightarrow \text{CL} + \text{HO}_2$	$1.1\text{E-}11 * \text{EXP}(120./\text{T(I)})$	DeMore et al. (1985)	
125)	$\text{HCL} + \text{OH} \rightarrow \text{CL} + \text{H}_2\text{O}$	$1.70\text{E-}12 * \text{EXP}(-230./\text{T(I)})$	Atkinson et al. (2007) <sup>o</sup>	
126)	$\text{HOCL} + \text{OH} \rightarrow \text{CLO} + \text{H}_2\text{O}$	$3.\text{E-}12 * \text{EXP}(-500./\text{T(I)})$	DeMore et al. (1997)	
127)	$\text{CLONO}_2 + \text{OH} \rightarrow \text{CL} + \text{HO}_2 + \text{NO}_2$	$1.2\text{E-}12 * \text{EXP}(-330./\text{T(I)})$	Atkinson et al. (2007) <sup>o</sup>	
128)	$\text{HCL} + \text{O} \rightarrow \text{CL} + \text{OH}$	$1.\text{E-}11 * \text{EXP}(-3300./\text{T(I)})$	DeMore et al. (1997)	
129)	$\text{HOCL} + \text{O} \rightarrow \text{CLO} + \text{OH}$	$1.70\text{E-}13$	Atkinson et al. (2007) <sup>o</sup>	
130)	$\text{CLONO}_2 + \text{O} \rightarrow \text{CL} + \text{O}_2 + \text{NO}_2$	$4.5\text{E-}12 * \text{EXP}(-900./\text{T(I)})$	Atkinson et al. (2007) <sup>o</sup>	
131)	$\text{CL}_2 + \text{OH} \rightarrow \text{HOCL} + \text{CL}$	$3.6\text{E-}12 * \text{EXP}(-1200./\text{T(I)})$	Atkinson et al. (2007) <sup>o</sup>	
132)	$\text{CL}_2 + \text{h}\nu \rightarrow \text{CL} + \text{CL}$	$1.82\text{E-}03$	DeMore et al. (1985)	
133)	$\text{CLO}_2 + \text{h}\nu \rightarrow \text{CLO} + \text{O}$	$2.71\text{E-}03$	DeMore et al. (1985)	
134)	$\text{HCL} + \text{h}\nu \rightarrow \text{H} + \text{CL}$	$8.01\text{E-}07$	DeMore et al. (1985)	
135)	$\text{HOCL} + \text{h}\nu \rightarrow \text{OH} + \text{CL}$	$2.84\text{E-}04$	DeMore et al. (1985)	
136)	$\text{NOCL} + \text{h}\nu \rightarrow \text{CL} + \text{NO}$	$2.55\text{E-}03$	DeMore et al. (1985)	
137)	$\text{CLONO} + \text{h}\nu \rightarrow \text{CL} + \text{NO}_2$	$4.80\text{E-}03$	DeMore et al. (1985)	
138)	$\text{CLONO}_2 + \text{h}\nu \rightarrow \text{CL} + \text{NO}_3$	$4.00\text{E-}04$	DeMore et al. (1985)	
139)	$\text{CLO}_2 + \text{h}\nu \rightarrow \text{CL} + \text{O}_2$	$(\#117)/(2.43\text{E-}25 * \text{EXP}(2979./\text{T(I)}))$	DeMore et al. (1997)	
140)	$\text{HO}_2 + \text{NO}_3 \rightarrow \text{HNO}_3 + \text{O}_2$	$1.91\text{E-}12$	Becker et al. (1992) <sup>o</sup>	
141)	$\text{CLO} + \text{CLO} + \text{M} \rightarrow \text{CL}_2\text{O}_2 + \text{M}$	TBDY(2.05E-32,1.00E-11,4.00,0.,TT,DN)	Atkinson et al. (2007) <sup>o</sup>	
142)	$\text{CL}_2\text{O}_2 + \text{h}\nu \rightarrow \text{CLO}_2 + \text{CL}$	$3.21\text{E-}03$	DeMore (1997)	

Table A1.1 (continued)

Reaction	Rate constant (per second)	Reference	Notes
143) $\text{Cl}_2\text{O}_2 + \text{M} \rightarrow \text{ClO} + \text{ClO}$	$(k_{141})/(3.E-27*\text{EXP}(8450./T(I)))$		Calculated from reverse reaction #141
144) $\text{ClO}_2 + \text{M} \rightarrow \text{Cl} + \text{O}_2$	$(k_{117},I)/(5.7E-25*\text{EXP}(2500./T(I)))$		Calculated from reverse reaction #117
145) $\text{Cl} + \text{NO}_3 \rightarrow \text{ClO} + \text{NO}_2$	2.40E-11	Atkinson et al. (2007) <sup>o</sup>	
146) $\text{Cl} + \text{HOCl} \rightarrow \text{Cl}_2 + \text{OH}$	$2.5E-12*\text{EXP}(-130./T(I))$	Cook et al. (1981) and Vogt and Schindler (1993)	
147) $\text{ClO} + \text{NO}_3 \rightarrow \text{ClONO} + \text{O}_2$	4.E-13	Atkinson et al. (1992) <sup>o</sup>	
148) $\text{ClONO} + \text{OH} \rightarrow \text{HOCl} + \text{NO}_2$	2.4E-12	Ganske et al. (1992) and Ganske et al. (1991)	*Originall y no EXP, but on site -> -1250; Previous value was 3.5E-14 which is far off
149) $\text{ClO}_2 + \text{O} \rightarrow \text{ClO} + \text{O}_2$	$2.4E-12*\text{EXP}(-960./T(I))$	Gleason et al. (1994)	
150) $\text{NO}_2 + \text{O} + \text{M} \rightarrow \text{NO}_3 + \text{M}$	TBDY(1.31E-31,2.3E-11,1.50,0.24,TT, DN)	Atkinson et al. (2004) <sup>o</sup>	
151) $\text{NO}_3 + h\nu \rightarrow \text{NO}_2 + \text{O}$	2.25E-02	JPL (1983)	
152) $\text{NO}_3 + \text{NO}_2 + \text{M} \rightarrow \text{N}_2\text{O}_5 + \text{M}$	TBDY3.70E-30,1.9E-12,4.10,0.20,TT, DN)	Atkinson et al. (2004) <sup>o</sup>	
153) $\text{N}_2\text{O}_5 + h\nu \rightarrow \text{NO}_2 + \text{NO}_3$	3.16E-04	JPL (1983)	
154) $\text{N}_2\text{O}_5 + \text{M} \rightarrow \text{NO}_2 + \text{NO}_3 + \text{M}$	TBDY(1.3E-19,5.7E-14,0.,0.,TT, DN)	NBS (1980)	

**Table A1.1** (continued)

Reaction		Rate constant (per second)	Reference	Notes
155)	$\text{N}_2\text{O}_5 + \text{H}_2\text{O} \rightarrow 2 \text{HNO}_3$	2.E-19	(Assumed)	Tuning parameter.
156)	$\text{SO} + \text{h}\nu \rightarrow \text{S} + \text{O}$	0.	(Assumed)	
157) *	$\text{SO}_2 + \text{h}\nu \rightarrow \text{SO} + \text{O}$	$0.7*(8.63\text{E-}05)$	Warneck et al. (1964), Okabe (1971)	
158)	$\text{H}_2\text{S} + \text{h}\nu \rightarrow \text{HS} + \text{H}$	1.38E-04	Sullivan and Holland (1966)	
159)	$\text{SO} + \text{O}_2 \rightarrow \text{O} + \text{SO}_2$	$1.60\text{E-}13*\text{EXP}(-2280./\text{T(I)})$	Atkinson et al. (2004) <sup>o</sup>	
160)	$\text{SO} + \text{HO}_2 \rightarrow \text{SO}_2 + \text{OH}$	2.8E-11	DeMore et al. (1992)	
161)	$\text{SO} + \text{O} \rightarrow \text{SO}_2$	$6.0\text{E-}31*\text{DEN(I)}$	Kasting (1990)	
162)	$\text{SO} + \text{OH} \rightarrow \text{SO}_2 + \text{H}$	8.6E-11	DeMore et al. (1992)	
163)	$\text{SO}_2 + \text{OH} \rightarrow \text{HSO}_3$	TBDY(4.62E-31,1.31E-12,3.90,0.70,TT,DN)	Atkinson et al. (2004) <sup>o</sup>	
164)	$\text{SO}_2 + \text{O} \rightarrow \text{SO}_3$	$3.4\text{E-}32*\text{EXP}(-1130./\text{T(I)})*\text{DEN(I)}$	Turco et al. (1982)	
165)	$\text{SO}_3 + \text{H}_2\text{O} \rightarrow \text{H}_2\text{SO}_4$	6.00E-15	DeMore et al. (1992)	
166)	$\text{HSO}_3 + \text{O}_2 \rightarrow \text{HO}_2 + \text{SO}_3$	$1.30\text{E-}12*\text{EXP}(-330./\text{T(I)})$	Atkinson et al. (2004) <sup>o</sup>	
167)	$\text{HSO}_3 + \text{OH} \rightarrow \text{H}_2\text{O} + \text{SO}_3$	1.00E-11	Kasting (1990)	
168)	$\text{HSO}_3 + \text{H} \rightarrow \text{H}_2 + \text{SO}_3$	1.00E-11	Kasting (1990)	
169)	$\text{HSO}_3 + \text{O} \rightarrow \text{OH} + \text{SO}_3$	1.00E-11	Kasting (1990)	
170)	$\text{H}_2\text{S} + \text{OH} \rightarrow \text{H}_2\text{O} + \text{HS}$	$6.10\text{E-}12*\text{EXP}(-80./\text{T(I)})$	Atkinson et al. (2004) <sup>o</sup>	
171)	$\text{H}_2\text{S} + \text{H} \rightarrow \text{H}_2 + \text{HS}$	$3.66\text{E-}12*((\text{T(I)}/298)**1.94)*\text{EXP}(-455./\text{T(I)})$	Pen et al. (1999)	
172)	$\text{H}_2\text{S} + \text{O} \rightarrow \text{OH} + \text{HS}$	$9.22\text{E-}12*\text{EXP}(-1800./\text{T(I)})$	DeMore et al. (1997)	
173)	$\text{HS} + \text{O} \rightarrow \text{H} + \text{SO}$	1.60E-10	DeMore et al. (1992)	

Table A1.1 (continued)

Reaction	Rate constant (per second)	Reference	Notes	
174) HS + O <sub>2</sub> → OH + SO	4.00E-19	DeMore et al. (1992)		
175) HS + HO <sub>2</sub> → H <sub>2</sub> S + O <sub>2</sub>	3.00E-11	McElroy et al. (1980)		
176) HS + HS → H <sub>2</sub> S + S	1.20E-11	Baulch et al. (1976)		
177) HS + HCO → H <sub>2</sub> S + CO	5.00E-11	Kasting (1990)		
178) HS + H → H <sub>2</sub> + S	1.00E-11	Langford and Oldershaw (1972)		
179) HS + S → H + S <sub>2</sub>	2.2E-11*EXP(120./T(I))	DeMore et al. (1992), Kasting (1990)		
180) S + O <sub>2</sub> → SO + O	2.10E-12	Atkinson et al. (2004) <sup>o</sup>		
181) S + OH → SO + H	6.60E-11	DeMore et al. (1992)		
182) S + HCO → HS + CO	0.	(This reaction has been removed)		
182a) )*	SO <sub>2</sub> + hv → S + O <sub>2</sub>	0.3*(8.63E-05)	Warneck et al. (1964), Okabe (1971)	*note about assumed branching ratio
183)	S + HO <sub>2</sub> → HS + O <sub>2</sub>	1.5E-11	Kasting (1990)	
184)	S + HO <sub>2</sub> → SO + OH	1.5E-11	Kasting (1990)	
185)	HS + H <sub>2</sub> CO → H <sub>2</sub> S + HCO	1.7E-11*EXP(-800./T(I))	DeMore et al. (1992)	
186)	SO <sub>2</sub> + hv → SO <sub>2</sub> 1	9.66E-04	Warneck et al. (1964), Okabe (1971)	

**Table A1.1** (continued)

<b>Reaction</b>	<b>Rate constant (per second)</b>	<b>Reference</b>	<b>Notes</b>
<b>187)</b> SO <sub>2</sub> + hv → SO <sub>2</sub> <sup>+</sup>	8.84E-07	Warneck et al. (1964), Okabe (1971)	
<b>188)</b> H <sub>2</sub> SO <sub>4</sub> + hv → SO <sub>2</sub> + OH + OH	8.05E-07	Turco et al. (1979)	
<b>189)</b> SO <sub>3</sub> + hv → SO <sub>2</sub> + O	0.	(Assumed)	
<b>190)</b> SO <sub>2</sub> <sup>+</sup> + M → SO <sub>2</sub> + M	1.0E-12	Turco et al. (1982)	
<b>191)</b> SO <sub>2</sub> <sup>+</sup> + M → SO <sub>2</sub> + M	1.0E-11	Turco et al. (1982)	
<b>192)</b> SO <sub>2</sub> <sup>+</sup> + hv → SO <sub>2</sub> <sup>+</sup> + hv	1.5E+3	Turco et al. (1982)	
<b>193)</b> SO <sub>2</sub> <sup>+</sup> + hv → SO <sub>2</sub> + hv	2.2E+4	Turco et al. (1982)	
<b>194)</b> SO <sub>2</sub> <sup>+</sup> + O <sub>2</sub> → SO <sub>3</sub> + O	1.0E-16	Turco et al. (1982)	
<b>195)</b> SO <sub>2</sub> <sup>+</sup> + SO <sub>2</sub> → SO <sub>3</sub> + SO	4.0E-12	Turco et al. (1982)	
<b>196)</b> SO <sub>3</sub> + M → SO <sub>2</sub> + M	1.5E-13	Turco et al. (1982)	
<b>197)</b> SO <sub>3</sub> + hv → SO <sub>2</sub> + hv	1.13E+3	Turco et al. (1982)	
<b>198)</b> SO <sub>3</sub> + SO <sub>2</sub> → SO <sub>3</sub> + SO	7.0E-14	Turco et al. (1982)	
<b>199)</b> SO + NO <sub>2</sub> → SO <sub>2</sub> + NO	1.40E-11	Atkinson et al. (2004) <sup>o</sup>	
<b>200)</b> SO + O <sub>3</sub> → SO <sub>2</sub> + O <sub>2</sub>	4.50E-12*EXP(-1170./T(I))	Atkinson et al. (2004) <sup>o</sup>	
<b>201)</b> SO <sub>2</sub> + HO <sub>2</sub> → SO <sub>3</sub> + OH	0.	(Assumed)	
<b>202)</b> HS + O <sub>3</sub> → HSO + O <sub>2</sub>	9.50E-12*EXP(-280./T(I))	Atkinson et al. (2004) <sup>o</sup>	
<b>203)</b> HS + NO <sub>2</sub> → HSO + NO	2.90E-11*EXP(240./T(I))	Atkinson et al. (2004) <sup>o</sup>	
<b>204)</b> S + O <sub>3</sub> → SO + O <sub>2</sub>	1.20E-11	DeMore et al. (1990)	
<b>205)</b> SO + SO → SO <sub>2</sub> + S	8.30E-15	Herron and Huie (1980)	

**Table A1.1 (continued)**

<b>Reaction</b>	<b>Rate constant (per second)</b>	<b>Reference</b>	<b>Notes</b>
<b>206)</b> SO <sub>3</sub> + SO → SO <sub>2</sub> + SO <sub>2</sub>	2.00E-15	Chung et al. (1975)	
<b>207)</b> S + CO <sub>2</sub> → SO + CO	1.00E-20	Yung and DeMore (1982)	
<b>208)</b> SO + HO <sub>2</sub> → HSO + O <sub>2</sub>	0.	(Assumed)	
<b>209)</b> SO + HCO → HSO + CO	(k44)	Kasting (1990)	
<b>210)</b> H + SO → HSO	(k6)	Kasting (1990)	
<b>211)</b> HSO + hν → HS + O	3.04E-04	DeMore et al. (1985)	
<b>212)</b> HSO + OH → H <sub>2</sub> O + SO	(k11)	Kasting (1990)	
<b>213)</b> HSO + H → HS + OH	(k9)	Kasting (1990)	
<b>214)</b> HSO + H → H <sub>2</sub> + SO	(k7)	Kasting (1990)	
<b>215)</b> HSO + HS → H <sub>2</sub> S + SO	1.00E-12	Kasting (1990)	
<b>216)</b> HSO + O → OH + SO	(k13)	Kasting (1990)	
<b>217)</b> HSO + S → HS + SO	1.00E-11	Kasting (1990)	
<b>218)</b> N <sub>2</sub> + O <sub>1</sub> D → N <sub>2</sub> O	TBDY(3.5E-37,1.E-10,0.6,0.,TT,DN)	DeMore et al. (1997)	
<b>219)</b> N <sub>2</sub> O + H → NO + NO + OH	5.03e-7*(298./T(I))**2.16*exp(-18701./T(I))	Bozelli et al. (1994) <sup>o</sup>	
<b>220)</b> N <sub>2</sub> O + NO → NO <sub>2</sub> + N <sub>2</sub>	2.E-14*EXP(-25000./T(I))	NBS (1980)	

## Chapter 3.

# The response of the greenhouse effect, and surface temperature, to changes in atmospheric O<sub>2</sub> during the Phanerozoic

Chapter 3 is published in the *Journal of Geophysical Research: Atmospheres (JGR: Atmospheres)* in August 2016 (<https://doi.org/10.1002/2016JD025459>), with coauthors Amber Young (née Britt), Howard Chen, David Catling, and James Kasting. I conducted the modeling and wrote the analysis; Britt and Chen contributed to some of the early modeling; Kasting assisted with model development. I thank all coauthors for their input on the text.

### 1. Background

While the Archean greenhouse effect prior to the rise of atmospheric oxygen depended largely on CO<sub>2</sub>, with additional warming from gases like CH<sub>4</sub>, the Phanerozoic atmosphere has been markedly different. The last 541 million years of climate history have been intertwined with the installation of O<sub>2</sub> as a major atmospheric constituent, shifting the fraction of the atmosphere made up of greenhouse gases. This chapter (as well as Chapter 4) focuses on greenhouse effect dynamics in the now-oxygenated atmosphere.

The longstanding paradigm of Phanerozoic climate change is that elevated CO<sub>2</sub> at the beginning of the Phanerozoic and intermittently throughout, along with steadily increasing solar luminosity, were the dominant controls on global temperature. The Cenomanian age at ~100 to 94 Ma—the earliest age of the Cretaceous period—was marked by warm global temperatures. By this time, the Sun was approximately 99% as bright as it is today, meaning that incoming solar radiation was great enough that the Earth could maintain a habitable global mean surface temperature with much less atmospheric CO<sub>2</sub> than was needed earlier in Earth's history. The breakup of the supercontinent Pangea resulted in elevated sea levels as mid-ocean ridge area increased, along with increased atmospheric CO<sub>2</sub> due to volcanic outgassing from spreading centers. CO<sub>2</sub> rose to above

1000 ppm during this thermal maximum (Berner, 2006; Rothman, 2002). The combination of near-modern-day solar luminosity and high CO<sub>2</sub>, driven in part by continental geography, resulted in a warm global climate during the Cenomanian.

Poulsen et al. (2015) argued that changing atmospheric O<sub>2</sub> concentrations may also have been an important driver of climate during the Phanerozoic, along with changing atmospheric CO<sub>2</sub>. Specifically, they used the GENESIS 3-D climate model to simulate a baseline mid-Cretaceous climate with 21% O<sub>2</sub>, along with 1120 ppmv CO<sub>2</sub>, and a solar constant of 0.9943 times the present value. They then looked at the effect of varying the atmospheric O<sub>2</sub> mixing ratio from 10% to 35%, which correspond to the lower and upper bounds derived from a charcoal O<sub>2</sub> proxy (Scott & Glasspool, 2006). They found that the global mean temperature increased by 2.1 K for the low-O<sub>2</sub> calculation and decreased by 2.3 K for the high-O<sub>2</sub> calculation. The suggested mechanism was decreased Rayleigh scattering at low O<sub>2</sub> levels (as fewer O<sub>2</sub> molecules in the atmosphere would mean less scattering), leading to a decrease in reflected solar radiation and a corresponding rise in surface temperature. At higher O<sub>2</sub> levels, increased Rayleigh scattering lowered the surface temperature in their model. Cloud feedbacks were also argued to be important in determining the climate response to O<sub>2</sub> forcing.

To test whether the Poulsen et al. results are robust, we used a version of our own 1-D climate model (Segura et al., 2003a) to perform a similar calculation. The 2003 model version was used with the RRTM (Rapid Radiative Transfer Model) of Mlawer et al. (1997) for infrared radiation because this model has been well-validated for present Earth conditions. Instead of simulating the mid-Cretaceous, as Poulsen et al. did, we computed the effects of changing O<sub>2</sub> in the modern atmosphere. In our model, these effects are nearly identical to

those obtained for mid-Cretaceous conditions. We also used a 1-D photochemical model to compute self-consistent ozone changes for these changes in  $O_2$ , as well as related trace gases such as  $CH_4$  and  $N_2O$ , and we calculated the accompanying changes in surface temperature caused by the ozone changes.

## **2. Conservation of nitrogen**

Before describing our calculations, we first point out that one must be careful when adding or subtracting partial pressures and thus changing overall surface pressure. In Chapter 2, we considered a similar issue when changing  $pN_2$  in the Archean atmosphere to influence total surface pressure. As noted in Section 4.1 of Chapter 2 (and again below), lighter gases cause heavier ones to diffuse away from Earth's surface, but heavier gases cause lighter ones to diffuse towards it. Therefore, one has to be careful when adding or subtracting  $O_2$  from a model atmosphere, because the partial pressure of a gas is not linearly related to its column abundance when the surface pressure changes.

Poulsen et al. (2015) calculated the change in atmospheric pressure caused by adding or removing  $O_2$  by simply adding or subtracting partial pressures. It can be shown that this methodology does not conserve the column mass of other atmospheric constituents, in this case  $N_2$  and Ar. The reason is that, in seeming contradiction with Dalton's Law, the partial pressure of one atmospheric gas depends on the partial pressures of the other gases in a column of air under the influence of gravity. Adding a lighter gas to a heavier one increases the atmospheric scale height and causes the heavier gas to spread vertically, decreasing its partial pressure at the surface. The errors introduced by incorrectly changing the atmospheric pressure are modest (about 2%) when expressed in terms of total atmospheric pressure. However, if one calculates the error relative to the change in

atmospheric pressure expected at 10% O<sub>2</sub> or 35% O<sub>2</sub>, the error is much higher, at roughly 10%.

Below, we outline a method for changing the O<sub>2</sub> volume mixing ratio while conserving the column masses of N<sub>2</sub> and Ar. For simplicity, we adopt modern volume mixing ratios of the modern Earth scenario, with values,  $C_i$ , of 0.21 for O<sub>2</sub>, 0.78 for N<sub>2</sub>, and 0.01 for Ar. To begin, we conserve the current ratio of N<sub>2</sub> to Ar,  $R_{N_2Ar} = 1/78$ . We also need to initialize the atmospheric column mass, which is given by

$$M_{col}^a = \frac{P_S}{g} \quad (1)$$

Here,  $P_S$  is surface pressure and  $g$  is gravitational acceleration. We next compute the mean molecular mass as

$$m = (C_{O_2} \cdot 32 + C_{N_2} \cdot 28 + C_{Ar} \cdot 40) \cdot m_H \quad (2)$$

where  $m_H$  is the mass of a hydrogen atom. The column mass of each individual species,  $i$ , is then computed from

$$M_{col}^i = C_i M_{col}^a \left( \frac{m_i}{m} \right) \quad (3)$$

where  $m_i$  is the species molecular mass. We then get the column number density of each gas by dividing its column mass density by its molecular mass

$$N_{col}^i = \frac{M_{col}^i}{m_i} \quad (4)$$

When we change the O<sub>2</sub> mixing ratio, we must recalculate the mixing ratio of N<sub>2</sub> and Ar.

These mixing ratios must sum to unity, such that

$$C_{O_2'} + C_{N_2'} + C_{Ar'} = C_{O_2'} + C_{N_2'}(1 + R_{N_2Ar}) = 1 \quad (5)$$

So,

$$C_{N_2'} = \frac{1 - C_{O_2'}}{1 + R_{N_2Ar}} \quad (6)$$

$$C_{Ar'} = C_{N_2'} R_{N_2Ar} \quad (7)$$

We use these new mixing ratios to compute a new mean molecular mass from equation (2).

The rest of the procedure requires iterations, as the total column changes. First, we calculate a new column number density of O<sub>2</sub> from  $N_{col}^{O_2} = C_{O_2} N_{col}^a$ , where  $N_{col}^a$  is the total column number density. Then, add this to  $N_{col}^{N_2} + N_{col}^{Ar}$  to get a new value for  $N_{col}^a$ '. Now, recalculate  $N_{col}^{O_2}$  using the new value of  $N_{col}^a$ '.  $N_{col}^a$  changes in each iteration. Using the new  $N_{col}^{O_2}$ , we can convert it back to column mass using  $M_{col}^{O_2} = \frac{N_{col}^{O_2}}{32 m_H}$ . Add this value to the column masses of N<sub>2</sub> and Ar (which were held constant) to compute a new total column mass,  $M_{col}^a$ '. Finally, from this, we find the new surface pressure  $P_S$  using eq. (1).

To ascertain that we have indeed conserved nitrogen with an altered  $C_{O_2}$  value, we check the final column mass of nitrogen after the final iteration using eq. (3), which is equal to the initial  $M_{col}^{N_2}$  at 7787.43 kg/m<sup>2</sup>. These numerical results are summarized in Table 3.2.

Overall, we find a mean 1.6 % discrepancy between our calculated surface pressure values and those of Poulsen et al. (2015).

Finally, following the methodology of Poulsen et al., we conserve column masses of CH<sub>4</sub> and N<sub>2</sub>O by increasing their surface mixing ratios for low O<sub>2</sub> and decreasing them at higher O<sub>2</sub> (see Table 3.1). Their mixing ratios are inversely proportional to surface pressure. This does not account for changes in their atmospheric photochemistry as O<sub>2</sub> changes, so we also performed a sensitivity study to determine how important these assumptions about CH<sub>4</sub> and N<sub>2</sub>O might be. An alternative methodology that of Poulsen et al. is to hold the upward fluxes of these gases constant and allow their surface mixing ratios to change freely in response to increasing or decreasing O<sub>2</sub>. When this approach is taken, CH<sub>4</sub> continues to vary inversely with surface pressure, but the N<sub>2</sub>O mixing ratio actually increases as O<sub>2</sub> increases, and decreases when O<sub>2</sub> decreases (Table 3.1, last two columns), contrary to what Poulsen et al. assumed. The reason for this is that higher atmospheric O<sub>2</sub> shields N<sub>2</sub>O from photolysis and thus lengthens its atmospheric lifetime. But this has a negligible effect on surface temperature; as O<sub>2</sub> is increased from 21% to 35%, surface

---



---

**Table 3.1:** Effect of changing O<sub>2</sub> on surface volume mixing ratios of CH<sub>4</sub> and N<sub>2</sub>O with constant column mass or fixed upward flux

Species	Volume mixing ratio				
	21% O <sub>2</sub>	Constant column mass		Fixed upward flux	
		10% O <sub>2</sub>	35% O <sub>2</sub>	10% O <sub>2</sub>	35% O <sub>2</sub>
CH <sub>4</sub>	1.60×10 <sup>-6</sup>	1.85×10 <sup>-6</sup>	1.29×10 <sup>-6</sup>	1.91×10 <sup>-6</sup>	1.43×10 <sup>-6</sup>
N <sub>2</sub> O	3.00×10 <sup>-7</sup>	3.47×10 <sup>-7</sup>	2.42×10 <sup>-7</sup>	2.31×10 <sup>-7</sup>	3.42×10 <sup>-7</sup>

---



---

temperature rises from 289.54 K to 290.86 K with constant upward flux, as opposed to 290.95 K with constant mixing ratios, so the effect of properly scaling N<sub>2</sub>O is only on the order of approximately 0.1 K).

### 3. Radiative forcing calculations

Using this methodology, we computed surface pressures for two different O<sub>2</sub> volume mixing ratios, 0.1 and 0.35. We then did three sets of calculations using the Segura et al. (2003) radiative-convective climate model. First, we did a control simulation with  $C_{O_2} = 0.21$  and  $P_S = 101.3$  kPa. Results are shown in the second row of Table 3.2.  $\bar{M}$  is the mean molecular weight;  $T_S$  (equal to 288.3 K) is the calculated mean surface temperature,  $A_P$  is the planetary or top-of-atmosphere (TOA) albedo,  $F_{IR}^{up}$  is the outgoing TOA infrared flux,  $F_{SOL}^{up}$  is the reflected TOA solar flux, and  $F_{SOL}^{dn}$  is the downward solar flux at the surface. Because these are converged simulations, the net TOA flux (net IR minus net solar) is close to zero.

Next, we did two “one-step” calculations with  $C_{O_2}$  changed to 0.1 and 0.35. The advantage of these types of model calculations is that they provide quick indicators of how upward and downward energy fluxes in the atmosphere are balanced, which more complex model calculations (such as the simulations we conduct in Section 4 of this chapter) can quantify in terms of the effect on surface temperature. The goal of our one-step calculations was to calculate the instantaneous radiative forcing caused by the O<sub>2</sub> change (although doing so requires making several assumptions, as described below). These simulations should indicate the direction and size of the change in greenhouse effect compared to Rayleigh scattering.

In these calculations, the vertical temperature profile was kept the same as in the control run, and the model was either stretched or compressed so as to reach the surface. Each model atmosphere has 100 vertical layers, which are unevenly spaced in log pressure. The lowest level is at the surface, so as the surface pressure changes, the pressure at each level also changes. To maintain a self-consistent atmospheric profile, with a convective troposphere, we first reduced the temperatures below the atmospheric cold trap to the cold trap value. However, the surface temperature,  $T_S$  was kept at the control value of 288.3 K. We then drew moist adiabats up from the surface until they intersected with the temperature profile. Finally, we recomputed the water vapor mixing ratio at each pressure level from its saturation vapor pressure and the specified distribution of relative humidity (following Manabe & Wetherald, 1967), and then computed radiative fluxes.

Results are shown in Table 3.2 and Fig. 3.1. The outgoing solar radiation decreases by about  $0.05 \text{ W/m}^2$  in the low- $\text{O}_2$  case and increases by just over  $0.4 \text{ W/m}^2$  in the high- $\text{O}_2$  case. These changes are caused by changes in Rayleigh scattering, which decreases with low  $\text{O}_2$  and increases with high  $\text{O}_2$  as discussed by Poulsen et al. But the outgoing infrared flux changes by a considerably greater amount: it is  $3.87 \text{ W/m}^2$  higher in the low- $\text{O}_2$  case and  $5.91 \text{ W/m}^2$  lower in the high- $\text{O}_2$  case relative to the control case. These changes in the outgoing IR flux are the result of increased and decreased pressure broadening of absorption lines of  $\text{CO}_2$  and  $\text{H}_2\text{O}$  at high and low  $\text{O}_2$  levels, respectively. Pressure broadening is a mechanism by which the effectiveness of a greenhouse gas can be increased due to atmospheric pressure. Briefly, collisions between greenhouse gases like  $\text{CO}_2$  and

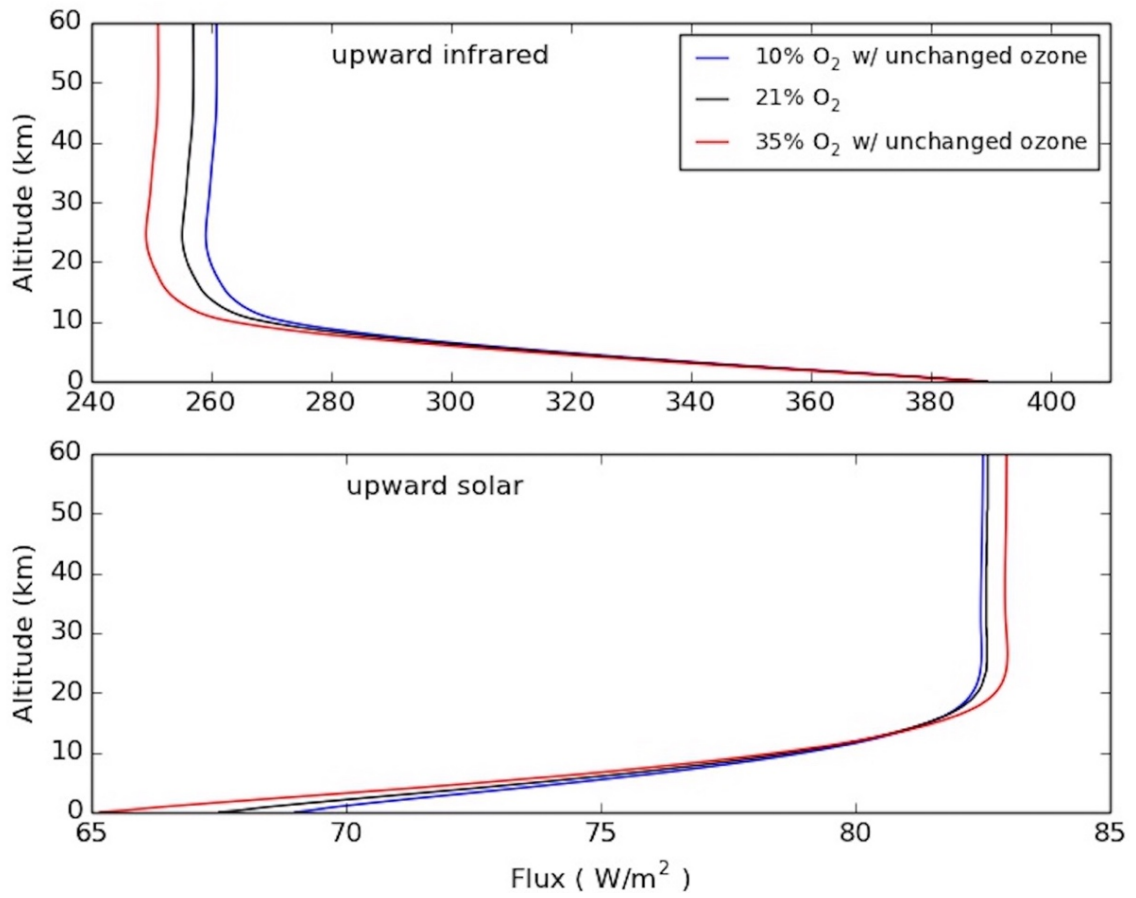


**Figure 3.1.** Plot of flux as a function of altitude for the one-step simulations, with O<sub>2</sub> levels of 10% (blue), 21% (black), and 35% (red).

**Table 3.2:** Effect of changing O<sub>2</sub> on radiative fluxes for one-step and converged simulations

O <sub>2</sub> %	Uncoupled one-step runs with unchanged O <sub>3</sub>			Converged runs with O <sub>3</sub> change		
	10%	21%	35%	10%	21%	35%
P <sub>s</sub> (kPa)	87.61	101.3	125.4	87.61	101.3	125.4
$\bar{M}$ (g/mol)	28.52	28.96	29.52	28.52	28.96	29.52
T <sub>s</sub> (K)	287.90	288.27	288.95	288.74	289.54	290.95
A <sub>p</sub>	0.2427	0.2429	0.2440	0.2390	0.2405	0.2431
TOA $F_{IR}^{up}$ (W/m <sup>2</sup> )	260.880	257.400	251.100	258.730	258.230	257.350
TOA $F_{SOL}^{up}$ (W/m <sup>2</sup> )	82.509	82.552	82.973	81.274	81.768	82.651
Surf $F_{SOL}^{dn}$ (W/m <sup>2</sup> )	255.58	250.53	241.37	252.12	248.22	241.72
TOA F <sub>tot</sub> (W/m <sup>2</sup> )	-3.3895	+0.0450	+5.9221			

non-greenhouse gases like N<sub>2</sub> and O<sub>2</sub> can broaden the greenhouse gas' absorption bands for infrared radiation, allowing it to absorb and interact with a broader wavelength range and thereby enhance its effectiveness as a greenhouse gas (Li et al., 2009). In other words, there is more greenhouse warming at higher surface pressure and less greenhouse warming at lower surface pressure, as expected (Goldblatt et al., 2009b). In our model, the change in the greenhouse effect caused by changing O<sub>2</sub> is greater than the change in planetary albedo, so the net radiative forcing is -3.39 W/m<sup>2</sup> at low O<sub>2</sub> and +5.92 W/m<sup>2</sup> at high O<sub>2</sub>. Our results are similar in sign and general magnitude to independent calculations performed by Goldblatt (2016) using the SMART (Spectral Mapping Atmospheric Radiative Transfer) line-by-line radiative transfer model. Thus, we would predict our

model should warm at higher  $C_{O_2}$  and cool at lower  $C_{O_2}$ , just the opposite of the results of the Poulsen et al. calculations.

The changes in outgoing solar radiation—and associated changes in planetary albedo—for the one-step radiative forcing calculations in Table 3.2 appear much smaller than those in Poulsen et al. (2016), and it is reasonable to ask why. First, as pointed out by Goldblatt (2016), Poulsen et al. evidently conflated Rayleigh scattering with Mie scattering by cloud particles (see further discussion below). Our model assumes clear skies, and so is not subject to such problems. Even so, the effects of Rayleigh scattering on outgoing solar radiation and planetary albedo are quite muted in our model. To see why, we ran additional one-step simulations with the surface albedo set to zero, so that the calculated upward solar flux ( $F_{SOL}^{up}$ ) and planetary albedo would be exclusively caused by Rayleigh scattering (Table 3.3); by comparison, the surface albedo is set to 0.27 in our standard model, effectively simulating the increased reflection caused by clouds. In these “Rayleigh scattering only” simulations,  $F_{SOL}^{up}$  increased by 3.25 W/m<sup>2</sup> as O<sub>2</sub> increased from 21% to 35%, and the planetary albedo increased by 13.73%. So, Rayleigh scattering does make a measurable difference in planetary albedo when the surface albedo is low. But for a higher surface albedo—or for a more realistic atmosphere in which the planetary albedo is dominated by clouds, as is the case on Earth—Rayleigh scattering is at best a second-order effect.

Although Poulsen et al. did not discuss the effects of pressure broadening, their version of the GENESIS climate model used the radiation code from CCM3 (Kiehl et al., 1998), which should include this effect. Indeed, one sees an increase in outgoing longwave radiation in their 10% O<sub>2</sub> case, similar to the increase calculated by our model (see their

Supp. Fig. 2b). So, the difference in results between the two models likely arise from other factors, such as the solar radiation code and/or cloud effects.

**Table 3.3:** Effect of changing O<sub>2</sub> on Rayleigh scattering and the corresponding change in planetary albedo for “Rayleigh scattering only” one-step simulations

O <sub>2</sub> %	TOA $F_{SOL}^{up}$ (W/m <sup>2</sup> )	A <sub>P</sub> from Rayleigh scattering only	$\Delta F_{SOL}^{up}$ from 21% O <sub>2</sub> (W/m <sup>2</sup> )	$\Delta A_P$ from 21% O <sub>2</sub>
10%	21.575	0.0635	- 1.942	- 8.24%
21%	23.517	0.0692	-	-
35%	26.768	0.0787	+ 3.251	+ 13.73%

#### 4. Converged model calculations

Our one-step radiative forcing calculations described above predict that the climate should warm at high O<sub>2</sub> and cool at low O<sub>2</sub>—just the opposite from that found by Poulsen et al. We then tested this prediction by running our own climate model to convergence for the high- and low-O<sub>2</sub> cases. Ozone should also change as O<sub>2</sub> changes, and we wanted to calculate the effect this would have on surface temperature. To do so, we used a 1-D photochemical model from Segura et al. (2003) to calculate ozone profiles for three different O<sub>2</sub> levels: 10%, 21%, and 35%. The CO<sub>2</sub> concentration was held constant at 355 ppmv for these calculations, while the concentrations of CH<sub>4</sub> and N<sub>2</sub>O were proportionately increased or decreased (from their present mixing ratios of 1.6 ppmv and 0.3 ppmv, respectively) to keep their column masses constant, as Poulsen et al. did. The O<sub>3</sub> profile was allowed to readjust with changing O<sub>2</sub>, and this had a measurable effect on our results.

Next, we coupled the calculated ozone profiles (Fig. 3.2) to the climate model and ran the climate model to convergence. Results are shown in Tables 3.2 and 3.4 and Figs. 3.3 and 3.4. The 21% O<sub>2</sub> control simulation has a marginally different surface temperature from the one-step calculation, normalized to 289.54 K, because the ozone profile is different from the one used to generate Table 3.2 (the one-step ozone profile is preset, while the converged ozone profile is calculated self-consistently for increased accuracy). Table 3.4 shows  $T_s$  calculated for 10% O<sub>2</sub> and 35% O<sub>2</sub> both with and without the calculated changes in ozone, as well as the difference in  $T_s$  from the control simulation.

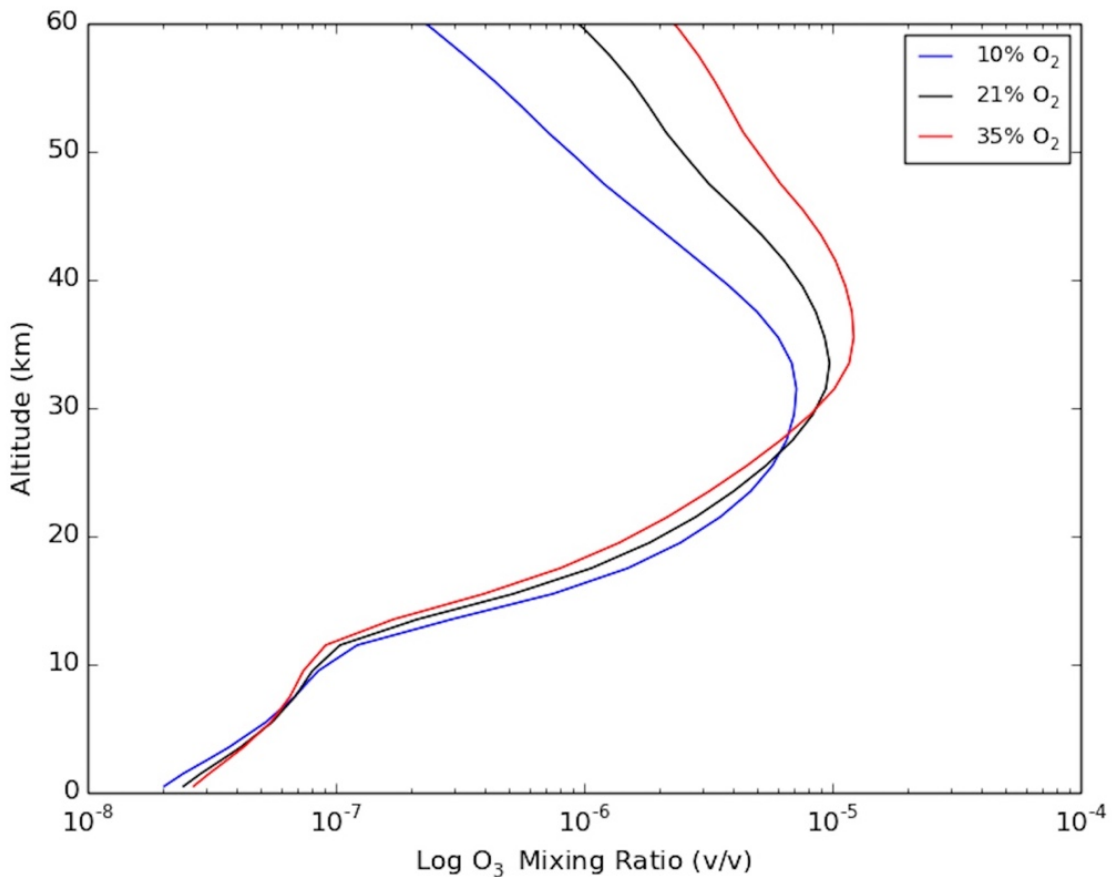


**Figure 3.2.** Vertical profile of ozone for the converged simulations.

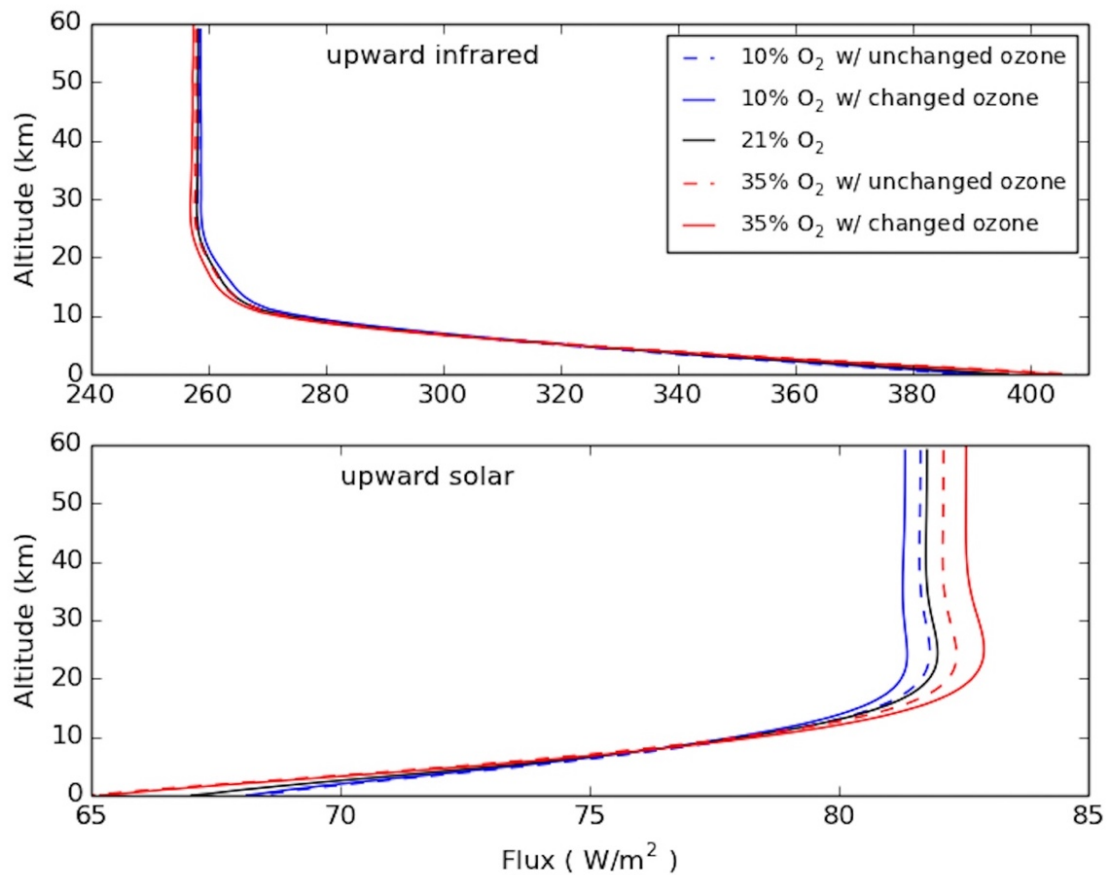


**Figure 3.3.** Plot of flux as a function of altitude for the converged simulations. Solid lines indicate simulations with changed ozone profiles according to the concentration of  $O_2$ , while dashed lines indicate simulations with an ozone profile matching that of the control (21%) run ('unchanged ozone').

---

**Table 3.4:** Effect of the changing O<sub>2</sub> on various surface parameters for converged runs with and without variable O<sub>3</sub>

O <sub>2</sub> %	T <sub>s</sub> (K)	ΔT <sub>s</sub> (K) from 21% O <sub>2</sub> control	A <sub>P</sub>	F <sub>SOL</sub> <sup>dn</sup> (surface)	O <sub>3</sub> column depth (molecules/cm <sup>2</sup> )
<b>10%, unchanged O<sub>3</sub></b>	288.31	- 1.23	0.2399	252.91	8.5079 × 10 <sup>18</sup>
<b>10% O<sub>3</sub> change</b>	288.74	- 0.80	0.2390	252.12	7.7598 × 10 <sup>18</sup>
<b>21% (control)</b>	289.54	0.0	0.2405	248.22	8.5079 × 10 <sup>18</sup>
<b>35%, unchanged O<sub>3</sub></b>	291.43	+ 1.89	0.2418	240.75	8.5079 × 10 <sup>18</sup>
<b>35% O<sub>3</sub> change</b>	290.95	+ 1.41	0.2431	241.72	9.8491 × 10 <sup>18</sup>

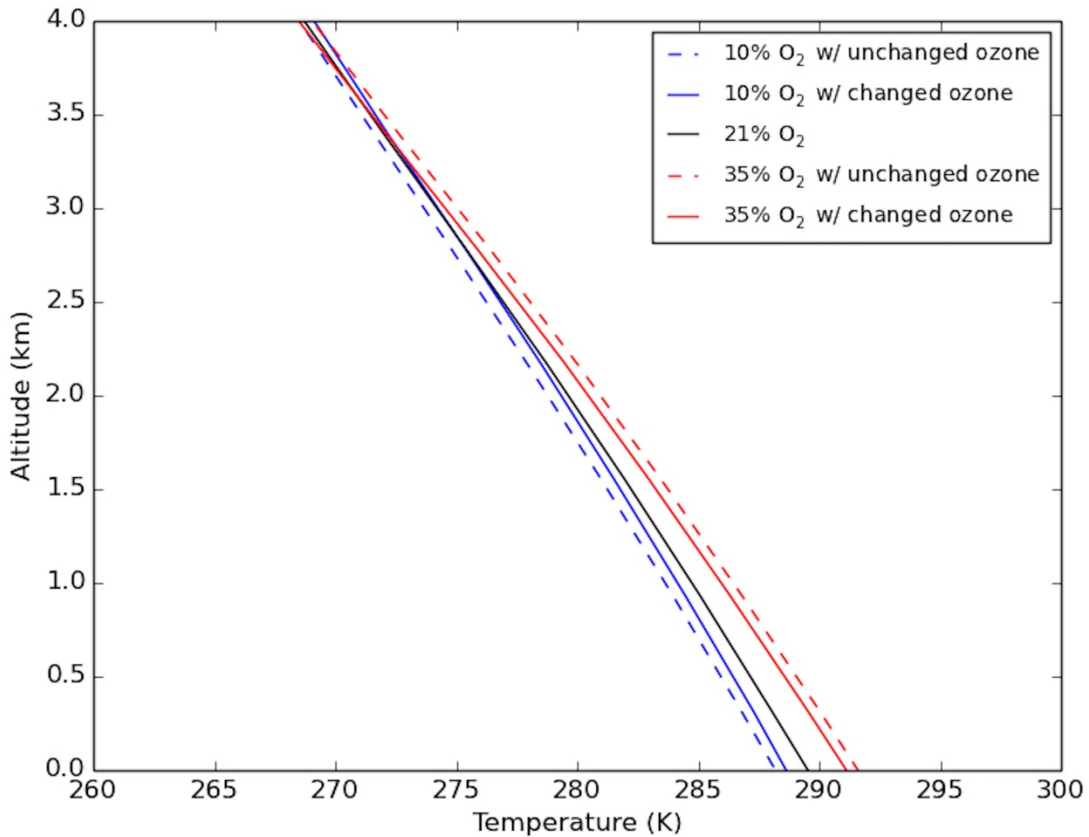


**Figure 3.4.** Vertical profile of temperature for the converged simulations.

By comparing the calculations with and without the ozone change included, one can estimate the effect of the changing ozone on surface temperature. Somewhat surprisingly, including the ozone change reduces  $\Delta T_s$  by a few tenths of a degree in both the 10% and 35% O<sub>2</sub> cases (Fig. 3.4). This may be because the ‘unchanged ozone’ simulations are actually unphysical, as the ozone layer has been either stretched or shrunk along with the log-pressure grid and is therefore no longer really the same as in the control run. The Poulsen et al. results could be similarly influenced by ozone. They used a prescribed seasonally and latitudinally varying modern ozone profile in all of their simulations, but their vertical grid should also change as the surface pressure changes. It is possible, therefore, that their ozone profile is technically unphysical and may be introducing additional minor errors to their temperature calculations.

We concentrate, then, on the two simulations we did in which ozone is modeled self-consistently. In this case, when O<sub>2</sub> is lowered to 10%,  $T_s$  decreases by 0.8 K. When O<sub>2</sub> is raised to 35%,  $T_s$  increases by 1.4 K. The changes are a factor of two smaller and in the opposite direction from those calculated by Poulsen et al. (the Poulsen model cooled by 2.3 K in the high O<sub>2</sub> case and warmed by 2.2 K in the low-O<sub>2</sub> case). We conclude that changes in the Rayleigh scattering optical depth—identified by Poulsen et al. as the main driver of O<sub>2</sub>-forced climate change—are likely not as important as those authors thought. Poulsen et al. combine Rayleigh and Mie scattering in their scaling analysis to result in a decrease in reflected sunlight in low-O<sub>2</sub> conditions. But, as Goldblatt (2016) points out in his comment, there is no reason that the number density of cloud droplets should scale with the number density of air molecules, as the relationship is not co-dependent in the atmosphere. Therefore, the scaling analysis used by Poulsen et al. cannot be justified.

Our own results are consistent with the predictions made earlier based on the instantaneous radiative forcing calculations made in Section 3 of this chapter: when  $O_2$  increases, the change in the greenhouse effect caused by increased pressure broadening outweighs the change in albedo caused by increased Rayleigh scattering; when  $O_2$  decreases, the decreased greenhouse effect has a greater impact on temperature than the decreased Rayleigh scattering. As for Poulsen et al., their results are highly dependent on cloud feedbacks, as they were careful to point out in their paper. Radiative forcing from clouds was 15 to 20  $W/m^2$  higher in the Poulsen et al. model than in other models, which would influence any potential cloud-driven warming (Goldblatt, 2016). Such feedbacks have been ignored in our 1-D climate model, in which the effects of clouds are instead parameterized by adopting a high surface albedo. This does not mean that the Poulsen et al. calculations are necessarily wrong, but it does suggest that their calculations should be checked with an independent 3-D climate model because cloud parameterizations are so uncertain.

## **5. Discussion**

### **5.1. Additional issues with the Poulsen et al. calculations**

We now return to the two observations that motivated the Poulsen et al. calculation. The first is that paleo- $CO_2$  levels were too low to explain the warm climate of the mid-Cretaceous and early Paleogene, and the second is that  $O_2$  levels were significantly lower in the Cretaceous than they are today.

Consider the  $CO_2$  argument first. Following Bice et al. (2006), Poulsen et al. cite a median  $CO_2$  concentration of 1120 ppmv for the Cenomanian stage, ~100 million years before present (Ma). But the Bice et al. error bars are at least a factor of two, with a quoted upper limit on  $CO_2$  of 2400 ppmv. Meanwhile, they estimate that tropical sea surface

temperatures were at least 5°C warmer than today. Global mean surface temperatures, then, were probably about 10°C warmer than today, assuming that the poles warmed up to 20°C, as did Cenomanian deep water (Friedrich et al., 2012). According to Bice et al., attaining these surface temperatures would require at least 4500 ppmv CO<sub>2</sub> in their GENESIS 2.0 3-D climate model. But different climate models have different sensitivities to increases in CO<sub>2</sub>. For a middle-of-the-road climate sensitivity of 3 degrees per CO<sub>2</sub> doubling (IPCC, 2014), a CO<sub>2</sub> concentration of 2400 ppmv (which represents ~3 doublings from the preindustrial CO<sub>2</sub> level of 280 ppmv) would produce about 9°C of warming on the modern Earth—almost the amount observed during the Cenomanian. Solar luminosity at 100 Ma was about 1% less than at present, though, which is equivalent to half a CO<sub>2</sub> doubling, or a temperature decrease of 1.5°C. So, we can account for about 7.5°C of warming out of a desired 10°C. There may indeed be a deficit of CO<sub>2</sub> during the Cenomanian but, if so, it is not that large, and it could be explained in other ways (such as higher climate sensitivity, or higher CH<sub>4</sub>), without invoking changes in O<sub>2</sub> concentration.

What about the postulated changes in atmospheric O<sub>2</sub>? Poulsen et al. cite two references on this subject: Falkowski et al. (2005) and Tappert et al. (2013). Berner was a coauthor on the Falkowski et al. paper, and they have relied on his geochemical cycle model (Berner & Canfield, 1989; Berner et al., 2000) for their predicted Cenomanian O<sub>2</sub> levels. An updated version of Berner's model is described in Berner (2006). This model is driven by the carbon isotope record in carbonates, which can be used to estimate the rate of burial of organic carbon in sediments. It predicts high atmospheric O<sub>2</sub> (~30%) around 300 Ma, following the deposition of the Carboniferous coal beds, and a minimum of O<sub>2</sub> (at ~12%) at the beginning of the Jurassic around 200 Ma. O<sub>2</sub> then increases steadily during

the Jurassic and Cretaceous, reaching approximately 18% by the Cenomanian (94-100 Ma). So, the Berner model does not offer much support for low O<sub>2</sub> during the period of greatest climatic warmth in the Cenomanian.

Moreover, O<sub>2</sub> models driven by carbon isotopes are poorly conditioned, as small errors in measured <sup>13</sup>C/<sup>12</sup>C ratios can cause considerable changes to the results. For example, a 1‰ change in δ<sup>13</sup>C (which is small compared to the scatter in the data) corresponds to a change in the organic carbon burial rate of ~2×10<sup>11</sup> mol/yr. When integrated over 10<sup>8</sup> years, this corresponds to an O<sub>2</sub> amount of ~2×10<sup>9</sup> mol, or about half the O<sub>2</sub> content of the modern atmosphere. This may explain why an alternative model for the evolution of atmospheric O<sub>2</sub> (Bergman et al., 2004), which is also driven by carbon isotopes, predicts 30% O<sub>2</sub> at 100 Ma. Both models are heavily influenced by the uncertainties in the data, as well as the particular form of their C-O cycle parameterization. Therefore, there is actually little geochemical support for the assertion by Poulsen et al. of low O<sub>2</sub> in the Cretaceous, and other models generally predict O<sub>2</sub> close to or in excess of its abundance in the modern atmosphere (Fig. 3.5).

The other paleo-O<sub>2</sub> reference cited by Poulsen et al. is Tappert et al. (2013). These authors estimate O<sub>2</sub> levels from δ<sup>13</sup>C in plant resins. The carbon isotopic composition of these resins is a complicated function of atmospheric O<sub>2</sub> and CO<sub>2</sub>. Higher CO<sub>2</sub> corresponds to lower O<sub>2</sub>. When the authors use the higher CO<sub>2</sub> levels calculated from models or inferred from pedogenic carbonates, they estimate O<sub>2</sub> concentrations of ~11% at 100 Ma (see their Fig. 10). So, this paper serves as the basis for the low Cenomanian O<sub>2</sub> levels preferred by Poulsen et al. Preserved δ<sup>13</sup>C in amber has been used to study organic carbon fractionation and oxidation, though generally as a means of estimating past CO<sub>2</sub> fractionation and

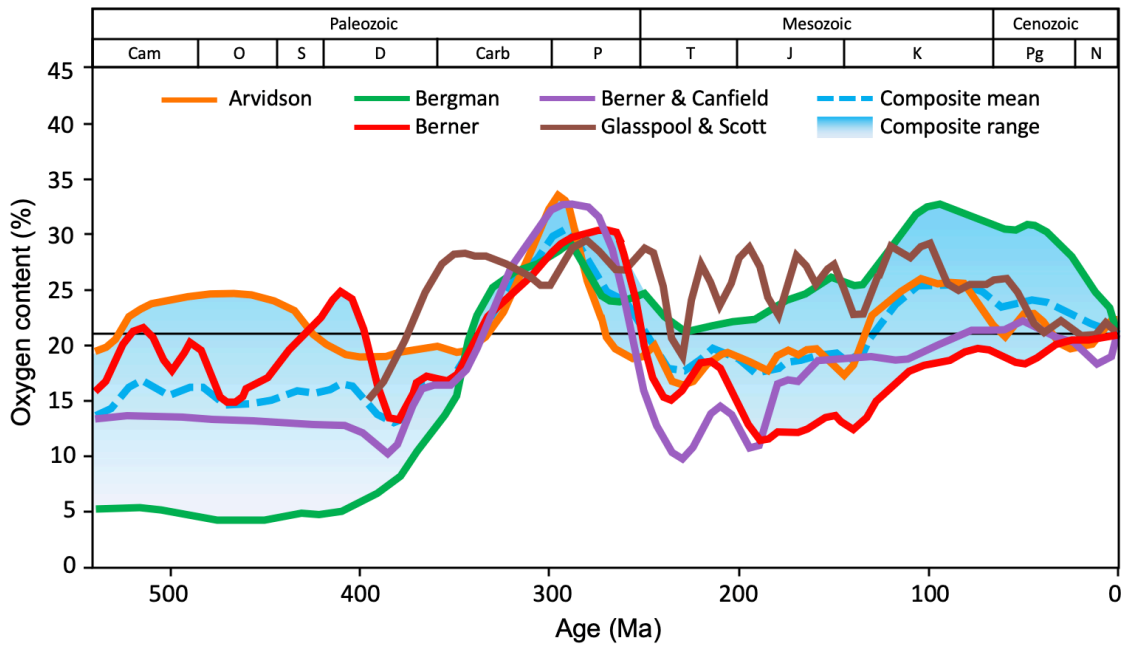


**Figure 3.5.** Atmospheric O<sub>2</sub> estimates for the Phanerozoic from multiple models—shown are trends from Arvidson et al. in orange (2013; MAGIC marine biogeochemistry model), Bergman et al. in green (2004; COPSE climate model), Berner in red (2009; GEOCARB model), Berner & Canfield in purple (1989; mathematical model), and Scott & Glasspool in brown (2010; “fire window” charcoal proxy model). The mean (blue dashed) and range (blue shaded) of the Arvidson et al., Bergman et al., and Berner O<sub>2</sub> estimates is indicated, as these most closely agree with ice core reconstructions (Stolper et al., 2016). Present-day O<sub>2</sub> is shown by the horizontal black line. Of note is that, though some estimates of O<sub>2</sub> at 100 Ma are below the modern level, most estimate O<sub>2</sub> was higher than 21%, and much higher than the 10% estimate from Poulsen et al. (2015). Figure modified from Wade et al. (2019).

oxidation, rather than as a measure of atmospheric O<sub>2</sub> (e.g. Lyons et al., 2019; Royer & Hren, 2017). It remains to be determined whether the connection between resin  $\delta^{13}\text{C}$  and paleo-O<sub>2</sub> from Tappert et al. (2013) is robust.

As one more reason for skepticism, we also wonder whether an O<sub>2</sub> level as low as 11% would have been enough to support the large, active dinosaurs and early placental mammals that lived during the Cenomanian, both of which have considerable oxygen

demands. O<sub>2</sub> abundance is considered an extrinsic control on gigantism; bigger terrestrial animals generally have a higher oxygen demand because of their massive size and energy demands (Beerling, 2017; Sander et al., 2011). The lung-air sac system of birds decrease weight and increase breathing efficiency, and may have evolved in massive sauropods (i.e. Brontosaurus, etc.) during the mid-Mesozoic (Lambertz et al., 2018) to maximize energy efficiency. But the presence of this system in sauropods is not certain and, moreover, other clades of dinosaur such as theropods (i.e. Tyrannosaurus rex, etc.) likely did not have this adaptation (Quick & Ruben, 2009). Placental mammals—first evolving between 100 and 65 million years ago (Archibald, 1996)—also have high atmospheric O<sub>2</sub> demands, as they require fairly high ambient oxygen to effectively facilitate this reproductive strategy (Falkowski et al., 2005). From a purely physiological standpoint, it seems that Cenomanian O<sub>2</sub> levels should have been relatively high.

## **5.2. Comparison with other 3-D models**

The results of our analysis suggest that the Poulsen et al. results appear to be driven largely by cloud feedbacks. This merits checking their results against other independent 3-D climate models, given the disagreement between our results and theirs and their deviation from the paradigm established by earlier models (namely Berner's GEOCARB model and Bergman et al.'s COPSE model, as discussed in Section 5.1). Recently, Wade et al. (2019) investigated the effect of changes in atmospheric O<sub>2</sub> on climate using the coupled atmosphere-ocean Hadley Centre Global Environmental Model version 3 (HadGEM3-AO) and Hadley Centre Coupled Model version 3 (HadCM3-BL) models. Following up on our work in Payne et al. (2016), Wade et al. compared their

model with the findings of Poulsen et al. and with our 1-D simulations, and examined the effect of O<sub>2</sub> on Phanerozoic climate.

Overall, Wade et al. found that pO<sub>2</sub> has a minor effect on Cretaceous climate, in agreement with our calculations described in this chapter. Wade et al. theorized that O<sub>2</sub> may have had an appreciable impact on climate earlier in the Phanerozoic (such as during the Permian, as tropical forests were developing and causing major shifts in atmospheric CO<sub>2</sub> and O<sub>2</sub>), but by the Cenomanian the effect of O<sub>2</sub> on surface temperature was likely minor. Wade et al. concluded, as we do, that cloud feedbacks drive much of the energy balance uncertainties and surface temperature changes in Poulsen et al. (2015), but that cloud feedbacks alone are not enough to explain the discrepancies. Error introduced by unphysical adjustment of atmospheric ozone or changing the partial pressure of O<sub>2</sub>, as discussed in this chapter, may explain the additional inconsistency.

The conclusions of Wade et al. (2019)—and of Goldblatt (2016), who first noted the GENESIS model's unusually strong cloud radiative forcings—support our findings discussed in this chapter, and reinforce the conclusion that the Poulsen et al. results are flawed. The complexity of the controls on atmospheric temperature and pressure, and the individuality of climate models in general, make it critical that model comparisons like this are performed when new climate drivers are proposed. The climate model intercomparison discussed here also highlights the complexity of cloud-related climate feedbacks, which are still not well understood.

## **6. Conclusions**

In conclusion, the effect of changes in atmospheric O<sub>2</sub> on surface temperature depends on the type of climate model used to study it. Our 1-D, coupled photochemical-

climate model predicts a response to changing O<sub>2</sub> levels that is about half as large and opposite in sign from that predicted by the 3-D climate model of Poulsen et al. The climatic response of our model is dominated by pressure broadening of absorption lines of CO<sub>2</sub> and H<sub>2</sub>O, which causes the greenhouse effect to increase at higher atmospheric O<sub>2</sub> levels and decrease at lower atmospheric O<sub>2</sub>. Changes in Rayleigh scattering push surface temperature in the opposite direction, but this effect is outweighed in our model by the change in pressure broadening. The Poulsen et al. results appear to be largely driven by cloud feedbacks, and both our calculations and the model comparisons conducted by Goldblatt (2016) and by Wade et al. (2019) indicate that their calculations are not robust. Given the large uncertainties in past levels of both O<sub>2</sub> and CO<sub>2</sub>, we agree with Berner (2006) that Phanerozoic climate has been driven largely by changes in atmospheric CO<sub>2</sub> and solar luminosity, coupled with changes in continental geography.

## Chapter 4.

# Long-term changes in atmospheric CO<sub>2</sub> and the carbon cycle throughout the Phanerozoic

### 1. Background

The major shifts in atmospheric composition over the course of the Phanerozoic make it essential that we hone our understanding of the sources, sinks, and processes that control the strength of the greenhouse effect. Changes in CO<sub>2</sub> and the C cycle in particular are a major focus of many models and biogeochemical analyses, and yet there is still work that needs to be done to refine our knowledge of Phanerozoic climate. In the previous two chapters, we focused on climate questions for two different times in Earth history, the Neoproterozoic and the early Cretaceous. In this chapter, we consider changes over time for the entire Phanerozoic, especially with respect to the processes that influence atmospheric CO<sub>2</sub> and climate in the last 100 Ma.

The classical view regarding the long-term control mechanism for CO<sub>2</sub> relies on the carbonate-silicate cycle (Bernier et al., 1983). In this cycle, CO<sub>2</sub> is outgassed from volcanoes and reacts with rainwater to facilitate the weathering of exposed silicate minerals on the continents. Runoff delivers the reacted CO<sub>2</sub> and silicate weathering products to the ocean, where most of these nutrients are used to make CaCO<sub>3</sub> shells. Some of these shells are, in turn, sequestered in carbonate sediments as these organisms die and their shells sink to the seafloor. CO<sub>2</sub> is eventually returned to the atmosphere over millions of years as the seafloor is recycled through plate tectonics. The rate of continental weathering dictates the drawdown of atmospheric CO<sub>2</sub>, and is dependent on surface temperature and the amount of continental runoff (Bernier, 2006) and, potentially, on pCO<sub>2</sub> directly (Walker et al.,

1981). On long time scales, the rate of silicate weathering increases as surface temperature increases—which can be the result of rising atmospheric CO<sub>2</sub>—resulting in a self-regulating, stabilizing climate feedback. This long-term cycle works in conjunction with short-term cycling of carbon, in which CO<sub>2</sub> is removed from the atmosphere by surface-dwelling photosynthetic organisms, both in the ocean and on the continents, and re-released via organic decay. Rapid changes in atmospheric CO<sub>2</sub> (< 1000 years) are dominated by the short-term feedback, but on longer timescales (> 10<sup>5</sup> years) the carbonate-silicate cycle maintains a stable climate and a quasi-steady state for atmospheric CO<sub>2</sub> and marine inorganic carbon (Royer et al., 2014).

There are, however, a number of complications to this long-term cycle. First, some authors have argued that the temperature dependence of continental weathering is weak (Krissansen-Totton & Catling, 2017; Walker, 1993) and that atmospheric CO<sub>2</sub> is affected more strongly by surface weatherability. Second, weathering may also occur on the seafloor, wherein Ca<sup>++</sup> ions are leached out of basalts extruded at midocean ridges and then deposited in carbonate veins and in seafloor pore space. This process acts as an additional marine CO<sub>2</sub> sink (Caldeira, 1995). Studies have suggested that this process occurs predominantly within the flanks of midocean ridges, away from the ridge axes, and can proceed at an appreciable rate in vent systems with temperatures as low as 15°C (Coogan & Gillis, 2018). As a result, deep-ocean temperatures can greatly influence the reaction rate. While seafloor weathering plays a relatively minor role compared to continental weathering today, it may have been much more significant in the global C cycle during warm periods of Earth history that saw higher deep ocean temperatures, such as the Mesozoic (Coogan & Dosso, 2015; Coogan & Gillis, 2013) and specifically the Cretaceous

around ~100 Ma (as we discussed in Chapter 3). Third, biology introduces additional complications to the carbonate-silicate weathering cycle, particularly during the Phanerozoic. During the early Phanerozoic, before the advent of vascular plants, atmospheric CO<sub>2</sub> and soil CO<sub>2</sub> should have been closely correlated, as the amount of CO<sub>2</sub> stored in soil would have been a function of its degree of contact with the air. But as vascular land plants evolved and established themselves on the continents, organic decay and the advent of subsurface respiration in plant root systems would have caused soil pCO<sub>2</sub> to become many times greater than atmospheric pCO<sub>2</sub> (Mora et al., 1991). These vascular plants first evolved in the late Ordovician Period (by ~444 Ma) and quickly spread and diversified. This is evidenced by the abundance of plant fossils with xylem (water-conducting plant tissue that helps to form self-supporting woody stems) and stomata (specialized plant cells, commonly found in leaves, which control gas and water exchange between the plant and atmosphere) found in the ~410 Ma Rhynie Chert formation (Hetherington & Dolan, 2019; Kidston & Lang, 1921). The expansion of terrestrial forests—most notably, the vast swamp forests that formed the hallmark coal formations of the Carboniferous, from ~359 to ~299 Ma—and the subsequent rise in terrestrial carbon storage is often linked to the decline of CO<sub>2</sub> from a major to a minor atmospheric constituent (Royer, 2013; Berner, 2006; Bergman et al., 2004).

Several different proxies have been used to estimate paleo-atmospheric pCO<sub>2</sub> over the course of the Phanerozoic. Some of the most commonly used proxies include paleosols (which we discussed in Section 4.2 of Chapter 2, in relation to their estimates and reliability during the Archean, about 2 billion years earlier than the span of Earth history we discuss in this chapter) and leaf stomatal density, though there are a multitude of other approaches

for estimating ancient pCO<sub>2</sub>. These proxies predict a general decrease of atmospheric CO<sub>2</sub> from high levels (> 1000 ppm) early in the Phanerozoic to the comparatively low level today (with a pre-industrial concentration of ~280 ppm), with limited periods of increase at ~200 Ma and ~100 Ma (Royer, 2013). There is general agreement between most of the established proxies in their projections of Phanerozoic changes in pCO<sub>2</sub>. That said, all proxies are subject to their own biases. The age, quality, and availability of samples can influence the accuracy of pCO<sub>2</sub> estimates, and uncertainty generally increases as pCO<sub>2</sub> increases (see Fig. 4.1a) and can vary by multiple orders of magnitude (Royer et al., 2014). Overall, while current proxy data gives us a broad picture of trends in pCO<sub>2</sub> over the Phanerozoic, considerable uncertainty remains concerning the magnitude of episodes of increased atmospheric CO<sub>2</sub>, and so proxy data alone cannot give the full picture.

There have been several published efforts to simulate changes in atmospheric CO<sub>2</sub> as well. Most of these models do so by parameterizing CO<sub>2</sub> burial, weathering, and degassing fluxes over time, and they generally agree with proxy evidence—though it could be argued that they just contain enough adjustable parameters to be tuned to broadly coincide with their contained proxy data. The most widely cited and well-known model is Berner's GEOCARB model (Berner, 2006a; Berner, 2006b; Berner & Kothavala, 2001). The GEOCARB model predicts a decline from high CO<sub>2</sub> in the early Phanerozoic to lower concentrations towards the end of the Devonian, with small-scale fluctuations in atmospheric CO<sub>2</sub> throughout the late Phanerozoic (Fig. 4.1b). This generally matches estimates from proxy data, although there are some periods of major disagreement in the Mesozoic and Cenozoic (Royer et al., 2014). However, GEOCARB derives its rate for C burial using C isotope ratios that may not represent a global average (Saltzman & Edwards,

2017), and it does not include seafloor weathering (Krissansen-Totton & Catling, 2017). As we mentioned in Section 5.1 of Chapter 3, small errors in  $^{13}\text{C}/^{12}\text{C}$  ratios can cause sizeable errors when calculating the rate of C burial; most pre-Cretaceous  $\delta^{13}\text{C}$  measurements are taken from inland sea deposits which are isotopically decoupled from the open ocean and can exhibit internal isotopic disparities due to geography. Another well-known model is COPSE (Carbon-Oxygen-Phosphorus-Sulfur-Evolution), which is a process-driven model rather than an isotope-driven model, and which has also been used to model  $p\text{O}_2$  (Bergman et al., 2004; Lenton et al., 2018). COPSE estimates organic C burial rates from biological activity and therefore tracks C isotopes as oxygen tracers rather than oxygen forcers. But it also shares much of its C cycle infrastructure with GEOCARB. Thus, COPSE is ultimately subject to many of the same issues with its handling of the global C cycle as GEOCARB.

A more recent contribution to modeling the global C cycle is a box model by Krissansen-Totten & Catling (2017) (K-T&C 2017). These authors developed a 2-box model of the global C cycle that includes both continental and seafloor weathering. The model solves a series of equations for partitioning of total C between the atmosphere-ocean system and seafloor pore space over time. Their model utilizes a statistical (Bayesian) approach that makes it wholly process-driven without drawing on the same isotope data as earlier models. They also considered long-term effects on climate sensitivity to  $p\text{CO}_2$ , such as ice sheet retreat and boreal forest decline. Most climate models focus exclusively on rapid feedbacks such as changes to water vapor or ice caps, as stipulated by equilibrium or “Charney” climate sensitivity (Charney et al., 1979), based on the assumption that long-term feedbacks are too slow to matter. The IPCC estimates of 1.5 to 4.5 K per  $\text{CO}_2$  doubling

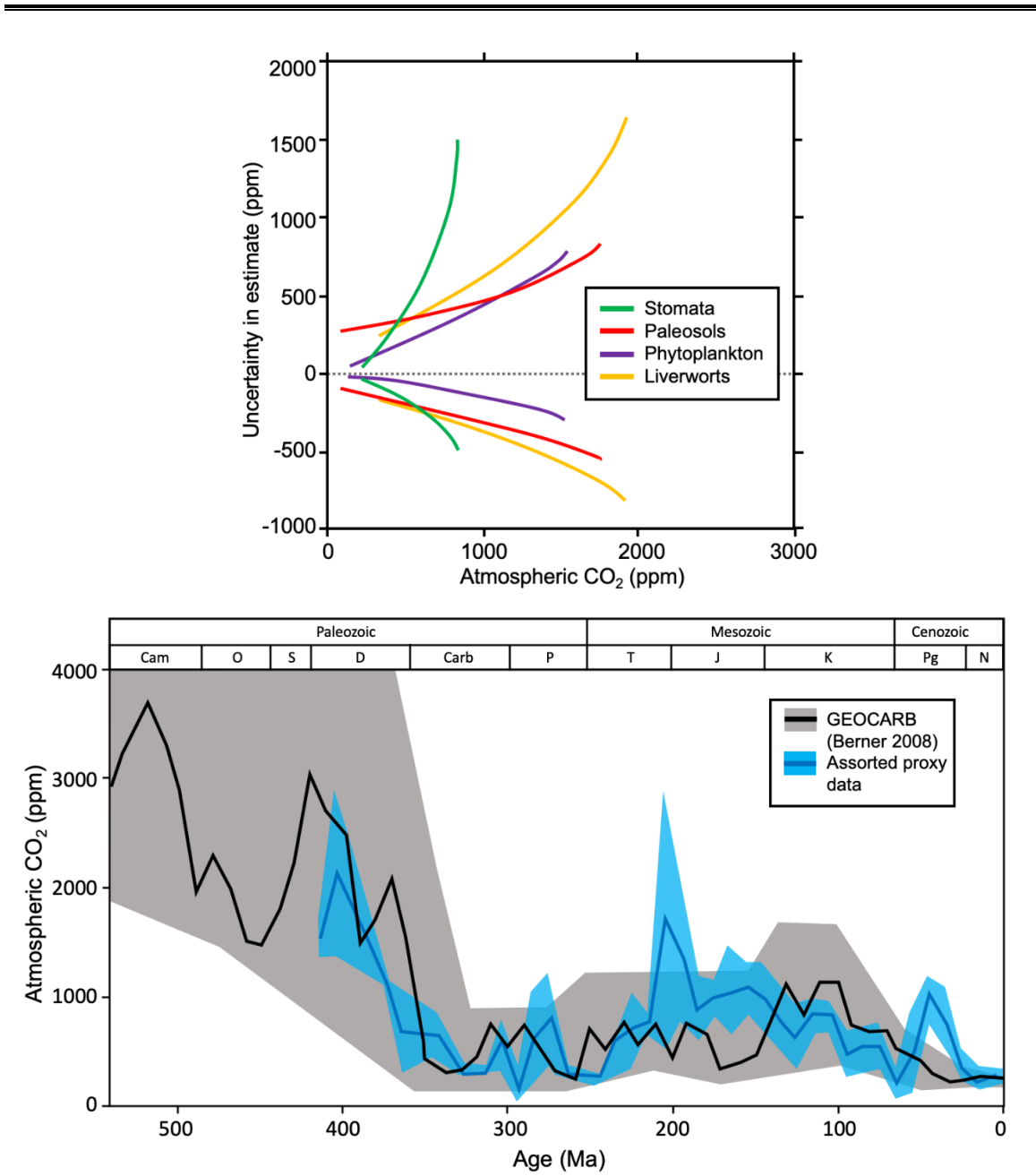


**Figure 4.1: (top)** Error analysis for various atmospheric CO<sub>2</sub> proxies. Curved lines represent regression fits (CO<sub>2</sub> versus associated error) of several studies for each proxy type. Positive and negative errors computed separately. Figure modified from Royer (2014).

**(bottom)** Phanerozoic history of atmospheric CO<sub>2</sub> from GEOCARB and various proxies. Solid lines indicate average, with shaded regions denoting error margin. GEOCARB calculations are shown in black/grey; proxy data shown in blue are represented in collective bins spanning 10 million years each. Figure modified from Royer (2014).

follow this reasoning. However, when considering climate on a longer timescale (such as over millions of years), it becomes essential to consider these slower feedbacks, as they can make a considerable difference (Knutti et al., 2017). The K-T&C model supports this hypothesis, as their model predicts a long-term climate sensitivity to pCO<sub>2</sub> of  $5.6_{-1.2}^{+1.3}$  K per CO<sub>2</sub> doubling, much higher than the IPCC range. K-T&C calculated an activation energy ( $E_A$ ) for continental weathering of  $20_{-5}^{+10}$  kJ/mol (much lower than earlier values of  $E_A$ ), implying that the silicate weathering rate is less temperature-dependent than previously thought. They concluded that continental weatherability has increased by a factor of 1.7-3.3 over the last 100 My, due to continental uplift and changes in continental area.

Close examination of the K-T&C model reveals several assumptions that may have influenced the results. The treatment of the atmosphere-ocean system as a single box in their model creates potential problems with their handling of temperature and pH gradients. First, the lack of a biological pump in their model makes it difficult to accurately compare their calculated pH to proxy data. The deep ocean is slightly more acidic than the surface ocean, due to the decay of organics and respiration at depth, but the proxy data used by K-T&C (2017) are representative of surface ocean pH only (Anagnostou et al., 2016). Second, the K-T&C model assumes that surface and deep ocean temperatures change at approximately the same rate. But data and model simulations of modern global warming indicate that temperatures in the deep ocean rise more quickly than surface ocean temperatures, due to the amplification of warming at the poles where deepwater forms. This means that the fixed surface-to-deep ocean temperature gradient in the K\_T&C model likely leads to an underestimate of deep ocean warming, along with the effect this would have on seafloor precipitation and dissolution. Third, the K-T&C model implies a need for

a change in continental weatherability over the last ~100 Ma but offers little explanation of why such a shift would have occurred. They suggest several possibilities—including changes in sea level, changes in erosion, and the emergence of angiosperms and fungi at ~100 Ma—but ultimately do not offer a compelling solution.

In this chapter, we explore and expand on recent developments in modeling Phanerozoic CO<sub>2</sub>. To explore the influences on the global C cycle, we created a box model that builds on the K-T&C (2017) framework but gives greater consideration to variables such as pH and the surface-deep ocean temperature gradient. We then used our model to revisit the K-T&C calculations for continental weatherability and the temperature dependence of weathering, and we compare our results to those of Walker et al., Berner, and K-T&C. We then combine our model projections with new understanding of geography and uplift during the last ~100 Ma—such as that of MacDonald et al. (2019)—to discuss large-scale trends in C cycling over that time.

## **2. Methods**

### **2.1. Model development**

Both the K-T&C (2017) model and our box model calculate ocean chemistry explicitly, with consideration given to both carbonate chemistry and alkalinity. Both models also include pH- and temperature-dependent kinetics, which have classically been arbitrarily assigned or considered only in isolation (i.e., Berner, 2008; Berner, 2006; Caldeira, 1995), to calculate the time evolution of the carbon cycle. This box model approach is also unique because many parameters—such as continental weatherability, precipitation and dissolution rates, and the marine temperature gradient—are defined as a range rather than as a fixed value. Outputs are therefore distributions based on parameter ranges, and this makes it possible to calculate a best fit and confidence range for outputs in

spite of uncertainties in some of the coefficients. Geochemical equations and kinetics drive the model, with proxy data serving only as points of comparison for the model output.

As mentioned above, K-T&C divided the atmosphere-ocean-seafloor system into two boxes (Fig. 4.2, a), isolating the seafloor. In our model, we track carbon and alkalinity fluxes into and out of three boxes (Fig. 4.2, b)—the atmosphere-surface ocean, the deep ocean, and seafloor pore space—to more realistically study the effect of surface-to-deep ocean pH and temperature gradients on seafloor precipitation and dissolution. Carbon enters the atmosphere-surface ocean through carbonate and silicate weathering on the continents, as well as through volcanic outgassing. Weathering creates an alkalinity flux into the atmosphere-surface ocean; the ingoing and outgoing alkalinity fluxes are double any accompanying carbon flux because the uptake or release of one mole of carbon (as carbonate) is balanced by a cation with a charge of 2+, e.g.,  $\text{Ca}^{2+}$ . C and alkalinity leave the ocean via carbonate burial on the relatively shallow continental shelves as well as carbonate deposition in the deep ocean, and by two-way mixing between the deep ocean and seafloor pore space as seawater circulates. Additional alkalinity is supplied to the pore space by dissolution of the basalts that make up much of the seafloor, and alkalinity and C are lost from pore space as carbonates precipitate out. Details on the dynamical equations and model setup can be found in the Methods section and in the Supplemental Information section of K-T&C (2017).

C and alkalinity are exchanged at steady fixed rates between the surface and deep ocean. However, our 3-box model incorporates a pH gradient between the surface and deep ocean that is parameterized similarly to observations of the modern ocean, where the deep ocean is approximately half a log unit more acidic than the surface ocean due to the sinking

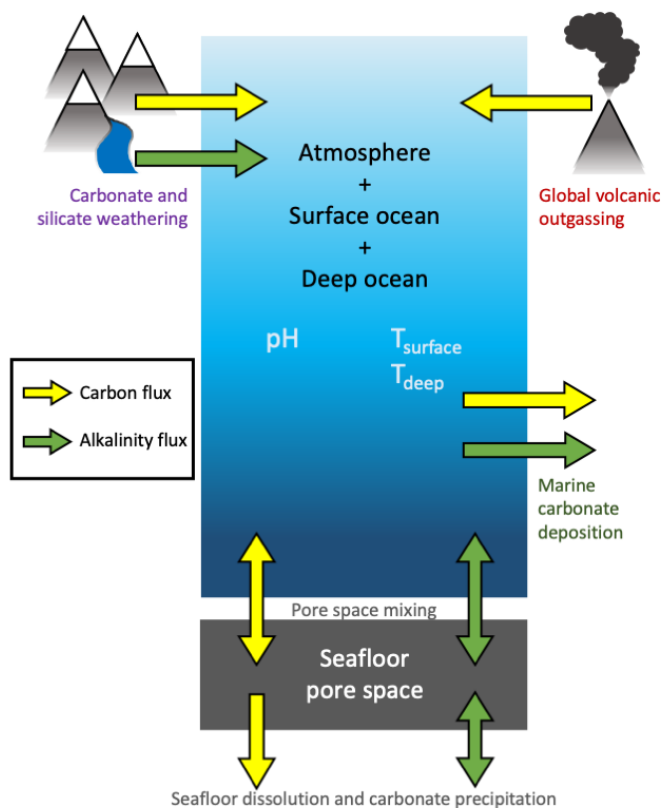
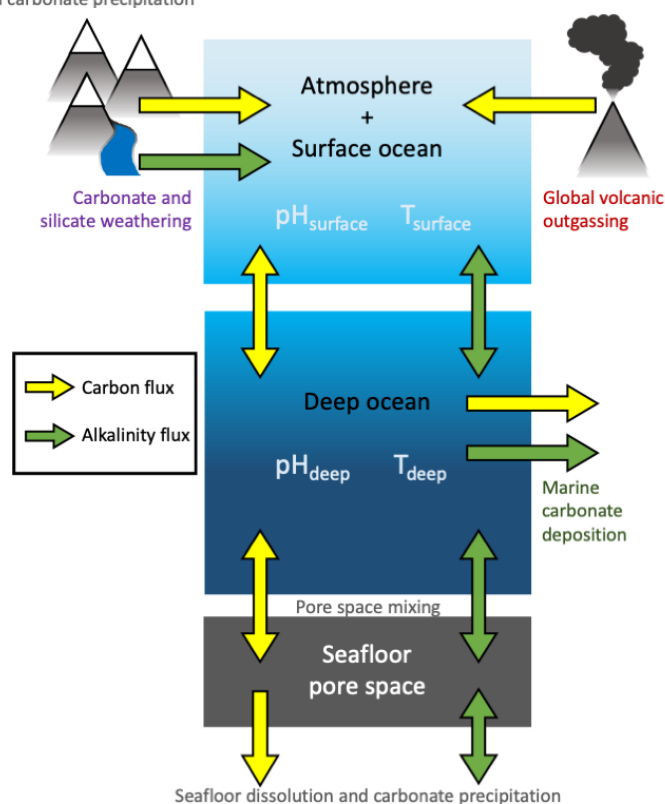


**Figure 4.2 (a):** Simplified schematic of K-T&C (2017) box model. Yellow arrows represent C fluxes, while green arrows represent alkalinity fluxes. Total C and alkalinity within the atmosphere-surface ocean-deep ocean and the seafloor pore space is determined based on reservoir mass, fluxes, and internal chemistry. Alkalinity fluxes are twice those of C because the uptake/release of one mole of C as carbonate is balanced by a 2+ cation.

**Figure 4.2 (b):** Simplified schematic of the modified box model used in our calculations. Both the C and alkalinity fluxes are the same as in the K-T&C model, but the deep ocean is a distinct box in our version, allowing for a more realistic calculation of pH and temperature gradients and the effect this has on seafloor C storage. We also modify continental weatherability and its temperature dependence.



and decay of organics via the biological pump (Kump et al., 2010). K-T&C did not include a biological pump in their model, arguing that its relatively fast response time ( $< \sim 1000$  years) would not have lasting effects on C cycling. But the difference between surface and deep ocean pH that is in part generated by the biological pump may have an appreciable effect on the ocean's saturation state and the precipitation/dissolution of seafloor carbonates, so we include this in our 3-box model. We also implement a surface-deep ocean temperature gradient derived from modern 3-D global climate models. K-T&C assumed that surface ocean and deep ocean temperatures change at approximately the same rate. But more detailed ocean modeling tells a different story: at high latitudes (specifically the Arctic), temperatures increase at a faster rate than the global mean temperature. This “polar amplification” of warming in coupled atmosphere-ocean GCMs causes polar temperatures to increase 1.5 to 4.5 times faster than global mean warming (Holland & Bitz, 2003). The magnitude of polar amplification decreases in warmer climates as ice cover decreases. If one assumes that the temperature of ocean deepwater—which today forms at high latitudes—always reflects polar temperatures (Poulsen & Zhou, 2013), then the rate of change for surface and deep ocean temperatures should not be the same. Accurately representing the surface-to-deep ocean temperature gradient is important for quantifying modern climate change, and is potentially even more important during warmer periods when it could trigger major shifts in the balance between seafloor C sources and sinks. Thus, we parameterize the surface-to-deep ocean temperature gradient based on the estimates from Holland & Bitz (2003).

## 2.2. Activation energy calculations

In addition, we reevaluated the temperature dependence—and  $E_A$ —of continental weathering following the same methods as K-T&C (2017). Both Walker et al. (1981) and K-T&C (2017) expressed the continental silicate weathering flux by scaling it with  $p\text{CO}_2$  and surface temperature in the modern atmosphere, such that

$$F_{\text{sil}} = \omega F_{\text{sil}}^{\text{mod}} \left( \frac{p\text{CO}_2}{p\text{CO}_2^{\text{mod}}} \right)^\alpha \exp\left(\frac{\Delta T_s}{T_e}\right) \quad (1)$$

where  $F_{\text{sil}}$  is the continental silicate weather flux (in Tmol/year),  $F_{\text{sil}}^{\text{mod}}$  is the modern continental silicate weathering flux,  $\omega$  is the weatherability,  $p\text{CO}_2$  is the actual atmospheric  $p\text{CO}_2$ ,  $p\text{CO}_2^{\text{mod}}$  is atmospheric  $p\text{CO}_2$  in the modern atmosphere,  $\alpha$  is a coefficient representing the relationship between atmospheric  $p\text{CO}_2$  and soil  $p\text{CO}_2$ ,  $\Delta T_s$  is the difference between the global mean surface temperature at a given time and the pre-industrial global mean temperature, and  $T_e$  represents the temperature dependence of continental weathering. In Equation 1,  $p\text{CO}_2$  is modified by an exponent  $\alpha$ , which has a range of 0.2 to 0.5 in the model based on measurements of soil pH at a given atmospheric  $\text{CO}_2$  (Volk, 1987).  $F_{\text{sil}}^{\text{mod}}$  is modified by a dimensionless weatherability factor,  $\omega$ , that represents the change in continental weatherability in the past when compared to the modern. Changes in  $\omega$  serve to represent changes in sea level, geography, lithology, and biology collectively. Higher weatherability indicates an increase in weatherable material on the continents (for instance, by exposure of more land due to a drop in sea level, or by creation of new continent via tectonic activity).  $\Delta T_s$  is the global mean surface temperature in the past minus the pre-industrial global mean surface temperature. We use a value of

~285 K for the pre-industrial global mean temperature in our calculations because this is the temperature used by K-T&C, and our aim was in part to compare to their results (however, we note that this is 1-2 K cooler than the actual pre-industrial global mean surface temperature; see Kump et al., 2010).  $T_e$  is a parameter that represents the temperature dependence of continental weathering; this term is broadly defined by the approximate change in temperature needed to increase or decrease the weathering rate by a factor of  $e$ . Following Walker et al. (1981), K-T&C relate this “e-folding temperature,”  $T_e$ , to an effective activation energy ( $E_A$ ) for continental weathering by the relation:

$$T_e \approx \frac{RT_S^2}{E_A} \quad (2)$$

where  $T_S$  is surface temperature,  $E_A$  is in J/mol, and  $R$  is the universal gas constant (~8.314 J/mol K). The relationship between  $T_e$  and  $E_A$  is approximate because the kinetic temperature dependence and the temperature dependence of runoff are combined in  $T_e$ , as in the K-T&C model and previous modeling efforts.  $E_A$  represents the energy needed for the breakdown of silicate rocks on the continents. Estimates of the temperature dependence,  $T_e$ , have been made for modern silicate weathering using catchment field studies of feldspars and other silicates (i.e., Velbel, 1993). Velbel estimated that  $T_e$  is on the order of ~9 K, corresponding to an  $E_A$  of ~77 kJ/mol. A high  $E_A$  (and low  $T_e$ ) indicates an extremely strong negative feedback for atmospheric CO<sub>2</sub>. A smaller activation energy (and high  $T_e$ ) suggests that the continental weathering feedback is not as closely linked to surface temperature and is a weaker negative feedback. Walker et al. (1981) included a temperature dependence with an  $E_A$  equivalent to ~50 kJ/mol (corresponding to a  $T_e$  of

13.7 K), while GEOCARB (Berner, 2006) utilized an  $E_A$  of  $\sim 75$  kJ/mol (meaning,  $T_e = \sim 9$  K), based in part on chemical weathering field studies (West et al., 2005). But K-T&C found that their “best fit” case (meaning, their model simulations that fit most closely to proxy data without using the proxy data as priors in a statistical analysis) required a much higher  $T_e$  of approximately 30 to 40 K, meaning the  $E_A$  of continental weathering would only be  $\sim 20$  kJ/mol in their projections for climate over the last 100 Ma. It is worth noting that K-T&C obtained an even better fit using a Bayesian statistical analysis that uses proxy data as priors; while the Bayesian approach allows for more quantitative conclusions, the approach we use in our calculations in this chapter present a qualitative look at climate trends in the last 100 Ma. With this in mind, we test a range of values for  $T_e$ , covering the range from K-T&C to GEOCARB.

We ran 100 simulations with our 3-box model, with increasingly narrow parameter ranges for the model’s input parameters (see Tables 1 and 2 from K-T&C (2017)). For each simulation, our 3-box model was run for 10,000 iterations to reach a stable solution. Each iteration sampled uniformly within each of the parameter ranges and then plotted the resulting change over time for outputs such as atmospheric  $\text{CO}_2$ , ocean temperatures, and carbonate precipitation and dissolution. The results of each simulation were then compared to the proxy data used in the K-T&C model, binned in 10-million-year intervals. The “best fit” was determined in the same manner as the K-T&C best fit referenced above—the “best fit” case encompassed the most proxy data within the 95% confidence interval for all of the time series model outputs.

As part of our simulations, we ran several cases testing the effects of a stronger pH gradient and a stronger surface-deep ocean temperature gradient in isolation. We then ran

several cases with varied values for the activation energy of continental weathering, with our pH and temperature gradients, between the low K-T&C estimate and the much higher Walker et al. estimate. We did the same with varied past weatherability coefficients, ranging from the lowest estimate from the confidence range in K-T&C (0.3) to a value equal to modern weatherability (1.0) and increasing linearly with time. From the results of these simulations, we calculated a new  $E_A$  using the equations above, following the methodology of K-T&C, and the median  $T_e$  from our “best fit” case.

### **3. Results**

We assess the importance of more realistic surface-to-deep ocean pH and temperature gradients on the global C system by comparing our model, with these changes only, to the K-T&C (2017) “base case”. In this case, they used the weathering temperature dependence calculated by Walker et al. (1981), no change in weatherability with time, no pH gradient, and an equal rate of temperature change in the surface ocean as in the deep ocean. We compare their base case with the modified pH and temperature regime used for our 3-box calculations in Figure 4.3, to isolate their effect from changes in continental weathering.

Deep ocean temperature had the greatest effect on the saturation state of pore space, as well as seafloor carbonate precipitation and dissolution. The separation of the surface and deep ocean in our 3-box model, and the inclusion of a surface-deep ocean temperature gradient, brings all of the deep ocean temperature proxy data within the confidence interval on its own (Fig. 4.3, B’). The median carbonate dissolution flux at 100 Ma in our 3-box model is likewise in close agreement with proxy data (Fig. 4.3, C’). The inclusion of a pH gradient between the surface and deep ocean had only a minor effect on saturation state,

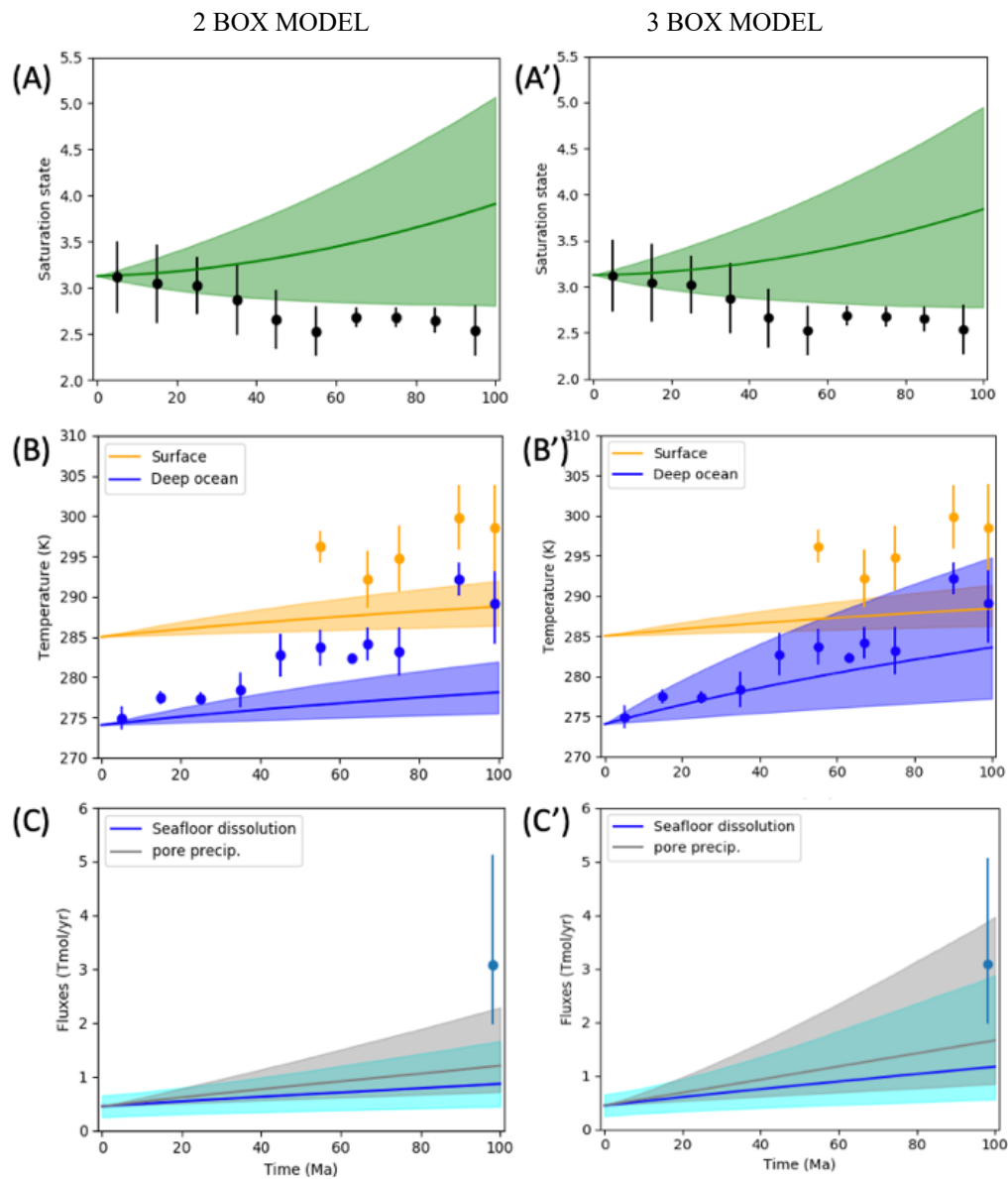


**Fig. 4.3:** Carbon cycle model output for K-T&C 2-box model (A, B, C) and our 3-D box model (A', B', C') for the last 100 Ma. Geochemical proxy data (see K-T&C (2017) for the full list of proxy sources) indicated by dots with bars representing the 95% confidence interval for each. Model median outputs shown by solid lines, with 95% confidence intervals indicated by the corresponding shaded region. Panels denote (A and A') marine saturation state, (B and B') surface and deep ocean temperatures, and (C and C') seafloor dissolution and precipitation carbonate fluxes. The surface-deep ocean temperature gradient in the K-T&C model cases was 0.8-1.4 (meaning rate of temperature change in the deep ocean is 0.8 to 1.4 times that in the surface ocean), while our model implemented a gradient of 1.5-4.5 based on GCM simulations. Our pH gradient resulted in a deep ocean pH 0.5 log units lower than in the surface ocean.

decreasing it by  $\sim 0.2$  (Fig. 4.3, A'). (The term 'saturation state' refers to the factor by which the whole ocean is supersaturated with respect to  $\text{CaCO}_3$ , as in the K-T&C model.) The minor decrease in saturation state reflects a slight decrease in the concentration of available  $\text{CO}_3^{2-}$  in the deep ocean and in pore space, as would be expected in a more acidic marine environment. But greater deep ocean warming in the past, at least in part as a result of polar amplification, has a much larger effect on the fluxes of carbonate precipitation and dissolution, both of which approximately doubled at 100 Ma compared to the original K-T&C calculation.

Separating the surface and deep ocean in our model does have an appreciable effect on the balance between seafloor carbonate sinks and sources. However, these changes to the marine component of the global C system are not enough to create full agreement between the model and all of the proxy data. In their "best fit" case (Fig. 4.4), K-T&C (2017) found that a significant decrease in the temperature dependence of continental weathering—and overall weatherability during the Cretaceous 100 Ma—was needed to fit the data. K-T&C obtained the best fit model output by assuming a weak temperature dependence and overall lower past weatherability for silicate weathering on the continents. An e-folding temperature of 30-40 K, combined with weatherability 40-60% as strong as today, resulted in the best fit with the geochemical data.

We found, with the addition of a stronger surface-deep ocean temperature gradient and biological pump, that weaker weatherability and temperature dependence improved our fit with proxy data (Fig. 4.5), in agreement with K-T&C. Our best fit was obtained with an e-folding temperature,  $T_e$ , of  $23_{-5}^{+9}$  K and Cretaceous weatherability equal to 50-60% of the modern value. Using Equation 2, this corresponds to an  $E_A$  for continental weathering

of  $29_{-8}^{+8}$  kJ/mol. This suggests a weaker temperature dependence than predicted by both Walker et al. ( $\sim 50$  kJ/mol) and Berner ( $\sim 75$  kJ/mol), but not as low a value as that proposed by K-T&C ( $20_{-5}^{+10}$  kJ/mol). It also supports lower continental weatherability during the Cretaceous, on the order of what K-T&C suggest in their calculations.

Our “best fit,” with these parameters, broadly agrees with all of the K-T&C proxy data save for one pH datapoint (Figs. 4.4, 4.5). Our best fits from our time series analysis are generally comparable with the “best fit” from K-T&C, with the exception of our deep ocean temperature fits, and show a strong fit with atmospheric CO<sub>2</sub> and seafloor dissolution in particular.

It is worth noting is that our 3-box model median estimate for deep ocean temperatures does include a deep ocean temperature range that is warmer than the surface ocean at 100 Ma. This prediction is admittedly unphysical—however, the confidence interval for deep ocean temperatures at 100 Ma includes temperatures below that of the surface ocean. The wide range of high deep ocean temperatures in the past that our 3-box model estimates emphasizes the variability introduced by a stronger surface-deep ocean temperature gradient and polar amplification introduce. Utilizing a Bayesian analysis for our 3-box model surface-deep ocean temperature gradient would help to more tightly constraint the strength of this gradient in the last 100 Ma. Our results shown in Fig. 4.5 do, however, predict a significantly warmer deep ocean in the past that would have strongly influenced seafloor carbonate precipitation and dissolution in the deep ocean.

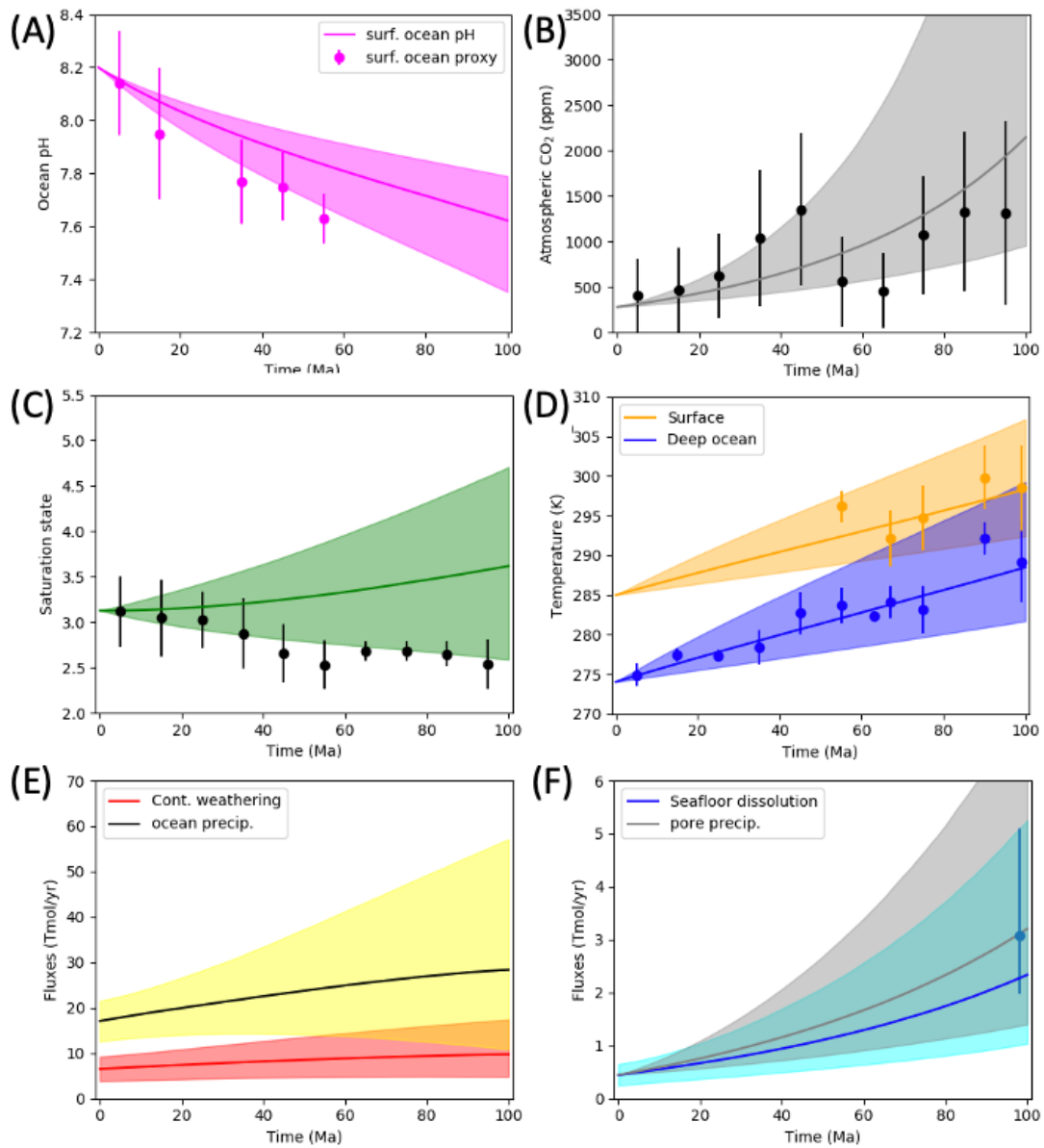


**Fig. 4.4:** Carbon cycle model output for the 2-box K-T&C (2017) “best fit” approximation. Solid lines show the median output, while corresponding shaded areas show 95% confidence interval. Geochemical proxy data and error bars indicated by dots. Panels denote (A) surface ocean pH, (B), atmospheric CO<sub>2</sub> (ppm), (C) carbonate saturation state, (D) surface and deep ocean temperatures (Kelvin), (E) continental silicate weathering and ocean carbonate precipitation fluxes (Tmol/year), and (F) seafloor dissolution and precipitation of carbonate (Tmol/year).

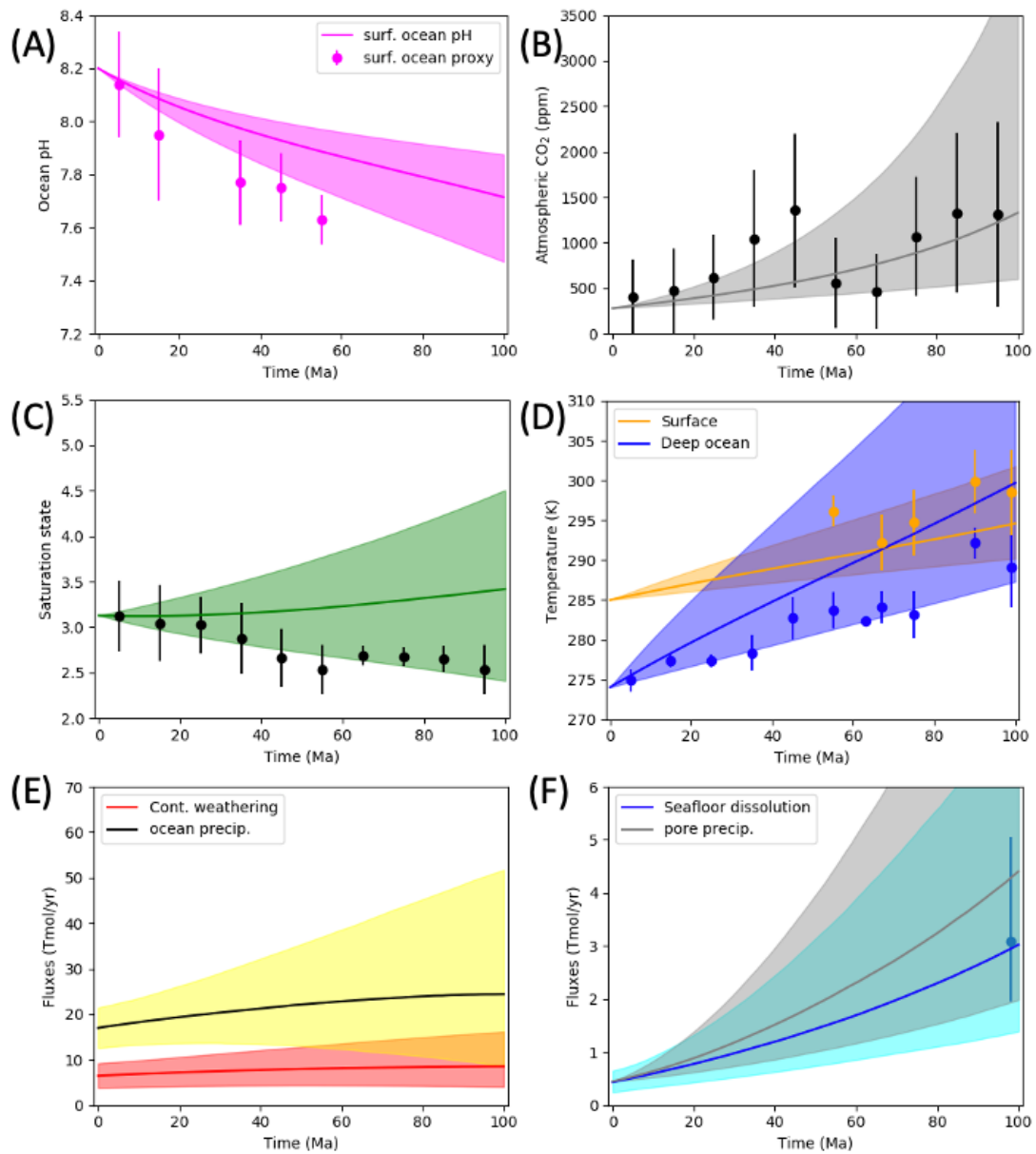


**Fig. 4.5:** Carbon cycle model output for our 3-box “best fit” model. Solid lines show the median output, while corresponding shaded areas show 95% confidence interval. Geochemical proxy data and error bars indicated by dots. Panels denote (A) surface ocean pH, (B), atmospheric CO<sub>2</sub> (ppm), (C) carbonate saturation state, (D) surface and deep ocean temperatures (Kelvin), (E) continental silicate weathering and ocean carbonate precipitation fluxes (Tmol/year), and (F) seafloor dissolution and precipitation of carbonate (Tmol/year).

## **4. Discussion**

### **4.1. Marine controls on C cycling**

Most models of the carbonate-silicate cycle and its effect on climate have focused on continental weathering as the primary means by which atmospheric CO<sub>2</sub> is lost. K-T&C (2017) included seafloor weathering in their model, arguing that this low-temperature CO<sub>2</sub> sink would have played an important role in warm climate episodes in Earth's past. Our model results support this hypothesis and suggest that ocean temperatures do play a major role in marine carbonate preservation, both on the shallow shelves and in the deep ocean. The importance of deep ocean temperatures to the C cycle is in large part because of its influence on seafloor weathering and carbonate precipitation. The climate during the mid-Cretaceous, ~100 Ma, was one of the warmest periods in the Phanerozoic, as we discussed in Chapter 3. Given that seafloor weathering occurs in off-axis hydrothermal vent systems and that it depends on deep ocean temperatures (Coogan & Gillis, 2013), it stands to reason that this process could have been even more important 100 million years ago. During periods like the Cretaceous when surface temperatures (especially at the poles, where warming is amplified by positive feedbacks like the ice albedo feedback) were much higher, deepwater formed at the poles would have likely seen a significant increase in temperature. It is, therefore, important to not only include seafloor weathering but to also give full consideration to the controls on deep sea temperatures.

Our box model results indicate that the deep ocean would likely have been at least 10 K warmer at 100 Ma than in the modern ocean. As a result, both precipitation and dissolution of seafloor carbonates would have been significantly faster, as reaction rates were elevated by higher temperatures. Due to the strong dependence of seafloor weathering rates on deep ocean temperatures, it is critical that the controls on ocean temperature are

modeled carefully. As our simulations suggest, surface warming by atmospheric CO<sub>2</sub> and the strength of the surface-deep ocean temperature gradient dictate the magnitude of seafloor weathering and deposition. Underestimating the temperature of deepwater underestimates the capacity of the seafloor CO<sub>2</sub> sink.

It is also possible that warmer deep ocean temperatures could have powered additional C sinks in the distant past. Isson & Planavsky (2018) argue that there may have been an additional flux of CO<sub>2</sub> from the seafloor via reverse weathering during the Proterozoic (2,500 – 541 Ma). In this process, excess silica in the oceans can form authigenic phyllosilicate clays with available cations within seafloor pore space. This reaction consumes carbonates to form these clays, releasing CO<sub>2</sub> back into the deep ocean. This back-reaction, buffered by deep ocean pH, could have counteracted some of the drawdown by seafloor weathering. However, reverse weathering would likely only have made a difference before the rise of siliceous marine life—such as diatoms and some sponges—which rapidly consume excess silica to form shells (Isson & Planavsky, 2018). During the Proterozoic, considerable amounts of dissolved silica should have been available for clay formation, as it was not being utilized on a grand scale by complex shelly organisms. The earliest of these siliceous organisms evolved around the start of the Phanerozoic, at ~540 Ma (Li et al., 1998), after which time reverse weathering would have a negligible impact on ocean CO<sub>2</sub> fluxes as the needed silica for clay formation was no longer available due to widespread biological use. So, while we do not consider reverse weathering in our analysis here, it may be an important process for pre-Phanerozoic models of the C cycle.

## 4.2. The role of continental processes in the Phanerozoic C cycle

Ocean temperatures and the effect on seafloor weathering are essential for C cycle modeling, but continental weathering arguably remains the dominant control on atmospheric CO<sub>2</sub>. Silicate weathering drives much of the change over time in the projections by K-T&C (2017), with lower relative weatherability and a weak temperature dependence causing the high atmospheric CO<sub>2</sub> (and resulting hot climate) at 100 Ma.

Similar to the result of K-T&C, our best-fit estimate of the approximate  $E_A$  for continental weathering is considerably lower than previous estimates. As we mention in Section 2, Walker et al. (1981) included a temperature dependence with an  $E_A$  equivalent to ~50 kJ/mol, while GEOCARB (Berner, 2006; Berner, 2008) utilized an  $E_A$  of ~75 kJ/mol. Our estimate of  $29_{-8}^{+8}$  kJ/mol is much lower, but is not as low as the estimate from K-T&C (~21 kJ/mol). This difference is likely due to the fact that the K-T&C model underestimated the CO<sub>2</sub> sink from seafloor weathering by neglecting polar amplification of deep ocean temperature. The much larger differences in  $E_A$  between our estimate and those of Walker et al. and Berner may be because neither of their C cycle models included seafloor weathering, and instead focused solely on carbonate-silicate weathering on the continents as atmospheric CO<sub>2</sub> drivers.

A bigger question may be how and why continental weatherability would have been lower at 100 Ma compared to today. K-T&C (2017) offered a number of potential mechanisms for changes in the continent's weatherability in their study, but ultimately did not have a clear explanation for the increase over the last 100 Ma that their statistical analysis implied. The feedback between silicate weathering and surface temperature must

be negative over long scales to keep Earth's climate stable—but the processes influencing the strength of that climate feedback can vary with time and are not fully understood.

Numerous hypotheses have been proposed for why continental weatherability might have increased since the Cretaceous, and during the Cenozoic (~65 Ma to present) in particular. Most of these argue that changes in geography and tectonic processes are the primary mechanisms. For example, the BLAG model estimated continental land area at 100 Ma was only ~80% that of today (Berner et al., 1983), indicating a higher sea level in the past. K-T&C likewise assume a higher sea level at 100 Ma in their discussion of changes to continental weatherability, and point out that studies of ocean basin dynamics (like those of Müller et al., 2008) suggest that sea level then was at least 80 m higher. The exposure of more continent surface area since the Cretaceous could drive a significant fraction of the rise in weatherability, as more land area was exposed to be weathered. But, as K-T&C point out based on their statistical analysis, sea level alone cannot explain the full change. Raymo & Ruddiman (1992) proposed that the uplift of the Himalayas starting at ~50 Ma accelerated silicate weathering fluxes, based partly on rapid episodic increase in marine Sr isotopes. However, Kump & Arthur (1997) pointed out that this was contradicted by concurrent C isotopes; they modified this hypothesis with a geochemical model and proposed that the continent collision that uplifted the Himalayas (~50 Ma to today) increased continental weatherability rather than weathering fluxes. Later studies have largely supported this idea and built off of it (Kump et al., 2000). For instance, Maher & Chamberlain (2014) showed that high topography and new rock can increase weatherability, and Caves et al. (2016) suggested changing continental lithologies as the result of uplift could be responsible for shifts in weatherability.

A more recent analysis by MacDonald et al. (2019) suggested that the main control on continental weatherability is low-latitude arc volcanism and associated tectonic activity. MacDonald et al. cite the emergence of the islands of Indonesia (~20 Ma to today) as the chief mechanism driving Cenozoic cooling. In this hypothesis, low-latitude arc-continent collisions create new mafic and ultramafic rock, which is highly reactive due to its abundant cation content. These newly exposed volcanic rocks are rapidly weathered in the tropics where warm temperatures and high annual rainfall accelerate mechanical and chemical weathering. MacDonald et al. argue that episodes of tropical arc-continent collisions throughout the last 100 Ma (namely the formation of Indonesian islands and uplift of the Himalayas) could have triggered the observed increase in weatherability and associated cooling of global climate in the recent Cenozoic. They also argue that previous arc-continent collisions may have triggered earlier Phanerozoic glaciations. For example, they suggest that the glaciation in the late Ordovician period was caused by the Taconic orogeny. Likewise, the major Permian-Carboniferous glaciation was, they argue, the result of high continental weathering when the Laurasia and Gondwana supercontinents collided during the formation of Pangea and subsequent uplift of the Allegheny and Appalachian Mountains. Both the Taconic and Allegheny-Appalachian mountain-building events were continent collisions that occurred largely in the tropics, between 30°N and 30°S latitude, where high annual precipitation and warm mean temperatures would facilitate accelerated rates of silicate weathering.

If MacDonald et al. are correct, it is possible that tectonic activity in the tropics—along with changes in sea level—caused the increase in weatherability indicated by K-T&C and our own model calculations. Generating new and highly weatherable continental

area could at least partially explain the observed shift. This mechanism for changing weatherability, in conjunction with the temperature-dependent balance between continental and seafloor weathering, could explain the long-term shifts we see in global climate during the last 100 Ma.

## **5. Conclusions**

To more fully solve this problem, it would be necessary to add even greater resolution to our parameterization of surface-deep ocean gradients (like pH and temperature) and to constrain our model output with an inverse MCMC analysis. But the work we present in this chapter offers an in-depth look at the processes controlling Phanerozoic climate, illustrating the complex balance between C sinks and sources that must be considered when modeling the Earth system. We agree with K-T&C (2017) that continental weathering is not as strongly temperature-dependent as earlier models like GEOCARB (Berner, 2008) have suggested, and an increase in continental weatherability over the last 100 Ma is needed to explain long-term trends in the global C cycle. However, we find that seafloor weathering is highly temperature-dependent, and continental weathering is somewhat more so than K-T&C suggested. A Bayesian analysis using our 3-box model would more quantitatively assess that difference, but the analysis we present in this chapter offers a qualitative look at climate change in the last 100 Ma, and emphasizes the particular importance and complexity of the marine component of the C cycle. Ultimately, global C cycling is controlled by the strength of both continental and seafloor weathering, the balance between both C sinks, atmosphere and ocean temperatures, and the release of atmospheric CO<sub>2</sub> by volcanoes. In addition, we agree with recent studies positing that tectonic processes such as tropical arc-continent collisions and sea level fall can

account for much of the increase in weatherability over the last 100 Ma that has caused atmospheric CO<sub>2</sub> to become lower and surface temperatures to decline.

## **Chapter 5.**

### **Concluding Remarks**

Studying the history of CO<sub>2</sub> and O<sub>2</sub> in Earth's atmosphere shows us a complex story spanning billions of years of change, with many major shifts in composition driven by evolving life in the oceans and on land. These changes in the atmosphere have dictated long-term changes in climate throughout Earth's history, and so it becomes essential to study both climate and atmospheric chemistry together to create a complete picture. This, in turn, requires utilizing a diverse array of techniques, tools, and data.

In Chapter 2, we explored a new potential proxy for CO<sub>2</sub> in the Archean atmosphere, at ~2.7 Ga. Using compositional analysis of ancient iron micrometeorites, we calculated the amount of oxidants needed to have oxidized the micrometeorites as they passed through Earth's atmosphere billions of years ago during entry. From that, we estimated that the Archean atmosphere likely contained a high abundance of CO<sub>2</sub>, which both oxidized the micrometeorites and kept the early Earth warm. We also theorized that lower pN<sub>2</sub> in the past may have been likely to explain both the oxidized micrometeorites and evidence for glaciation in the late Archean. The work in this chapter points to new directions for future study, including honing data for CO<sub>2</sub> and iron oxidation reactions, further investigation on long-term changes in atmospheric N<sub>2</sub>, and applying this possible new proxy to other periods in Earth history (following future micrometeorite collection and analysis).

In Chapters 3 and 4, we moved forward in time, focusing on atmospheric evolution after oxygen rose to prominence in the Earth's atmosphere. In Chapter 3, we focused on a

specific period of climate history at ~100 Ma and conduct an in-depth study of the effect of O<sub>2</sub> on surface temperature and the greenhouse effect during the Cretaceous. Our findings indicated that O<sub>2</sub> accentuates the effectiveness of greenhouse gases like CO<sub>2</sub>, and support the longstanding paradigm that CO<sub>2</sub>, weathering, and geography are the dominant controls on Phanerozoic climate.

In Chapter 4, we broadened our lens to consider long-term climate change, with consideration to global carbon cycling since the Cretaceous. We revisited earlier models of CO<sub>2</sub> and the carbon cycle over the last ~100 Ma and expanded on recent modeling efforts to create a realistic box model of continental and marine influences on global carbon. We found that continental weathering—and specifically, changes in continental weatherability due to tectonics and uplift—have driven much of the CO<sub>2</sub> evolution since the Cretaceous; this is supplemented by highly temperature-dependent seafloor weathering. Future work in this area will include continuing to develop the model used in Chapter 4, and expanding it to examine the whole Phanerozoic. Future work will include adding more adjustable parameters to the model and including additional proxy data for comparison with the model.

Overall, these three chapters examine problems in Earth's atmospheric history in three different ways. This work emphasizes the importance of geochemical data and modeling in studying climate change, past and present, and utilizes a variety of tools to do so. Ultimately, this research and future work on these topics illustrate that there are still a number of fascinating questions about Earth's climate evolution, waiting to be explored.

## Bibliography

- Abuluwefa. (1997). Oxidation of low carbon steel in multicomponent gases. Part 1: Reaction mechanisms during isothermal oxidation. <https://doi.org/10.1007/s11661-997-0255-7>
- Akhmadov, U. S., Zaslanko, I. S., & Smirnov, V. N. (1988). Mechanism and kinetics of interaction of Fe, Cr, Mo, and Mn atoms with molecular oxygen. Retrieved from <https://www.osti.gov/biblio/6289832>
- Anagnostou, E., John, E. H., Edgar, K. M., Foster, G. L., Ridgwell, A., Inglis, G. N., et al. (2016). Changing atmospheric CO<sub>2</sub> concentration was the primary driver of early Cenozoic climate. *Nature*, 533(7603), 380–384. <https://doi.org/10.1038/nature17423>
- Archibald, J. D. (1996). Fossil Evidence for a Late Cretaceous Origin of “Hoofed” Mammals. *Science*, 272(5265), 1150 LP – 1153. <https://doi.org/10.1126/science.272.5265.1150>
- Arvidson, R. S., Mackenzie, F. T., & Guidry, M. W. (2013). Geologic history of seawater: A MAGic approach to carbon chemistry and ocean ventilation. *Chemical Geology*, 362, 287–304. <https://doi.org/https://doi.org/10.1016/j.chemgeo.2013.10.012>
- Avice, G., Marty, B., Burgess, R., Hofmann, A., Philippot, P., Zahnle, K., & Zakharov, D. (2018). Evolution of atmospheric xenon and other noble gases inferred from Archean to Paleoproterozoic rocks. *Geochimica et Cosmochimica Acta*, 232, 82–100. <https://doi.org/https://doi.org/10.1016/j.gca.2018.04.018>
- Banks, & Kockarts. (1973). *Aeronomy, Part B*. Academic Press.
- Berling. (2017). *The Emerald Planet*. Oxford University Press.
- Bekker, A., Kaufman, A. J., Karhu, J. A., & Eriksson, K. A. (2005). Evidence for Paleoproterozoic cap carbonates in North America. *Precambrian Research*, 137(3), 167–206. <https://doi.org/https://doi.org/10.1016/j.precamres.2005.03.009>
- Bergman, N. M., Lenton, T. M., & Watson, A. J. (2004). COPSE: A new model of biogeochemical cycling over phanerozoic time. *American Journal of Science*, 304(5), 397–437. <https://doi.org/10.2475/ajs.304.5.397>
- Berner, & Canfield. (1989). A new model for atmospheric oxygen over Phanerozoic time. *American Journal of Science*, 289(4), 333–361.
- Berner, R. A., Lasaga, A. C., & Garrels, R. M. (1983). The carbonate-silicate geochemical cycle and its effect on atmospheric carbon dioxide over the past 100 million years. *American Journal of Science*. <https://doi.org/10.2475/ajs.283.7.641>
- Berner, R A, Petsch, S. T., Lake, J. A., Beerling, D. J., Popp, B. N., Lane, R. S., et al.

- (2000). Isotope Fractionation and Atmospheric Oxygen: Implications for Phanerozoic O<sub>2</sub> Evolution. *Science*, 287(5458), 1630 LP – 1633. <https://doi.org/10.1126/science.287.5458.1630>
- Berner, Robert A. (2006). GEOCARBSULF: A combined model for Phanerozoic atmospheric O<sub>2</sub> and CO<sub>2</sub>. *Geochimica et Cosmochimica Acta*, 70(23 SPEC. ISS.), 5653–5664. <https://doi.org/10.1016/j.gca.2005.11.032>
- Berner, Robert A. (2006). Inclusion of the Weathering of Volcanic Rocks in the GEOCARBSULF Model. *American Journal of Science*, 306(5), 295–302. <https://doi.org/10.2475/05.2006.01>
- Berner, Robert A. (2009). Phanerozoic atmospheric oxygen: New results using the GEOCARBSULF model. *American Journal of Science*, 309(7), 603–606. <https://doi.org/10.2475/07.2009.03>
- Berner, Robert A., & Kothavala, Z. (2001). Geocarb III: A Revised Model of Atmospheric CO<sub>2</sub> over Phanerozoic Time. *American Journal of Science*, 301(2), 182–204. <https://doi.org/10.2475/ajs.301.2.182>
- Bice, K. L., Birgel, D., Meyers, P. A., Dahl, K. A., Hinrichs, K.-U., & Norris, R. D. (2006). A multiple proxy and model study of Cretaceous upper ocean temperatures and atmospheric CO<sub>2</sub> concentrations. *Paleoceanography*, 21(2). <https://doi.org/10.1029/2005PA001203>
- Bredesen, R., & Kofstad, P. (1991). On the oxidation of iron in CO<sub>2</sub>+CO mixtures: II. Reaction mechanisms during initial oxidation. *Oxidation of Metals*, 35(1), 107–137. <https://doi.org/10.1007/BF00666503>
- Caldeira, K. (1995). Long-term control of atmospheric carbon dioxide; low-temperature seafloor alteration or terrestrial silicate-rock weathering? *American Journal of Science*, 295(9), 1077–1114. Retrieved from <http://www.ajsonline.org/content/295/9/1077.short>
- Catling, & Kasting. (2017). *Atmospheric Evolution on Inhabited and Lifeless Worlds*. Cambridge University Press.
- Caves, J. K., Jost, A. B., Lau, K. V., & Maher, K. (2016). Cenozoic carbon cycle imbalances and a variable weathering feedback. *Earth and Planetary Science Letters*, 450, 152–163. <https://doi.org/10.1016/j.epsl.2016.06.035>
- Chapman, & Cowling. (1939). *The mathematical theory of non-uniform gases: an account of the kinetic theory of viscosity, thermal conduction and diffusion in gases*. University Press.
- Chapman, Cowling, & Burnett. (1990). *The mathematical theory of non-uniform gases: an account of the kinetic theory of viscosity, thermal conduction and diffusion in gases*. Cambridge University Press.

- Charney, E., Lee, C.-H., & Rosenfield, J. S. (1979). Calculations of rotatory strengths in chiral chromophores. Sensitivity to structural parameters in dienes. *Journal of the American Chemical Society*, *101*(23), 6802–6804. <https://doi.org/10.1021/ja00517a002>
- Coogan, L A, & Gillis, K. M. (2018). Temperature dependence of chemical exchange during seafloor weathering: Insights from the Troodos ophiolite. *Geochimica et Cosmochimica Acta*, *243*, 24–41. <https://doi.org/https://doi.org/10.1016/j.gca.2018.09.025>
- Coogan, Laurence A., & Dosso, S. E. (2015). Alteration of ocean crust provides a strong temperature dependent feedback on the geological carbon cycle and is a primary driver of the Sr-isotopic composition of seawater. *Earth and Planetary Science Letters*, *415*, 38–46. <https://doi.org/10.1016/j.epsl.2015.01.027>
- Coogan, Laurence A., & Gillis, K. M. (2013). Evidence that low-temperature oceanic hydrothermal systems play an important role in the silicate-carbonate weathering cycle and long-term climate regulation. *Geochemistry, Geophysics, Geosystems*, *14*(6), 1771–1786. <https://doi.org/10.1002/ggge.20113>
- Driese, S. G., Jirsa, M. A., Ren, M., Brantley, S. L., Sheldon, N. D., Parker, D., & Schmitz, M. (2011). Neoproterozoic paleoweathering of tonalite and metabasalt: Implications for reconstructions of 2.69Ga early terrestrial ecosystems and paleoatmospheric chemistry. *Precambrian Research*, *189*(1), 1–17. <https://doi.org/https://doi.org/10.1016/j.precamres.2011.04.003>
- Falkowski, P. G., Katz, M. E., Milligan, A. J., Fennel, K., Cramer, B. S., Aubry, M. P., et al. (2005). The Rise of Oxygen over the Past 205 Million Years and the Evolution of Large Placental Mammals. *Science*, *309*(5744), 2202 LP – 2204. <https://doi.org/10.1126/science.1116047>
- Farquar, Bao, & Thiemens. (2000). Atmospheric Influence of Earth's Earliest Sulfur Cycle. *Science*, *289*(5480), 756–758.
- Friedrich, O., Norris, R. D., & Erbacher, J. (2012). Evolution of middle to Late Cretaceous oceans—A 55 m.y. record of Earth's temperature and carbon cycle. *Geology*, *40*(2), 107–110. <https://doi.org/10.1130/G32701.1>
- Giesen, A., Herzler, J., & Roth, P. (2002). High temperature oxidation of iron atoms by CO<sub>2</sub>. *Physical Chemistry Chemical Physics*, *4*(15), 3665–3668. <https://doi.org/10.1039/B201822E>
- Goldblatt, Claire, Lenton, Matthews, Watson, & Zahnle. (2009a). Nitrogen-enhanced greenhouse warming on early Earth. *Nature Geoscience*, *2*.
- Goldblatt, C. (2016). Comment on “Long-term climate forcing by atmospheric oxygen concentrations.” *Science*, *353*(6295), 132 LP – 132. <https://doi.org/10.1126/science.aad6976>

- Goldblatt, C., Claire, M. W., Lenton, T. M., Matthews, A. J., Watson, A. J., & Zahnle, K. J. (2009b). Nitrogen-enhanced greenhouse warming on early Earth. *Nature Geoscience*, 2(12), 891–896. <https://doi.org/10.1038/ngeo692>
- Gough, D. O. (1981). Solar Interior Structure and Luminosity Variations BT - Physics of Solar Variations. In V. Domingo (Ed.) (pp. 21–34). Dordrecht: Springer Netherlands.
- Haqq-Misra, J. D., Domagal-Goldman, S. D., Kasting, P. J., & Kasting, J. F. (2008). A revised, hazy methane greenhouse for the Archean Earth. *Astrobiology*, 8(6), 1127–1137. <https://doi.org/10.1089/ast.2007.0197>
- Harman, Schwieterman, Schottkotte, & Kasting. (2015). Abiotic O<sub>2</sub> levels on planets around F, G, K, and M stars: possible false positives for life? *The Astrophysical Journal*, 812(2).
- Harman, C. E., Pavlov, A. A., Babikov, D., & Kasting, J. F. (2018). Chain formation as a mechanism for mass-independent fractionation of sulfur isotopes in the Archean atmosphere. *Earth and Planetary Science Letters*, 496, 238–247. <https://doi.org/10.1016/j.epsl.2018.05.041>
- Hetherington, A. J., & Dolan, L. (2019). Rhynie chert fossils demonstrate the independent origin and gradual evolution of lycophyte roots. *Current Opinion in Plant Biology*, 47, 119–126. <https://doi.org/https://doi.org/10.1016/j.pbi.2018.12.001>
- Holland. (1994). Early life on Earth. In *Nobel Symposium, Vol. 4* (pp. 237–244). Columbia University Press.
- Holland. (2006). The oxygenation of the atmosphere and oceans. *Phil. Trans. of the Royal Society – Biological Sciences*, 361, 903–915.
- Holland, M. M., & Bitz, C. M. (2003). Polar amplification of climate change in coupled models. *Climate Dynamics*, 21(3–4), 221–232. <https://doi.org/10.1007/s00382-003-0332-6>
- Intergovernmental Panel on Climate Change (Ed.). (2014). Anthropogenic and Natural Radiative Forcing. In *Climate Change 2013 – The Physical Science Basis: Working Group I Contribution to the Fifth Assessment Report of the Intergovernmental Panel on Climate Change* (pp. 659–740). Cambridge: Cambridge University Press. <https://doi.org/DOI: 10.1017/CBO9781107415324.018>
- Isson, T. T., & Planavsky, N. J. (2018). Reverse weathering as a long-term stabilizer of marine pH and planetary climate. *Nature*, 560(7719), 471–475. <https://doi.org/10.1038/s41586-018-0408-4>
- Kah, L. C., & Riding, R. (2007). Mesoproterozoic carbon dioxide levels inferred from calcified cyanobacteria. *Geology*, 35(9), 799–802. <https://doi.org/10.1130/G23680A.1>

- Kanzaki, Y., & Murakami, T. (2015). Estimates of atmospheric CO<sub>2</sub> in the Neoproterozoic–Paleoproterozoic from paleosols. *Geochimica et Cosmochimica Acta*, *159*, 190–219. <https://doi.org/https://doi.org/10.1016/j.gca.2015.03.011>
- Kasting. (2014). Atmospheric composition of Hadean–early Archean Earth: The importance of CO. *Geological Society of America Special Papers*, *504*, 19–28.
- Kasting, J.F. (2010). Faint young sun redux. *Nature*, *464*, 687–689.
- Kasting, J.F. (1993). Earth's early atmosphere. *Science*, *259*(5097), 920 LP – 926. <https://doi.org/10.1126/science.11536547>
- Kasting, James F. (1984). The evolution of the prebiotic atmosphere. *Origins of Life*, *14*, 75–82.
- Kasting, James F. (1987). Theoretical constraints on oxygen and carbon dioxide concentrations in the Precambrian atmosphere. *Precambrian Research*, *34*(3), 205–229. [https://doi.org/https://doi.org/10.1016/0301-9268\(87\)90001-5](https://doi.org/https://doi.org/10.1016/0301-9268(87)90001-5)
- Kharecha, P., Kasting, & Siefert. (2005). A coupled atmosphere–ecosystem model of the early Archean Earth. *Geobiology*, *3*(2), 53–76. <https://doi.org/10.1111/j.1472-4669.2005.00049.x>
- Kidston, R., & Lang, W. H. (1921). XXXIII.—On Old Red Sandstone Plants showing Structure, from the Rhynie Chert Bed, Aberdeenshire. Part V. The Thallophyta occurring in the Peat-Bed; the Succession of the Plants throughout a Vertical Section of the Bed, and the Conditions of Accumulation a. *Transactions of the Royal Society of Edinburgh*, *52*(4), 855–902. <https://doi.org/DOI:10.1017/S0080456800016045>
- Kiehl, J. T., Hack, J. J., Bonan, G. B., Boville, B. A., Williamson, D. L., & Rasch, P. J. (1998). The National Center for Atmospheric Research Community Climate Model: CCM3\*. *Journal of Climate*, *11*(6), 1131–1149. [https://doi.org/10.1175/1520-0442\(1998\)011<1131:TNCFAR>2.0.CO;2](https://doi.org/10.1175/1520-0442(1998)011<1131:TNCFAR>2.0.CO;2)
- Kirschvink, J. L., Gaidos, E. J., Bertani, L. E., Beukes, N. J., Gutzmer, J., Maepa, L. N., & Steinberger, R. E. (2000). Paleoproterozoic snowball Earth: Extreme climatic and geochemical global change and its biological consequences. *Proceedings of the National Academy of Sciences*, *97*(4), 1400 LP – 1405. <https://doi.org/10.1073/pnas.97.4.1400>
- Knutti, R., Rugenstein, M. A. A., & Hegerl, G. C. (2017). Beyond equilibrium climate sensitivity. *Nature Geoscience*, *10*(10), 727–736. <https://doi.org/10.1038/ngeo3017>
- Kopp, R. E., Kirschvink, J. L., Hilburn, I. A., & Nash, C. Z. (2005). The Paleoproterozoic snowball Earth: A climate disaster triggered by the evolution of oxygenic photosynthesis. *Proceedings of the National Academy of Sciences of the United States of America*, *102*(32), 11131 LP – 11136. <https://doi.org/10.1073/pnas.0504878102>

- Krissansen-Totton, J., & Catling, D. C. (2017). Constraining climate sensitivity and continental versus seafloor weathering using an inverse geological carbon cycle model. *Nature Communications*, 8(May), 1–15. <https://doi.org/10.1038/ncomms15423>
- Kuhn, W. R., & Atreya, S. K. (1979). Ammonia photolysis and the greenhouse effect in the primordial atmosphere of the earth. *Icarus*, 37(1), 207–213. [https://doi.org/https://doi.org/10.1016/0019-1035\(79\)90126-X](https://doi.org/https://doi.org/10.1016/0019-1035(79)90126-X)
- Kump, & Arthur. (1997). Global Chemical Erosion during the Cenozoic: Weatherability Balances the Budgets. In *Tectonic Uplift and Climate Change* (pp. 399–426). Springer.
- Kump, Kasting, & Crane. (2010). *The Earth System* (3rd ed.). Pearson.
- Kump, L. R., Brantley, S. L., & Arthur, M. A. (2000). Chemical Weathering, Atmospheric CO<sub>2</sub>, and Climate. *Annual Review of Earth and Planetary Sciences*, 28(1), 611–667. <https://doi.org/10.1146/annurev.earth.28.1.611>
- Lambertz, M., Bertozzo, F., & Sander, P. M. (2018). Bone histological correlates for air sacs and their implications for understanding the origin of the dinosaurian respiratory system. *Biology Letters*, 14(1), 20170514. <https://doi.org/10.1098/rsbl.2017.0514>
- Lehmer, O. R., Catling, D. C., Buick, R., Brownlee, D. E., & Newport, S. (2020). Atmospheric CO<sub>2</sub> levels from 2.7 billion years ago inferred from micrometeorite oxidation. *Science Advances*, 6(4), eaay4644. <https://doi.org/10.1126/sciadv.aay4644>
- Lenton, T. M., Daines, S. J., & Mills, B. J. W. (2018). COPSE reloaded: An improved model of biogeochemical cycling over Phanerozoic time. *Earth-Science Reviews*, 178(August 2017), 1–28. <https://doi.org/10.1016/j.earscirev.2017.12.004>
- Li, C.-W., Chen, J.-Y., & Hua, T.-E. (1998). Precambrian Sponges with Cellular Structures. *Science*, 279(5352), 879 LP – 882. <https://doi.org/10.1126/science.279.5352.879>
- Li, K.-F., Pahlevan, K., Kirschvink, J. L., & Yung, Y. L. (2009). Atmospheric pressure as a natural climate regulator for a terrestrial planet with a biosphere. *Proceedings of the National Academy of Sciences*, 106(24), 9576 LP – 9579. <https://doi.org/10.1073/pnas.0809436106>
- Love, S. G., & Brownlee, D. E. (1991). Heating and thermal transformation of micrometeoroids entering the Earth's atmosphere. *Icarus*, 89(1), 26–43. [https://doi.org/10.1016/0019-1035\(91\)90085-8](https://doi.org/10.1016/0019-1035(91)90085-8)
- Lyons, S. L., Baczynski, A. A., Babila, T. L., Bralower, T. J., Hajek, E. A., Kump, L. R., et al. (2019). Palaeocene–Eocene Thermal Maximum prolonged by fossil carbon oxidation. *Nature Geoscience*, 12(1), 54–60. <https://doi.org/10.1038/s41561-018->

- Macdonald, F. A., Swanson-Hysell, N. L., Park, Y., Lisiecki, L., & Jagoutz, O. (2019). Arc-continent collisions in the tropics set Earth's climate state. *Science*, *364*(6436), 181 LP – 184. <https://doi.org/10.1126/science.aav5300>
- Maher, K., & Chamberlain, C. P. (2014). Hydrologic Regulation of Chemical Weathering and the Geologic Carbon Cycle. *Science*, *343*(6178), 1502 LP – 1504. <https://doi.org/10.1126/science.1250770>
- Manabe, S., & Wetherald, R. T. (1967). Thermal Equilibrium of the Atmosphere with a Given Distribution of Relative Humidity. *Journal of the Atmospheric Sciences*, *24*(3), 241–259. [https://doi.org/10.1175/1520-0469\(1967\)024<0241:TEOTAW>2.0.CO;2](https://doi.org/10.1175/1520-0469(1967)024<0241:TEOTAW>2.0.CO;2)
- Marty, B., Zimmermann, L., Pujol, M., Burgess, R., & Philippot, P. (2013). Nitrogen Isotopic Composition and Density of the Archean Atmosphere. *Science*, *342*(6154), 101 LP – 104. <https://doi.org/10.1126/science.1240971>
- Massie, S. T., & Hunten, D. M. (1981). Stratospheric eddy diffusion coefficients from tracer data. *Journal of Geophysical Research: Oceans*, *86*(C10), 9859–9868. <https://doi.org/10.1029/JC086iC10p09859>
- Mlawer, E. J., Taubman, S. J., Brown, P. D., Iacono, M. J., & Clough, S. A. (1997). Radiative transfer for inhomogeneous atmospheres: RRTM, a validated correlated-k model for the longwave. *Journal of Geophysical Research: Atmospheres*, *102*(D14), 16663–16682. <https://doi.org/10.1029/97JD00237>
- Mojzsis, S. J., Harrison, T. M., & Pidgeon, R. T. (2001). Oxygen-isotope evidence from ancient zircons for liquid water at the Earth's surface 4,300 Myr ago. *Nature*, *409*(6817), 178–181. <https://doi.org/10.1038/35051557>
- Mora, C. I., Driese, S. G., & Seager, P. G. (1991). Carbon dioxide in the Paleozoic atmosphere: evidence from carbon- isotope compositions of pedogenic carbonate. *Geology*, *19*(10), 1017–1020. [https://doi.org/10.1130/0091-7613\(1991\)019<1017:CDITPA>2.3.CO;2](https://doi.org/10.1130/0091-7613(1991)019<1017:CDITPA>2.3.CO;2)
- Müller, R. D., Sdrolias, M., Gaina, C., Steinberger, B., & Heine, C. (2008). Long-Term Sea-Level Fluctuations Driven by Ocean Basin Dynamics. *Science*, *319*(5868), 1357 LP – 1362. <https://doi.org/10.1126/science.1151540>
- Nutman, A. P., Bennett, V. C., Friend, C. R. L., Van Kranendonk, M. J., & Chivas, A. R. (2016). Rapid emergence of life shown by discovery of 3,700-million-year-old microbial structures. *Nature*, *537*(7621), 535–538. <https://doi.org/10.1038/nature19355>
- Ojakangas, Srinivasan, Hegde, Chandrakant, & Srikantia. (2014). The Talya Conglomerate: an Archean (~2.7 Ga) Glaciomarine Formation, Western Dharwar Craton, Southern India. *Current Science*, *106*(3).

- Pavlov, A. A., Brown, L. L., & Kasting, J. F. (2001). UV shielding of NH<sub>3</sub> and O<sub>2</sub> by organic hazes in the Archean atmosphere. *Journal of Geophysical Research*, 106(106), 23267–23287. <https://doi.org/10.1029/2000JE001448>
- Poulsen, C. J., & Zhou, J. (2013). Sensitivity of Arctic Climate Variability to Mean State: Insights from the Cretaceous. *Journal of Climate*, 26(18), 7003–7022. <https://doi.org/10.1175/JCLI-D-12-00825.1>
- Poulsen, C. J., Tabor, C., & White, J. D. (2015). Long-term climate forcing by atmospheric oxygen concentrations. *Science*, 348(6240), 1238 LP – 1241. <https://doi.org/10.1126/science.1260670>
- Quick, D. E., & Ruben, J. A. (2009). Cardio-pulmonary anatomy in theropod dinosaurs: Implications from extant archosaurs. *Journal of Morphology*, 270(10), 1232–1246. <https://doi.org/10.1002/jmor.10752>
- Raymo, M. E., & Ruddiman, W. F. (1992). Tectonic forcing of late Cenozoic climate. *Nature*, 359(6391), 117–122. <https://doi.org/10.1038/359117a0>
- Ribas, I., Guinan, E. F., Gudel, M., & Audard, M. (2005). Evolution of the Solar Activity over Time and Effects on Planetary Atmospheres. I. High-Energy Irradiances (1–1700 Å). *The Astrophysical Journal*, 622(1), 680–694. <https://doi.org/10.1086/427977>
- Rimmer, P. B., Shorttle, O., & Rugheimer, S. (2019). Oxidised micrometeorites as evidence for low atmospheric pressure on the early Earth. *Geochemical Perspectives Letters*, 9, 38–42. <https://doi.org/10.7185/geochemlet.1903>
- Rollason, R. J., & Plane, J. M. C. (2000). The reactions of FeO with O<sub>3</sub>, H<sub>2</sub>, H<sub>2</sub>O, O<sub>2</sub> and CO<sub>2</sub>. *Physical Chemistry Chemical Physics*, 2(10), 2335–2343. <https://doi.org/10.1039/B000877J>
- Rothman, D. H. (2002). Atmospheric carbon dioxide levels for the last 500 million years. *Proceedings of the National Academy of Sciences of the United States of America*, 99(7), 4167–4171. <https://doi.org/10.1073/pnas.022055499>
- Royer, D. L. (2013). *Atmospheric CO<sub>2</sub> and O<sub>2</sub> During the Phanerozoic: Tools, Patterns, and Impacts*. *Treatise on Geochemistry: Second Edition* (2nd ed., Vol. 6). Elsevier Ltd. <https://doi.org/10.1016/B978-0-08-095975-7.01311-5>
- ROYER, D. L., & HREN, M. T. (2017). CARBON ISOTOPIC FRACTIONATION BETWEEN WHOLE LEAVES AND CUTICLE. *PALAIOS*, 32(4), 199–205. <https://doi.org/10.2110/palo.2016.073>
- Royer, Dana L, Donnadieu, Y., Park, J., Kowalczyk, J., & Godd eris, Y. (2014). Error analysis of CO<sub>2</sub> and O<sub>2</sub> estimates from the long-term geochemical model GEOCARBSULF. *American Journal of Science*, 314(9), 1259–1283. Retrieved from <http://www.ajsonline.org/content/314/9/1259.abstract>

- Sagan, C., & Mullen, G. (1972). Earth and Mars: Evolution of Atmospheres and Surface Temperatures. *Science*, 177(4043), 52 LP – 56. <https://doi.org/10.1126/science.177.4043.52>
- Saltzman, M. R., & Edwards, C. T. (2017). Gradients in the carbon isotopic composition of Ordovician shallow water carbonates: A potential pitfall in estimates of ancient CO<sub>2</sub> and O<sub>2</sub>. *Earth and Planetary Science Letters*, 464, 46–54. <https://doi.org/10.1016/j.epsl.2017.02.011>
- Sander, P. M., Christian, A., Clauss, M., Fehner, R., Gee, C. T., Griebeler, E.-M., et al. (2011). Biology of the sauropod dinosaurs: the evolution of gigantism. *Biological Reviews of the Cambridge Philosophical Society*, 86(1), 117–155. <https://doi.org/10.1111/j.1469-185X.2010.00137.x>
- Scott, A. C., & Glasspool, I. J. (2006). The diversification of Paleozoic fire systems and fluctuations in atmospheric oxygen concentration. *Proceedings of the National Academy of Sciences of the United States of America*, 103(29), 10861–10865. <https://doi.org/10.1073/pnas.0604090103>
- Segura, A., Krelove, K., Kasting, J. F., Sommerlatt, D., Meadows, V., Crisp, D., et al. (2003a). Ozone concentrations and ultraviolet fluxes on earth-like planets around other stars. *Astrobiology*, 3(4), 689–708. <https://doi.org/10.1089/153110703322736024>
- Segura, A., Krelove, K., Kasting, J. F., Sommerlatt, D., Meadows, V., Crisp, D., et al. (2003b). Ozone Concentrations and Ultraviolet Fluxes on Earth-Like Planets Around Other Stars. *Astrobiology*, 3(4), 689–708. <https://doi.org/10.1089/153110703322736024>
- Self, D. E., & Plane, J. M. C. (2003). A kinetic study of the reactions of iron oxides and hydroxides relevant to the chemistry of iron in the upper mesosphere. *Physical Chemistry Chemical Physics*, 5(7), 1407–1418. <https://doi.org/10.1039/B211900E>
- Smirnov, V. N. (2008). Rate constant of the gas-phase reaction between Fe atoms and CO<sub>2</sub>. *Kinetics and Catalysis*, 49(5), 607–609. <https://doi.org/10.1134/S0023158408050017>
- Smirnov, V. N. (2012). Thermochemical parameters and rate constants of the reactions Fe + O<sub>2</sub> + M ↔ FeO<sub>2</sub> + M and FeO + O<sub>2</sub> ↔ FeO<sub>2</sub> + O. *Kinetics and Catalysis*, 53(5), 543–553. <https://doi.org/10.1134/S0023158412050138>
- Som, S. M., Buick, R., Hagadorn, J. W., Blake, T. S., Perreault, J. M., Harnmeijer, J. P., & Catling, D. C. (2016). Earth's air pressure 2.7 billion years ago constrained to less than half of modern levels. *Nature Geoscience*, 9(6), 448–451. <https://doi.org/10.1038/ngeo2713>
- Stanton, C. L., Reinhard, C. T., Kasting, J. F., Ostrom, N. E., Haslun, J. A., Lyons, T. W., & Glass, J. B. (2018). Nitrous oxide from chemodenitrification: A possible missing link in the Proterozoic greenhouse and the evolution of aerobic respiration.

*Geobiology*, 16(6), 597–609. <https://doi.org/10.1111/gbi.12311>

- Stolper, D. A., Bender, M. L., Dreyfus, G. B., Yan, Y., & Higgins, J. A. (2016). A Pleistocene ice core record of atmospheric O<sub>2</sub> concentrations. *Science*, 353(6306), 1427 LP – 1430. <https://doi.org/10.1126/science.aaf5445>
- Tappert, R., McKellar, R. C., Wolfe, A. P., Tappert, M. C., Ortega-Blanco, J., & Muehlenbachs, K. (2013). Stable carbon isotopes of C<sub>3</sub> plant resins and ambers record changes in atmospheric oxygen since the Triassic. *Geochimica et Cosmochimica Acta*, 121, 240–262. <https://doi.org/https://doi.org/10.1016/j.gca.2013.07.011>
- Tomkins, A. G., Bowlt, L., Genge, M., Wilson, S. A., Brand, H. E. A., & Wykes, J. L. (2016). Ancient micrometeorites suggestive of an oxygen-rich Archaean upper atmosphere. *Nature*, 533, 235–238. <https://doi.org/10.1038/nature17678>
- Toon, O. B., McKay, C. P., Ackerman, T. P., & Santhanam, K. (1989). Rapid calculation of radiative heating rates and photodissociation rates in inhomogeneous multiple scattering atmospheres. *Journal of Geophysical Research: Atmospheres*, 94(D13), 16287–16301. <https://doi.org/10.1029/JD094iD13p16287>
- Velbel, M. A. (1993). Temperature dependence of silicate weathering in nature: How strong a negative feedback on long-term accumulation of atmospheric CO<sub>2</sub> and global greenhouse warming? *Geology*, 21(12), 1059–1062. [https://doi.org/10.1130/0091-7613\(1993\)021<1059:TDOSWI>2.3.CO;2](https://doi.org/10.1130/0091-7613(1993)021<1059:TDOSWI>2.3.CO;2)
- Volk. (1987). Feedbacks between weathering and atmospheric CO<sub>2</sub> over the last 100 million years. *American Journal of Science*, 287(8), 763–779.
- Wade, D. C., Abraham, N. L., Farnsworth, A., Valdes, P. J., Bragg, F., & Archibald, A. T. (2019). Simulating the climate response to atmospheric oxygen variability in the Phanerozoic: a focus on the Holocene, Cretaceous and Permian. *Climate of the Past*, 15(4), 1463–1483. <https://doi.org/http://dx.doi.org/10.5194/cp-15-1463-2019>
- Walker. (1993). Biogeochemical Cycles of Carbon on a Hierarchy of Time Scales. In *Biogeochemistry of Global Change* (pp. 3–28).
- Walker, J. C. G., Hays, P. B., & Kasting, J. F. (1981). A negative feedback mechanism for the long-term stabilization of Earth's surface temperature. *Journal of Geophysical Research: Oceans*, 86(C10), 9776–9782. <https://doi.org/10.1029/JC086iC10p09776>
- West, A. J., Galy, A., & Bickle, M. (2005). Tectonic and climatic controls on silicate weathering. *Earth and Planetary Science Letters*, 235(1), 211–228. <https://doi.org/https://doi.org/10.1016/j.epsl.2005.03.020>
- Wilde, S. A., Valley, J. W., Peck, W. H., & Graham, C. M. (2001). Evidence from detrital zircons for the existence of continental crust and oceans on the Earth 4.4 Gyr ago. *Nature*, 409(6817), 175–178. <https://doi.org/10.1038/35051550>

- Wordsworth, R., & Pierrehumbert, R. (2013). Hydrogen-Nitrogen Greenhouse Warming in Earth's Early Atmosphere. *Science*, 339(6115), 64 LP – 67. <https://doi.org/10.1126/science.1225759>
- Young, G. M., Brunn, V. von, Gold, D. J. C., & Minter, W. E. L. (1998). Earth's Oldest Reported Glaciation: Physical and Chemical Evidence from the Archean Mozaan Group (~2.9 Ga) of South Africa. *The Journal of Geology*, 106(5), 523–538. <https://doi.org/10.1086/516039>
- Zahnle, K., Claire, M., & Catling, D. (2006). The loss of mass-independent fractionation in sulfur due to a Palaeoproterozoic collapse of atmospheric methane. *Geobiology*, 4(4), 271–283. <https://doi.org/10.1111/j.1472-4669.2006.00085.x>
- Zahnle, K. J. (1986). Photochemistry of methane and the formation of hydrocyanic acid (HCN) in the Earth's early atmosphere. *Journal of Geophysical Research: Atmospheres*, 91(D2), 2819–2834. <https://doi.org/10.1029/JD091iD02p02819>
- Zahnle, Kevin, & Buick, R. (2016). Ancient air caught by shooting stars. *Nature*, 533(7602), 184–186. <https://doi.org/10.1038/533184a>

**Vita**  
**Rebecca C. Payne**

**Education**

Dual-title PhD, *Geosciences and Astrobiology* Anticipated graduation: Dec 2020  
Penn State University, University Park, PA  
Bachelor of Sciences, *Geological Sciences* May 2015  
Brown University, Providence, RI

**Publications**

**Payne**, Brownlee, & Kasting (2020): “Oxidized micrometeorites suggest either high pCO<sub>2</sub> or low pN<sub>2</sub> during the Neoproterozoic”. *PNAS*.  
Hayworth, Kopparapu, Haqq-Misra, Batalha, **Payne**, Foley, Ikwut-Ukwa, & Kasting (2020): “Warming early Mars with climate cycling: the effect of CO<sub>2</sub>-H<sub>2</sub> collision-induced absorption”. *Icarus*.  
**Payne**, Britt, Chen, Kasting, & Catling (2016): “The response of Phanerozoic surface temperature to variations in atmospheric oxygen concentration”. *JGR: Atmospheres*, 121.

**Research Experience**

Doctoral Research, Penn State University 2015–2020  
*Research Advisor*: James F. Kasting. Penn State University  
*Dissertation*: Select problems in the evolution of Earth’s atmosphere and climate  
Undergraduate Research, Brown University 2014–2015  
*Research Advisor*: Jung-Eun Lee, Brown University  
*Thesis*: Precipitation Seasonality in Extreme Climates Using an Idealized GCM

**Teaching Experience**

Graduate Writing Tutor, Penn State University Jan 2017 – present  
Teaching assistant at Penn State University  
*Astrobiology* Fall 2019  
*Geology of the National Parks* (online course) Spring 2017, Spring 2019  
*Introduction to the Earth System* Fall 2015, Fall 2018  
*Global Water Cycle* (Brown University) Spring 2015

**Conferences**

EON-ELSI Astrobiology Winter School—Earth-Life Sciences Institute, Tokyo Jan 2018  
NASA Astrobiology Summer School—NASA and Centro de Astrobiología June 2017  
AGU Fall Meeting, talks and posters 2014, 2016, 2018, 2019

**Awards and Honors**

2<sup>nd</sup> place, Pre-Comps Talks—51<sup>st</sup> Geosciences Graduate Colloquium 2018  
Krynine Scholarship 2018, 2019

**Institutional Roles**

Geosciences Dept Graduate Colloquium budget manager; co-chair 2017–2020; 2020